

Convergence of Heterogeneous Wireless Networks for 5G-and-Beyond Communications: Applications, Architecture, and Resource Management

Lead Guest Editor: Mostafa Z. Chowdhury

Guest Editors: Md Jahidur Rahman, Gabriel-Miro Muntean, Phuc V. Trinh, and Juan C. Cano





**Convergence of Heterogeneous
Wireless Networks for 5G-and-Beyond
Communications: Applications, Architecture,
and Resource Management**

Wireless Communications and Mobile Computing

**Convergence of Heterogeneous
Wireless Networks for 5G-and-Beyond
Communications: Applications, Architecture,
and Resource Management**

Lead Guest Editor: Mostafa Z. Chowdhury

Guest Editors: Md Jahidur Rahman, Gabriel-Miro Muntean,
Phuc V. Trinh, and Juan C. Cano



Copyright © 2019 Hindawi. All rights reserved.

This is a special issue published in “Wireless Communications and Mobile Computing.” All articles are open access articles distributed under the Creative Commons Attribution License, which permits unrestricted use, distribution, and reproduction in any medium, provided the original work is properly cited.

Editorial Board

- Javier Aguiar, Spain
Ghufran Ahmed, Pakistan
Wessam Ajib, Canada
Muhammad Alam, China
Eva Antonino-Daviu, Spain
Shlomi Arnon, Israel
Leyre Azpilicueta, Mexico
Paolo Barsocchi, Italy
Alessandro Bazzi, Italy
Zdenek Becvar, Czech Republic
Francesco Benedetto, Italy
Olivier Berder, France
Ana M. Bernardos, Spain
Mauro Biagi, Italy
Dario Bruneo, Italy
Jun Cai, Canada
Zhipeng Cai, USA
Claudia Campolo, Italy
Gerardo Canfora, Italy
Rolando Carrasco, UK
Vicente Casares-Giner, Spain
Luis Castedo, Spain
Ioannis Chatzigiannakis, Italy
Lin Chen, France
Yu Chen, USA
Hui Cheng, UK
Ernestina Cianca, Italy
Riccardo Colella, Italy
Mario Collotta, Italy
Massimo Condoluci, Sweden
Daniel G. Costa, Brazil
Bernard Cousin, France
Telmo Reis Cunha, Portugal
Igor Curcio, Finland
Laurie Cuthbert, Macau
Donatella Darsena, Italy
Pham Tien Dat, Japan
André de Almeida, Brazil
Antonio De Domenico, France
Antonio de la Oliva, Spain
Gianluca De Marco, Italy
Luca De Nardis, Italy
Liang Dong, USA
Mohammed El-Hajjar, UK
Oscar Esparza, Spain
Maria Fazio, Italy
Mauro Femminella, Italy
Manuel Fernandez-Veiga, Spain
Gianluigi Ferrari, Italy
Ilario Filippini, Italy
Jesus Fontecha, Spain
Luca Foschini, Italy
A. G. Fragkiadakis, Greece
Sabrina Gaito, Italy
Óscar García, Spain
Manuel García Sánchez, Spain
L. J. García Villalba, Spain
José A. García-Naya, Spain
Miguel Garcia-Pineda, Spain
A.-J. García-Sánchez, Spain
Piedad Garrido, Spain
Vincent Gauthier, France
Carlo Giannelli, Italy
Carles Gomez, Spain
Juan A. Gómez-Pulido, Spain
Ke Guan, China
Antonio Guerrieri, Italy
Daojing He, China
Paul Honeine, France
Sergio Ilarri, Spain
Antonio Jara, Switzerland
Xiaohong Jiang, Japan
Minho Jo, Republic of Korea
Shigeru Kashihara, Japan
Dimitrios Katsaros, Greece
Minseok Kim, Japan
Mario Kolberg, UK
Nikos Komninos, UK
Juan A. L. Riquelme, Spain
Pavlos I. Lazaridis, UK
Tuan Anh Le, UK
Xianfu Lei, China
Hoa Le-Minh, UK
Jaime Lloret, Spain
Miguel López-Benítez, UK
Martín López-Nores, Spain
Javier D. S. Lorente, Spain
Tony T. Luo, Singapore
Maode Ma, Singapore
Imadeldin Mahgoub, USA
Pietro Manzoni, Spain
Álvaro Marco, Spain
Gustavo Marfia, Italy
Francisco J. Martinez, Spain
Davide Mattera, Italy
Michael McGuire, Canada
Nathalie Mitton, France
Klaus Moessner, UK
Antonella Molinaro, Italy
Simone Morosi, Italy
Kumudu S. Munasinghe, Australia
Enrico Natalizio, France
Keivan Navaie, UK
Thomas Newe, Ireland
Wing Kwan Ng, Australia
Tuan M. Nguyen, Vietnam
Petros Nicopolitidis, Greece
Giovanni Pau, Italy
Rafael Pérez-Jiménez, Spain
Matteo Petracca, Italy
Nada Y. Philip, UK
Marco Picone, Italy
Daniele Pinchera, Italy
Giuseppe Piro, Italy
Vicent Pla, Spain
Javier Prieto, Spain
Rüdiger C. Pryss, Germany
Sujan Rajbhandari, UK
Rajib Rana, Australia
Luca Reggiani, Italy
Daniel G. Reina, Spain
Jose Santa, Spain
Stefano Savazzi, Italy
Hans Schotten, Germany
Patrick Seeling, USA
Muhammad Z. Shakir, UK
Mohammad Shojafar, Italy
Giovanni Stea, Italy
Enrique Stevens-Navarro, Mexico
Zhou Su, Japan
Luis Suarez, Russia
Ville Syrjäla, Finland



Hwee Pink Tan, Singapore
Pierre-Martin Tardif, Canada
Mauro Tortonesi, Italy
Federico Tramarin, Italy
Reza Monir Vaghefi, USA

Juan F. Valenzuela-Valdés, Spain
Aline C. Viana, France
Enrico M. Vitucci, Italy
Honggang Wang, USA
Jie Yang, USA

Sherali Zeadally, USA
Jie Zhang, UK
Meiling Zhu, UK

Convergence of Heterogeneous Wireless Networks for 5G-and-Beyond Communications: Applications, Architecture, and Resource Management

Mostafa Zaman Chowdhury , Md Jahidur Rahman , Gabriel-Miro Muntean , Phuc V. Trinh , and Juan Carlos Cano 

Editorial (2 pages), Article ID 2578784, Volume 2019 (2019)

Efficient Content Delivery for Mobile Communications in Converged Networks

Mahfuzur Rahman Bosunia  and Seong-Ho Jeong 

Research Article (12 pages), Article ID 3170694, Volume 2019 (2019)

Fuzzy Based Network Assignment and Link-Switching Analysis in Hybrid OCC/LiFi System

Moh. Khalid Hasan , Mostafa Zaman Chowdhury , Md. Shahjalal , and Yeong Min Jang 

Research Article (15 pages), Article ID 2870518, Volume 2018 (2019)

Exploiting Opportunistic Scheduling for Physical-Layer Security in Multitwo User NOMA Networks

Kyusung Shim  and Beongku An 

Research Article (12 pages), Article ID 2797824, Volume 2018 (2019)

An Implementation Approach and Performance Analysis of Image Sensor Based Multilateral Indoor Localization and Navigation System

Md. Shahjalal , Md. Tanvir Hossan , Moh. Khalid Hasan , Mostafa Zaman Chowdhury , Nam Tuan Le , and Yeong Min Jang 

Research Article (13 pages), Article ID 7680780, Volume 2018 (2019)

Threshold Secret Sharing Transmission against Passive Eavesdropping in MIMO Wireless Networks

Jungho Myung, Keunyoung Kim, and Taehong Kim 

Research Article (7 pages), Article ID 4143061, Volume 2018 (2019)

Network-Assisted Optimal Datalink Selection Scheme for Heterogeneous Aeronautical Network

Dongli Wang , Guoce Huang, Shufu Dong, Yequn Wang, Jian Liu, and Weiting Gao

Research Article (13 pages), Article ID 9349824, Volume 2018 (2019)

Editorial

Convergence of Heterogeneous Wireless Networks for 5G-and-Beyond Communications: Applications, Architecture, and Resource Management

Mostafa Zaman Chowdhury ^{1,2}, **Md Jahidur Rahman** ³, **Gabriel-Miro Muntean** ⁴,
Phuc V. Trinh ⁵ and **Juan Carlos Cano** ⁶

¹Kookmin University, Seoul, Republic of Korea

²Khulna University of Engineering & Technology (KUET), Khulna, Bangladesh

³Qualcomm Technologies Inc., San Diego, CA, USA

⁴Dublin City University (DCU), Dublin, Ireland

⁵National Institute of Information and Communications Technology (NICT), Tokyo, Japan

⁶Technical University of Valencia, Camí de Vera, Spain

Correspondence should be addressed to Mostafa Zaman Chowdhury; mzaman@kookmin.ac.kr

Received 25 December 2018; Accepted 25 December 2018; Published 14 January 2019

Copyright © 2019 Mostafa Zaman Chowdhury et al. This is an open access article distributed under the Creative Commons Attribution License, which permits unrestricted use, distribution, and reproduction in any medium, provided the original work is properly cited.

Evolving fifth-generation- (5G-) and-beyond communication networks are envisioned to provide services with massive connectivity, ultrahigh data-rate, ultralow latency, much improved security, very low energy consumption, and high quality of experience. 5G-and-beyond communication systems not only will be more advanced but also are expected to be more complex in comparison with legacy systems. To achieve the goals of 5G-and-beyond communication systems, convergence of the heterogeneous wireless technologies has emerged as one of the key solutions. This entails convergence of not only the radio frequency (RF) technologies, but also the optical and RF/optical wireless technologies. The optical spectrum is considered as an emerging solution for the development of future high capacity optical wireless communication (OWC) networks. It offers unique advantages, such as huge unregulated optical spectrum and inherent security. Therefore, future networks are anticipated to adopt a multitier RF/optical architecture comprising macrocells, microcells, different types of licensed small cells, optical attocells, OWC networks, and relays. The future 5G-and-beyond systems, instead of being a single wireless access network, will be a “network of networks.” The seamless integration among

heterogeneous wireless, optical and RF/optical wireless networks, demands paradigm shifts in such a way that different networks collaborate with each other so as to achieve the desired goals of the 5G-and-beyond communications. In order to attain full convergence of the heterogeneous networks, many technical issues need to be resolved.

The motivation behind this special issue has been to solicit cutting-edge research relevant to applications, architecture, and resource management of heterogeneous wireless networks for 5G-and-beyond communications. This special issue invited papers that address such issues. Following a rigorous review process (including a second review round), six outstanding papers have been finally selected for inclusion in the special issue. The accepted papers cover a wide range of research subjects in the broader area of convergence of heterogeneous wireless networks to meet the demand of 5G-and-beyond communications systems.

The paper “*Network-Assisted Optimal Datalink Selection Scheme for Heterogeneous Aeronautical Network*” by D. Wang et al. focuses on datalink selection mechanism in heterogeneous aeronautical network. The authors proposed a priority distinction selection algorithm by constructing

multiuser multiobjective optimization problem to maximize the number of users accessing their optimal datalinks and minimize the modification of the users' access requests.

The paper by J. Myung et al. entitled "*Threshold Secret Sharing Transmission against Passive Eavesdropping in MIMO Wireless Networks*" proposes a threshold secret sharing scheme for secure communications in multiple input and multiple output wireless networks. In their novel scheme, the base station divides the secret data into a number of parts using a polynomial-based approach and transmits the divided data to the legitimate user by beamforming with multiple spatial dimensions.

The paper "*An Implementation Approach and Performance Analysis of Image Sensor Based Multilateral Indoor Localization and Navigation System*" by M. Shahjalal et al. investigates the implementation issues for indoor mobile robot localization and navigation systems. The authors proposed an indoor navigation and positioning combined algorithm and further evaluate its performance for the feasibility of real-implementation. They developed an Android application to support data acquisition from multiple simultaneous transmitter links.

The paper by K. Shim et al. entitled "*Exploiting Opportunistic Scheduling for Physical-Layer Security in Multitwo User NOMA Networks*" addresses the opportunistic scheduling in multitwo user nonorthogonal multiple access (NOMA) systems consisting of one base station, multiple near users, multiple far users, and one eavesdropper. The authors introduced a user selection scheme, called best-secure-near-user best-secure-far-user scheme to improve the secrecy performance. Additionally, the authors proposed a descent-based search method to find the optimal values of the power allocation coefficients that can minimize the total secrecy outage probability.

The paper "*Fuzzy Based Network Assignment and Link-Switching Analysis in Hybrid OCC/LiFi System*" by M. Khalid et al. proposes a hybrid optical camera communications and light fidelity architecture to improve the quality-of-service (QoS) of users. The authors present a network assignment mechanism for such hybrid systems. A dynamic link-switching technique is proposed which includes switching provisioning based on user mobility and detailed network switching flow analysis. Fuzzy logic is used to develop their proposed mechanism. A time-division multiple access is also adopted to ensure fairness in time resource allocation while serving multiple users using the same light-emitting diode in the hybrid system.

The paper by M. R. Bosunia and S.-Ho Jeong entitled "*Efficient Content Delivery for Mobile Communications in Converged Networks*" proposes a content-centric networking based content delivery mechanism for 4G and 5G heterogeneous converge networks. The authors described a mobility management scheme to support the content diversity and network diversity by leveraging the abundant computation resources in the mobile network. In addition, this paper analyzes the existing approaches with respect to mobility and evaluates the performance of their seamless content delivery mechanisms in terms of content transfer time, throughput, and data transmission success ratio.

Conflicts of Interest

The authors declare that they have no conflicts of interest.

Acknowledgments

The editors would like to thank all the authors who submitted their excellent research articles to this special issue. Also, we would like to express our deepest gratitude to all the reviewers for providing their valuable and timely feedback during the review process, which helped to improve the quality of this special issue. The work of Mostafa Zaman Chowdhury was supported by the Korea Research Fellowship Program through the National Research Foundation of Korea (NRF) funded by the Ministry of Science and ICT (2016H1D3A1938180).

Mostafa Zaman Chowdhury
Md Jahidur Rahman
Gabriel-Miro Muntean
Phuc V. Trinh
Juan Carlos Cano

Research Article

Efficient Content Delivery for Mobile Communications in Converged Networks

Mahfuzur Rahman Bosunia ¹ and Seong-Ho Jeong ²

¹Bangladesh Bank, Dhaka, Bangladesh

²Dept. of Information and Communications Engineering, Hankuk University of Foreign Studies, Seoul, Republic of Korea

Correspondence should be addressed to Seong-Ho Jeong; shjeong@hufs.ac.kr

Received 3 August 2018; Accepted 4 November 2018; Published 14 January 2019

Guest Editor: Mostafa Zaman Chowdhury

Copyright © 2019 Mahfuzur Rahman Bosunia and Seong-Ho Jeong. This is an open access article distributed under the Creative Commons Attribution License, which permits unrestricted use, distribution, and reproduction in any medium, provided the original work is properly cited.

The mobile Internet is already playing a key role in people's daily lives worldwide, resulting in the dramatic growth in the number of mobile devices. The size of the Internet and the amount of the traffic are being expanded rapidly, which poses various challenges. In particular, the Internet and mobile communications are entering a new era that demands faster communication services and uninterrupted content delivery. A new paradigm called content-centric networking (CCN) is considered as an appropriate way for efficient content delivery. In this paper, we propose a CCN-based efficient content delivery mechanism in the 4G network and also in the upcoming 5G network where various heterogeneous networks are converged. We also propose a novel mobility management scheme to support the content diversity and network diversity by leveraging the abundant computational resources in the mobile network. In addition, we analyze the existing approaches with respect to mobility and evaluate the performance of our seamless content delivery mechanism in terms of content transfer time, throughput, and data transmission success ratio. Simulation results are also presented to show that the content-centric wireless network with our mobility management scheme can improve the data delivery services significantly compared to the existing schemes.

1. Introduction

Recently, as the use of mobile devices such as smart phones and tablets has increased exponentially, the number of services that connect mobile devices to the Internet has also increased. Accordingly, the volume of the mobile content has increased enormously, and it is a big challenge to support fast content delivery as well as seamless mobility in the wireless network. The content-centric networking (CCN) [1, 2] architecture can be useful to resolve this issue.

The current Internet is configured for host-to-host communication, and therefore it is not suitable for the future Internet which will deal with various contents and provide seamless mobility for moving users. The main focus of CCN is to provide more efficient, faster, and secured delivery of a content rather than to establish the communication path to the content source. CCN provides name-based routing without exploiting the content/device address. CCN operates using two simple messages for content transmission: first one

is the Interest packet and the other is the Data packet. The Interest packet contains the request for a desired content, and the request consists of different attributes such as content name, content type, and content version. The Data packet contains the original data with the content name, security related information, and several other attributes, e.g., hop distance and content source description.

Figure 1 shows the CCN forwarding module which is equipped with three functional and operative elements for content-based routing: Content Store (CS), Forwarding Information Base (FIB), and Pending Interest Table (PIT). The CS is the physical storage of the content and stores the identical name of the published content. The FIB preserves the content routing information for mapping between the content name and the next hop towards the content source. The PIT keeps track of and records the status of all received Interest packets in order to satisfy later when the content is on hand. Any node that wants to publish a content spreads the content name to the nearby nodes to make it available

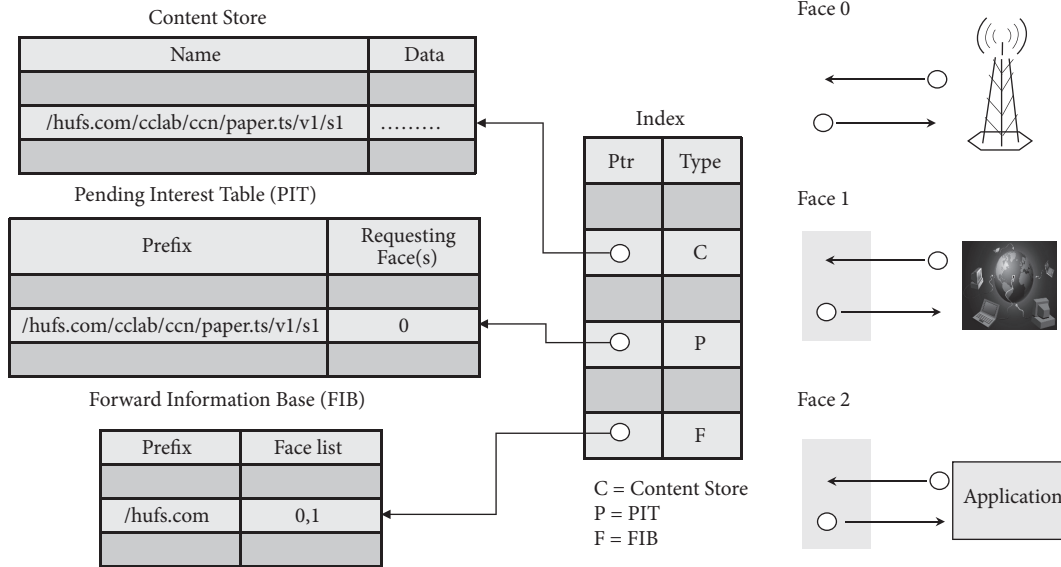


FIGURE 1: A forwarding module for CCN.

and accessible to the content consumers. A node sends an Interest packet to retrieve a content based on the routing information available in the FIB. When a node receives the Interest packet, it enforces a lookup inside the CS to check the content availability. If the requested content is available then the content is delivered back to the content requester. If the content is not available inside the CS, a pending Interest is recorded in the PIT and the Interest packet is forwarded via the face guided by the FIB.

The LTE-based 4G mobile network establishes a network architecture to provide faster data retrieval and seamless mobility management. Even though LTE promises to be a faster and more efficient data delivery network, its communication architecture is still centralized and host oriented; thus various performance degradation issues, e.g., high bandwidth consumption, cross domain traffic, high delay for the long communication path, and waste of network resources, may need to be resolved. A new paradigm called CCN is considered as an appropriate way of efficient content delivery as mentioned above. The integration of CCN and LTE can be used to resolve the issues by providing timely and fast delivery of the data with efficient resource utilization.

In this paper, we propose a CCN-based efficient content delivery mechanism in the 4G network and also in the upcoming 5G network where various heterogeneous networks are converged. We also propose an efficient mobility management mechanism to address the content diversity and network diversity by leveraging the abundant computational resources in the LTE-based 4G network. Our proposed mobility management scheme introduces a context-aware handover prediction mechanism to deal with the heterogeneity of wireless content providers and consumers. Context awareness provides a significant effect to guarantee data continuity in the mobile environment. We also introduce a content similarity matching mechanism to provide the data continuity when mobility increases the chance of data

unavailability. The rest of the paper is organized as follows. Section 2 describes the recent work related to content delivery in CCN. Section 3 presents a novel approach to integrate CCN with LTE and some mechanisms for efficient and seamless content delivery in the LTE network in detail. Section 4 describes implementation details and performance issues, and finally, Section 5 concludes the paper.

2. Related Work

Seamless content delivery and mobility management in wireless networks are important research issues which have been focused a lot under various scenarios. A lot of works have been proposed so far in this area. The LTE network is limited to the measured value of the received signal strength which is a factor that triggers handover in the wireless network. In reality, handover involves content delivery rate requirements for a particular application, packet loss, end-device demand for high/low data rate, and many more.

There are various mobility-related mechanisms and protocols across all the layers in the TCP/IP protocol stack for providing seamless content transmission. For example, Mobile IP [3] provides mobility support at the Network layer; the Stream Control Transmission Protocol (SCTP) [3] and the Datagram Congestion Control Protocol (DCCP) [3] provide seamless mobility support at the transport layer. Dynamic DNS (DDNS) [3] and Session Initiation Protocol (SIP) [3] are examples to provide mobility management at the application layer. The efficiency of these mechanisms is limited due to the acting of IP address as a locator as well as an identifier and also due to the cross layer communication between different layers. The separation of the locator from its identifier is proposed in Host Identity Protocol (HIP) [3] and Locator Identifier Separation Protocol (LISP) [4], but they cannot come out from the host-to-host communication scenario.

The future Internet architecture based on Information-Centric Networking (ICN) such as CCN, Name Data Networking (NDN), Data-Oriented Network Architecture (DONA), and Network of Information (NetInf) uses in-network content caching to improve the efficiency of content transmission, reduce the network traffic and content access latencies, alleviate the present communication bottlenecks, and support ubiquitous access and efficient mobility management. DONA [5] introduces integrated name resolution and content-based routing schemes by replacing the concept of DNS in the traditional TCP/IP based Internet architecture. DONA uses a flat, self-certifying name of a content and registers the content name and the location in a domain server called Resolution Handlers (RHs). RHs are structured into a BGP topology of the network and content lookups are performed by querying a consumer to its local RH. If no reference of the requested content is found, the query is forwarded up the tree until a content source is found; an out-of-band delivery path is then established by the source (over IP). DONA reduces the applicability due to the dependency on RHs like DNS and location-based communication. The amount of delay and overhead may also be a big concern for DONA.

Network of Information (NetInf) [6] follows the similar mechanisms as DONA and also provides content delivery using a name resolution (NR) service. To handle content and device mobility issues and provide content-based routing, NetInf uses Multiple Distributed Hash Table (MDHT) [7] and Late Locator Construction (LLC) [8] schemes. MDHT and LLC try to make the content management and name resolution simple and provide in-network content caching. PERSUIT [9] uses three key components, Rendezvous, Topology, and Routing, to provide seamless content delivery and mobility management in a publish/subscribe architecture. Bloom filter based source routing is used to transfer content through the network [10]. However, NetInf reduces its efficiency due to the dependency on the NR which is responsible for content registration, content updates, and content-based route establishment. It requires a re-binding similar to DONA. The mechanism for handling mobility in NetInf may vary according to the chosen content locator; thus the implementation can be complex. The cost of updating the routing information for PERSUIT is very high. The packet loss may be significant in the case of high mobility.

The CCN architecture [11, 12] decouples the content from the location and device and distributes the content using content name-based routing. In CCN, consumer mobility is managed inherently by its receiver driven nature. There is no need to update the routing information due to mobility from a consumer's perspective; the consumer just retransmits Interest packets if the content is not available yet. Even though CCN supports consumer mobility inherently, it faces long delays to re-issue the Interest after re-binding to a new network and cannot provide seamless content transmission. Content provider mobility is still an open issue in CCN; there are several issues to be resolved such as update of routing and location information, repeated transmission of Interest/Data packets, and undesirable content delivery delays due to mobility.

A proxy-based approach [13] proposes a publisher mobility support protocol in CCN and a fast FIB update mechanism. It introduces the mobility entry in FIB for mobile and temporal destination and also defines the Home Router (HR) or proxy to announce the original entry of the publisher to the network and establish a tunnel between the previous point of attachment and a new point of attachment to reduce the packets loss due to mobility. Clustered CCN [14] introduces the cluster concept to support mobility which can be viewed as a hierarchical mobility management scheme to support the extensive mobile domain. It forms a cluster with a cluster head that manages all the responsibilities of its members like Interest processing and mobility tracking. With the assistance of the cluster or proxy, it can reduce the Interest dissemination and content distribution, but the overhead and complexity of this approach are high due to its centralized and hierarchical nature.

A converged network is useful to exploit content diversity and device heterogeneity by disseminating contents through several networks, e.g., Wi-Fi, broadcast networks or cellular networks [15, 16]. Despite a large variability of content requests to several routes and several content sources for efficient transmission of user requests and content storing, content requests are typically satisfied by the nearby devices or networks [17–19]. The separation among content delivery, content storage, and content and device mobility operations may reduce the performance efficiency of the network and increases the operational complexity of the network.

Fetching the content before handover was proposed in [20] to support producer mobility in name-based routing. Software defined controller for CCN [21] proposed a mobility management mechanism for allowing packet forwarding and intermediate routing on the device mobility. Software Defined Mobile Network [22] was proposed to improve the content delivery efficiency by optimizing caching in the LTE network in which Software Defined Networking (SDN) mechanisms were integrated with the Mobility Management Entity (MME). It allows dynamic relocation of contents in any intermediate node. This mechanism was compared and evaluated in [23] by using simulation. The simulation results showed that the in-node content caching reduced traffic load and improved content delivery efficiency. Even though intermediate content storing ensures faster content access, the virtual tunnel-based content redirection in the LTE network increases the overhead and reduces the transmission efficiency.

A mobility direction prediction mechanism was proposed in [24] for reducing the number of handovers and data losses in the LTE network. However the scope of this work is very limited due to the TCP/IP-based communication nature. The future mobile networks demand the mobility and portability of devices and data or contents in an autonomous and adaptive way to provide seamless content delivery, to be connected to several access networks simultaneously, and maintain the high quality of content transmission without any interruption even in the highly mobile environment. The proposed mechanism is an enhancement to our previous work [25], which makes it possible to directly fetch and store contents in any appropriate node before handover to enable

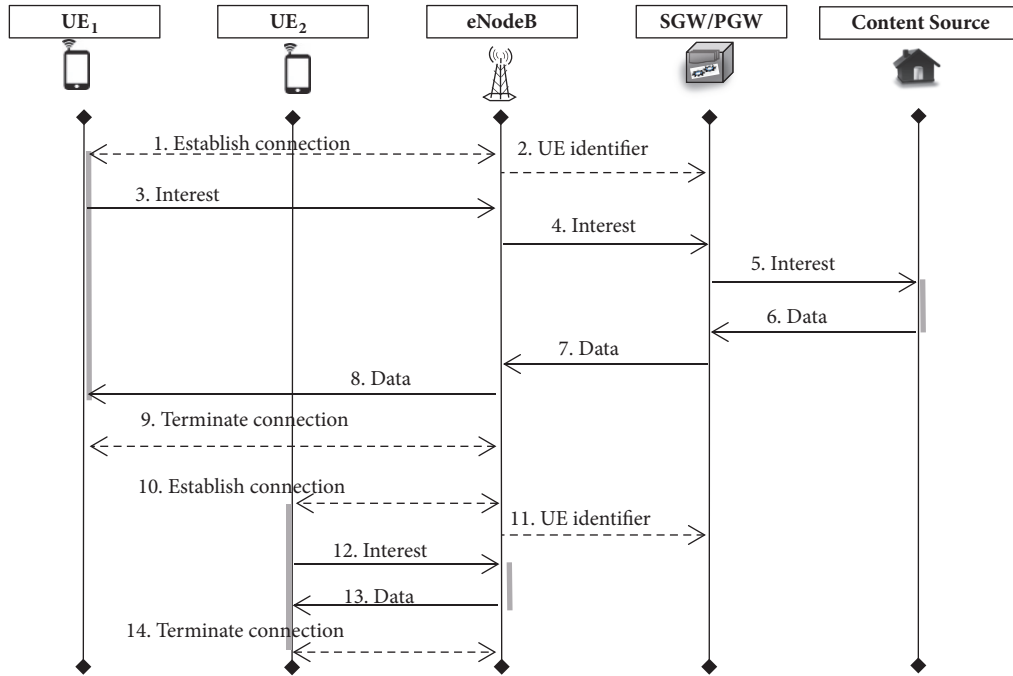


FIGURE 2: Content delivery procedure in the content-centric mobile network (e.g., LTE network).

faster content retrieval for reducing content transmission delays and preventing the repeated transmission of Interest/Data packets to avoid the network congestion.

3. A CCN-based Mechanism for Seamless and Efficient Content Delivery in the Mobile Network

Mobility in the Internet means that either the consumer or the provider is moving away from its point of attachment to another or both of them are moving away together. Mobility support is a service such that the mobility of the node should not result in any loss of data or extended periods of disconnection. It is still an issue how CCN will be integrated with the LTE network. We simplify here a seamless data delivery procedure in the content-centric LTE network. The eNodeB, SGW/PGW, and MME can support the CCN function and protocols. The detailed content delivery procedure in the content-centric LTE network is described below and also shown in Figure 2.

- (i) Step 1: UE₁ establishes a connection to an eNodeB.
- (ii) Step 2: the eNodeB sends the UE₁ information containing the node identifier and the interface identifier to the SGW/PGW.
- (iii) Step 3: UE₁ sends the Interest packet via the eNodeB. When the eNodeB receives the Interest packet, it performs according to the basic operation of the CCN node.
- (iv) Step 4: the SGW/PGW receives the Interest packet from the eNodeB. After searching its CS and PIT, if no matched content is found, it checks its FIB.

- (v) Step 5: the SGW/PGW's FIB sends the Interest packet via the face of the content provider.
- (vi) Step 6: when a content provider receives the Interest packet, it searches its CS. When the matched content is found, it sends the Data packet of the content out via the incoming face.
- (vii) Steps 7, 8: when the SGW/PGW receives the Data packet, it forwards it to the eNodeB and UE₁ based on their PIT.
- (viii) Step 9: UE₁ terminates the connection.
- (ix) Step 10: UE₂ establishes a connection to the eNodeB.
- (x) Step 11: the eNodeB sends the UE₂ information containing the node identifier and the interface identifier to the SGW/PGW.
- (xi) Step 12: UE₂ sends the Interest packet to the eNodeB.
- (xii) Step 13: when the eNodeB receives the Interest packet, it performs according to the basic operation of the CCN node. Since it is cached in the previous eNodeB, it sends the Data packet to UE₂.
- (xiii) Step 14: UE₂ terminates the existing connection.

3.1. Device Mobility Prediction. Device mobility or consumer mobility allows consumers to change their point of attachment without disrupting the connectivity. We have defined a mathematical model which takes into account the preference of end devices, e.g., UEs, when selecting a base station for seamless and fast content retrieval and content delivery services. Let x be a value for a single criterion and α be the steepness. $x_{min} \leq x_m \leq x_{max}$ where x_m is the midpoint of the

variation range. These variations can be defined as [26] using the single criteria utility function as shown in

$$u(x) = \begin{cases} 0 & \text{if } x \leq x_{min} \\ \frac{1}{1 + e^{\alpha(x_m - x)/(x - x_{min})}} & \text{if } x_{min} < x \leq x_m \\ 1 - \frac{1}{1 + e^{\beta(x - x_m)/(x_{max} - x)}} & \text{if } x_m < x \leq x_{max} \\ 1 & \text{if } x \geq x_{max} \end{cases} \quad (1)$$

where

$$\beta = \frac{\alpha(x_{max} - x_m)}{x_m - x_{min}} \quad (2)$$

and $\alpha > 0$ is the tuned steepness parameter. The proposed utility function satisfies the following properties: $u(x) = 0 \forall x \leq x_{min}$, $u(x) = 1 \forall x \geq x_{max}$, and $u(x_m) = 0.5$. The point of attachment selection in the wireless networking environment is based on the aggregation of different utility functions for decision processes. Hence, we define here a multicriteria utility function that is able to integrate the end devices' different choice metrics to select a best point of attachment. Let $R = R_1 \dots R_n$ be a set of potential alternatives (e.g., possible different eNodeBs) and each alternative can be described as a different descriptor or attributes (e.g., received signal strength, mobility direction, and load in terms of data transfer rate) $x = x_1 * \dots * x_n$, and each alternative attribute being described as a utility function $u(x_n)$, the simple weighted average of different alternatives $A(R_1 \dots R_n)$ is used to maximize the selection probability of the best eNodeB as follows:

$$A_R = \sum_{i=1}^l w_i u(x_i) \quad (3)$$

where w_i is a weight that reflects the content receiver's preference. Weights are assigned according to the UE's expected criteria.

(i) *Received Signal Strength.* Received signal strength (RSS) is one of the most popular parameters to take a handover decision. By monitoring the RSS, it is easily determined whether the UE should connect to a new eNodeB or not. The UE reports the received RSS value for all the neighbor eNodeBs to the serving eNodeB. The eNodeB that takes a handover decision uses the RSS values of each eNodeB in a single criteria utility function as shown in (1).

(ii) *Mobility Direction.* The proposed mechanism also uses the moving direction prediction of each UE to make the decision of the movement towards an eNodeB. We assume that each eNodeB is aware of the position of the 2-hop neighbor eNodeBs and each UE is aware of its own position. Assuming the serving eNodeB position is (X_e, Y_e) , the position of the UE is (X_u, Y_u) , and the candidate eNodeB position is (X_n, Y_n) , using the Pythagorean Theorem, it is possible to estimate distance between a UE and a candidate eNodeB as shown in

$$d = \sqrt{(X_n - X_u)^2 + (Y_n - Y_u)^2} = \sqrt{(\Delta X)^2 + (\Delta Y)^2} \quad (4)$$

Therefore, the probability of a UE being in a coverage area of an eNodeB is

$$P_r \{d \leq R_r\} = P_r \left\{ \sqrt{(\Delta X)^2 + (\Delta Y)^2} \leq R_r \right\} \quad (5)$$

So d is normalized using the coverage R_r as follows:

$$d_R = \frac{R_r - d}{R_r} \quad (6)$$

Since the velocity is a vector and a UE moves to different direction, it is reasonable to predict the direction or angle of the UE towards a candidate SBS using the vector formula. The moving angle of the UE from the associated eNodeB to a new candidate eNodeB can be estimated as shown in

$$\theta = \cos^{-1} \frac{X_u X_n + Y_u Y_n}{\sqrt{X_u^2 + Y_u^2} * \sqrt{X_n^2 + Y_n^2}} \quad (7)$$

It is considered that the 120° angle is the acceptable angle towards a eNodeB as in [24]. So it is considered as an offset of $\mu = \pm 60^\circ$ to normalize the θ value as shown in the following formula

$$\theta_R = \frac{\mu - \theta}{\mu} \quad (8)$$

Then θ and d are used to estimate the movement prediction P_m as shown in the following formula

$$P_m = (1 - \alpha) * d_R + \alpha * \theta_R \quad (9)$$

The eNodeB that takes a handover decision uses the movement prediction values of (9) of each eNodeB in a single criteria utility function as shown in (1).

(iii) *Load.* In order to take the accurate context based decision for handover, the load of a candidate eNodeB was additionally considered. In some cases, the UE can attach to an eNodeB which has a greater RSS value but might be overloaded in terms of connected UEs. In other words, based only the RSS and the number of associated UEs that are currently associated with an eNodeB, the handover decision may experience the degradation of a performance. Each eNodeB transmits its current work load to its two hop neighbor eNodeBs. The eNodeB that takes a handover decision uses the work load value of each eNodeB in a single criteria utility function as shown in (1).

3.2. *Candidate eNodeB Selection.* The handover decision is made in the serving eNodeB. The UE reports the measurement of RSS values of all the candidate eNodeBs and its own position information to the associated eNodeB. Each eNodeB sends its load estimation to 2-hop neighbor eNodeBs. Then the associated eNodeB uses (1) to make the utility estimation of each alternative of the eNodeB. For each candidate eNodeB, three different utility values are estimated and combined in the aggregated metric function as shown in (3). The serving eNodeB selects the eNodeB which has the highest aggregated metric value.

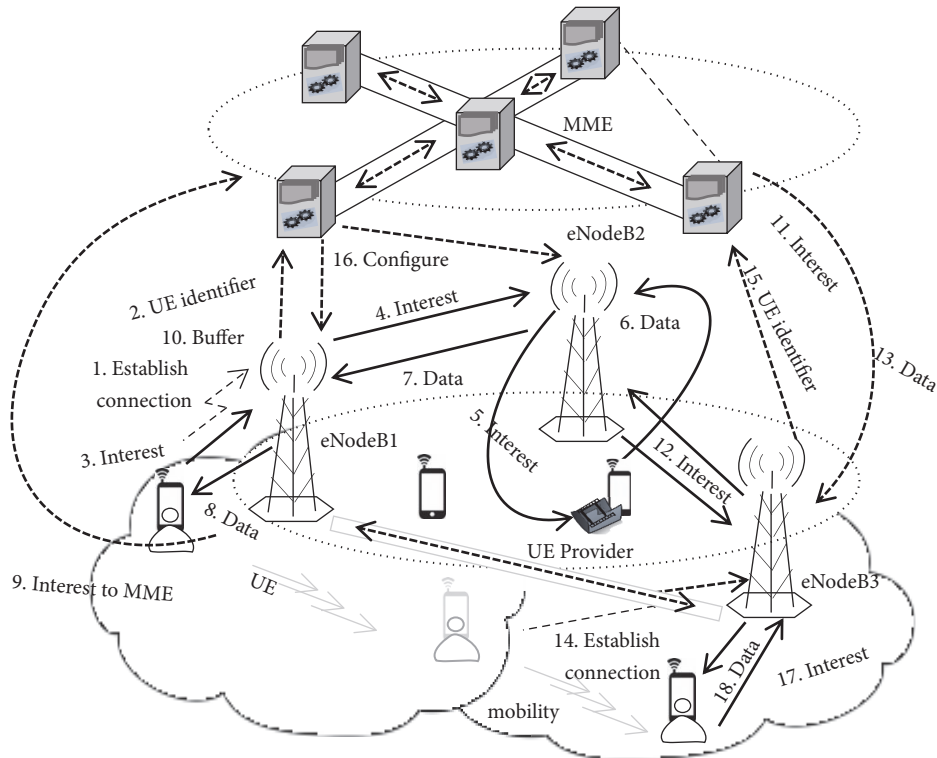


FIGURE 3: Seamless content retrieval in the highly mobile environment.

3.3. Seamless Content Retrieval Using MME. Consumer mobility allows consumers to change their point of attachment without disrupting connectivity. The point of attachment selection in the wireless networking environment is based on an aggregation of different utility functions for decision processes. Hence, we define here multicriteria that are able to integrate the end devices' different choice metrics to select the best point of attachment. This paper proposes a soft-handover approach where a new connection is established with the new eNodeB before breaking the current connection. This is almost similar to the follow-me service that is the modern trend of mobile communications. In the proposed approach, UEs send the measurement reports to the serving eNodeB. Then the eNodeB follows the procedure mentioned in Section 3.1 to decide whether the UE will move to a new eNodeB or not. If the serving eNodeB decides the necessity for a new eNodeB to continue the seamless content retrieval of the UE, it forwards the Interest and related information to the new eNodeB; then the new eNodeB forwards the Interest to the most appropriate content provider to retrieve the content. If the content retrieval is successful, the UE releases the connection with the old eNodeB and continues the content transfer using the new eNodeB. The message flow for seamless content retrieval of the UE is shown in Figure 3.

The detailed operational procedure for seamless content retrieval of the UE in the content-centric LTE network is described below.

(i) Step 1: an UE establishes a new connection to eNodeB1.

- (ii) Step 2: eNodeB1 sends details about the UE, e.g., UE identifier, interface identifier to MME.
- (iii) Step 3: the UE sends an Interest message via eNodeB1. When eNodeB1 receives the Interest, it follows the same procedure performed by a CCN node.
- (iv) Step 4: eNodeB2 receives the Interest message from eNodeB1 and follows the same procedure performed by a CCN node. After doing look-up on its CS and PIT, it forwards the Interest to the mobile content source (UE Provider).
- (v) Step 5: after forwarding the Interest message to the content source, it adds PIT entry to forward content in future.
- (vi) Step 6: when the content source receives the Interest message, it looks up its CS. When the matching content is found, it replies back with the Data message as a response through the arrival interface of the Interest message.
- (vii) Step 7, 8: eNodeB2 and eNodeB1 forward Data packets to the UE.
- (viii) Step 9: during the ongoing content transfer, the eNodeB1 estimates the mobility prediction and decides whether it will move from eNodeB1 or not using (3), as in Section 3.1. If the serving eNodeB1 finds the best candidate for content transmission, the eNodeB1 sends the chunk Interest to the MME

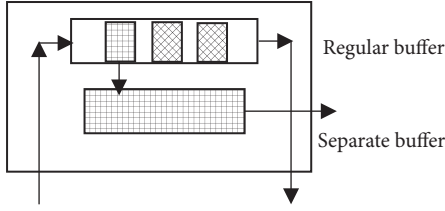


FIGURE 4: Separate buffer to store and forward data.

with preceding the Interest with the best candidate eNodeB.

- (ix) Step 10: eNodeB1 receives the Data packet but cannot transmit it to the UE efficiently. In our proposed mechanism, we maintain a separate buffer as shown in Figure 4 to store and forward the Data packets for later transmission. If an eNodeB tries to buffer the packets in the main queue, buffer overflow may hamper the normal operation of the eNodeB. To solve the problem, we maintain an extra buffer so that all the Data packets for upcoming handover can be stored separately by stamping as buffered packets. To avoid buffer overflow it checks the current queue status using the Exponentially Weighted Moving Average (EWMA) formula as shown in the following formula

$$Q_{avg} = (1 - \alpha) * Q_{avg} + Q_{curr} * \alpha \quad (10)$$

where α is a weight factor and Q_{curr} is the current queue size. eNodeB1 can buffer packets if the current status falls below or is equal to a minimum threshold called Q_{Th} calculated as shown in the following formula

$$Q_{Th} = w * Q_{size} \quad (11)$$

where w is a weight factor. Based on the extra buffer occupancy, if the value of Q_{avg} is $\leq Q_{Th}$, eNodeB1 discards the Data packet. MME sends the Interest message to eNodeB1 to transfer the buffered Data message to the desired eNodeB where the UE wants to move, e.g., eNodeB3.

- (x) Step 11: MME forwards the received Interest message to the desired eNodeB where the UE wants to move, e.g., eNodeB3.
- (xi) Step 12: eNodeB3 receives the Interest message and forwards the Interest message to the eNodeB2. It also receives the buffered Data messages sent by eNodeB1.
- (xii) Step 13: after receiving the Interest message from eNodeB3, eNodeB2 sends the Data message as a response to the Interest message.
- (xiii) Step 14: The UE terminates the connection to the eNodeB1 and uses the same physical handover operation like LTE and makes a connection to eNodeB3. It is a UE initiated handover, and the UE establishes a new connection to eNodeB3.

- (xiv) Step 15: eNodeB3 sends the UE details, e.g., UE identifier, interface identifier to MME.

- (xv) Step 16: since the UE's identifier is already registered in the MME, MME identifies that the UE is moved from eNodeB1 to eNodeB3. MME sends the Interest message to eNodeB1 and eNodeB2 to reconfigure the previous path.

- (xvi) Steps 17, 18: the UE sends the Interest to the new eNodeB, e.g., eNodeB3, and continues to receive the content seamlessly using the new eNodeB.

3.4. Seamless Content Delivery Using MME. Provider mobility allows sources to relocate without disrupting content availability. In order to reduce handover latency and the cost of the provider mobility in CCN, we propose a new mechanism that can allow soft-handover approach where a new connection is established to a new eNodeB before breaking the old connection. Once a handover occurs, the producer will update its prefix to match the new location (e.g., when a producer named /prefix moves from eNodeB1 to eNodeB2, the producer's name will change from /eNodeB1/prefix to /eNodeB2/prefix).

If the producer changes its attachment point, i.e., eNodeB, its location name becomes invalid and Interests from the UE and eNodeB will no longer reach the content source. As soon as it is assigned a new location name at the new eNodeB, the eNodeB and MME update the binding information. Consumers exploit CCN's multipath forwarding to handle handovers. Due to mobility, if the content name is changed and the producer receives the old named Interest message, then it can use similarity matching mechanism to satisfy the Interest. Let a content be denoted by d which consists of naming components or attributes, e.g., location and type denoted by v_d . Thus the content name is represented by $d = (v_1^d, v_2^d, \dots, v_m^d)$. Then for similarity matching, the following formula shown in (12) is used to calculate the similarity, $S_{1,2}$, between the content item d_1 and the content item d_2 .

$$S_{1,2} = \frac{\sum_{i=1}^m w_i * B(v_i^{d_1}, v_i^{d_2})}{\sum_{i=1}^m w_i} \quad (12)$$

where m is the number of qualitative attributes that present the content, e.g., movie, video, size, and length, w_i is the weight for each attribute based on its significance, and $B(i, m)$ is a similarity function returning 1 if $v_i^{d_1} = v_i^{d_2}$ and 0 otherwise. Using the similarity value obtained from (9) based on the requested content and available content and also based on the significance of the data, the producer can determine whether the Interest was satisfied or not. The detailed operational procedure for seamless data delivery of a provider UE in the content-centric LTE network is described below. The message flow regarding seamless data delivery of the provider UE is shown in Figure 5.

- (i) Step 1: UE (provider) establishes a connection to eNodeB1 and registers its content name to eNodeB1.

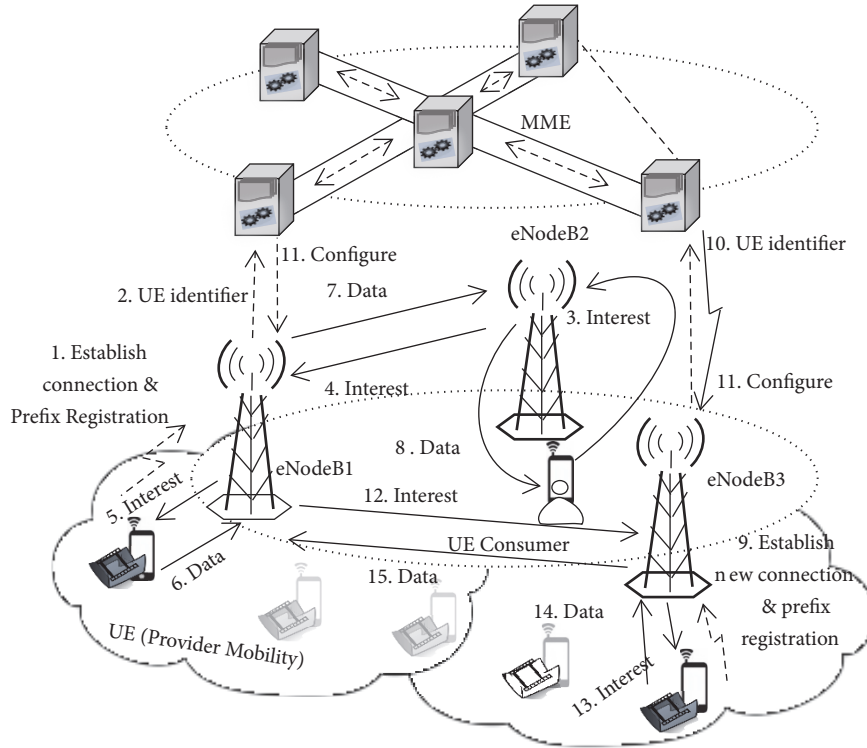


FIGURE 5: Seamless content delivery with content provider mobility.

- (ii) Step 2: eNodeB1 sends the UE the details, e.g., UE identifier, interface identifier to MME.
- (iii) Step 3: UE (consumer) sends Interest message via eNodeB2. When eNodeB2 receives the Interest, it follows the same procedure performed by a CCN node.
- (iv) Step 4: eNodeB1 receives the Interest packet from eNodeB2 and follows the same procedure performed by a CCN node. After doing look-up on its CS and PIT, it forwards the Interest to the mobile content source.
- (v) Step 5: after forwarding the Interest packet to the content source, it adds PIT entry to forward data in the future.
- (vi) Step 6: when the content source receives the Interest packet, it looks up its CS. When the matching content is found, UE replies back with the Data packet as a response through the arrival interface of the Interest packet.
- (vii) Step 7, 8: eNodeB1 and eNodeB2 forward the Data packet to the UE.
- (viii) Step 9: during the ongoing content transfer, the eNodeB1 estimates the mobility prediction using (3) and decides whether UE will move from eNodeB1 or not. If the serving eNodeB1 finds any best candidate for content transmission, it uses the same physical handover operation like LTE and triggers a connection to eNodeB3. UE establishes connection to eNodeB3.
- (ix) Step 10: eNodeB3 sends the UE details, e.g., UE identifier, interface identifier to MME.
- (x) Step 11: Since the UE's identifier is already registered in the MME, MME identifies that the UE is moved from eNodeB1 to eNodeB3. MME sends the Interest packet to eNodeB1 and eNodeB2 to reconfigure their path.
- (xi) Steps 12, 13: eNodeB1 forwards the Interest packet to eNodeB3. When eNodeB3 receives the Interest, it follows the same procedure performed by a CCN node. For content matching, it can use the similarity matching equation (9). After doing look-up on its CS and PIT, it forwards the Interest to the mobile content source.
- (xii) Step 13: UE (Content Producer) receives the old named Interest packet; it uses the similarity matching equation (9) to satisfy the Interest that is matched with any appropriate content.
- (xiii) Steps 14, 15: after receiving the Interest from eNodeB3, eNodeB2 sends the Data packet as a response to the Interest packet to eNodeB1.

4. Performance Evaluation

This section presents simulation results in order to demonstrate that the content-centric LTE network is well suited to

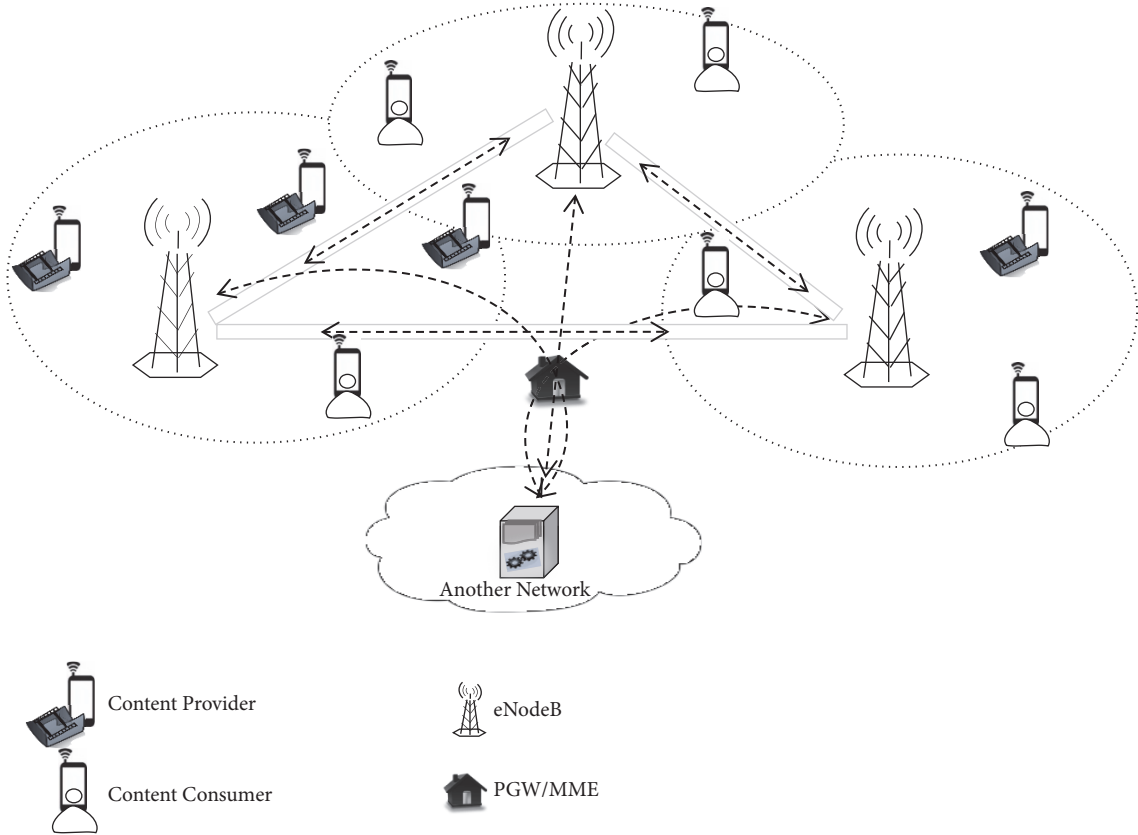


FIGURE 6: A CCN-based mobile network topology for simulation.

today's communication trend. This section also analyzes the performance of the content-centric LTE network with our proposed mobility management scheme and compares it with the prediction-based LTE [24] and mobility management for CCN [21].

The simulations were performed using CCNx, LENA/NS-3, Direct Code Execution (DCE) on VMware, and Ubuntu 12.04 environment. We used a simulation topology as shown in Figure 6. The size of the content which is transferred between the mobile producer and mobile consumer is 1.1 Mbytes. The number of eNodeBs was considered to be three to show the mobility scenario of the UEs. The number of UEs covered by each eNodeB varies from 1 to 10 to show the effectiveness of our proposed mechanisms and also to show the content delivery efficiency in the low load and high load environment. The UEs may work as a content provider or a content consumer.

We showed the performance for different number of content providers who publish the video files and different number of consumers. Each content provider publishes different content files after 1-minute interval in the whole simulation time, and contents are requested randomly from the different consumers. We selected a half of all UEs to work as consumers and the other half as producers at each eNodeB. To show the efficiency of the proposed mobility management mechanism, we varied the mobility speed of the UE. The UE was placed in the boundary of its serving eNodeB to create the handover scenario. The UEs and eNodeBs were distributed

uniformly using the grid position allocator. The simulation used a random walk mobility model, and the moving speed of UEs varied in the range from 0 km/h (stationary) to 60 km/h. When the number of the UEs and the number of the eNodeBs increase, the number of content providers and the number of generated contents also increase and the network becomes heavily loaded. For the simulation simplicity and reducing the processing complexity, we assigned each weight of (3) with the equal value of 1/3. We ran the simulation 10 times for each simulation configuration and took the average value of the results.

We evaluated the efficiency of the proposed approach and applicability by showing the average content transfer time, the average throughput observed by each consumer over time, and the average content delivery success ratio as performance parameters. We measured the average content transfer time T using the following formula:

$$T = \frac{\sum_{i=1}^n T_{i,f} - T_{i,s}}{n} \quad (13)$$

where n is the total number of UEs which are involved in receiving the content, $T_{i,s}$ is the time at which the UE i makes a requests to retrieve the content, and $T_{i,f}$ is the time at which the UE receives the requested content. Average throughput is measured as the average number of data bytes received by all the consumer UEs per second. Data transmission success ratio is the ratio of the total number of data packets received

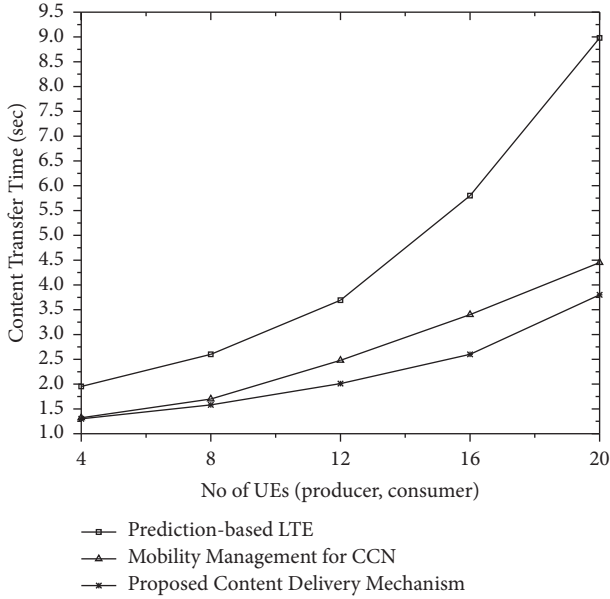


FIGURE 7: Average content transfer time.

by the all consumer UEs to the total number of Data packets sent by all the producer UEs.

4.1. Content Transfer Time. Figure 7 shows the average content transfer time observed by UEs. The average content transfer time of our proposed CCN-based mobility management mechanism has been evaluated and compared with the prediction-based LTE and CCN-based mobility management mechanism in the LTE network.

The content transfer time of our proposed approach is shorter than the content transfer time of others because of its efficient soft handover based mobility management mechanism for both consumers and producers. The introduction of the extra buffer reduces the chance of long transmission delay, queuing delay, propagation delay, and processing delay at intermediate nodes in case of high mobility scenarios. In case of high mobility cases, our proposed mechanism uses the make-before-break approach when changing the routing path if needed. To avoid the high cost of tunnel setup, we use the same approach in case of consumer mobility. The main reason is that a content is retrieved in the candidate eNodeB before the original handover occurred. In the proposed mechanism, a node acquires the content from the edge network whereas in the other content communication a node acquires the content from a remote network. Therefore, the routing path, cost, and latency in the proposed mechanism are smaller.

4.2. Average Throughput. Figure 8 depicts the average throughput of the prediction-based LTE, CCN-based mobility management mechanism, and our proposed mechanism with the varying number of producers and consumers in random mobility scenarios. The throughput of our proposed mechanism is better and stable as it is able to detect and differentiate losses due to congestion, link failure, and

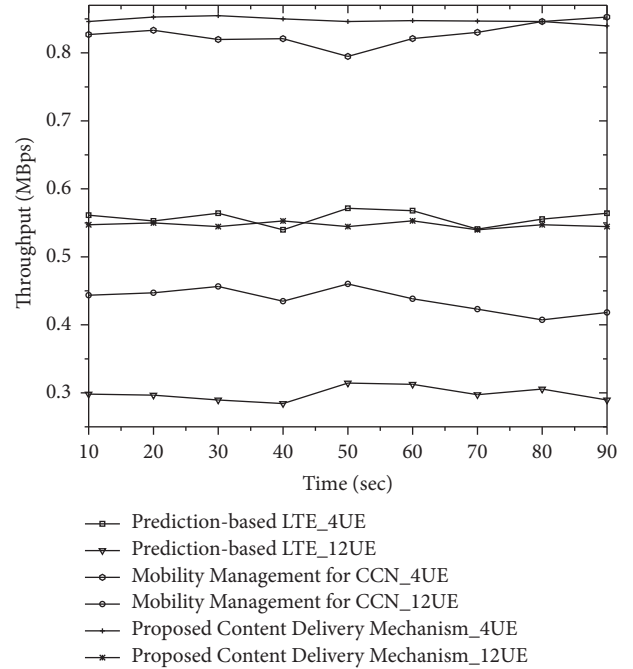


FIGURE 8: Average throughput observed inside the consumer.

mobility. Our in-network buffering capability does not affect the normal operation of the network in case of high mobility, so the throughput rate is always consistent in case of our approach. However, the content delivery rates are hardly affected by mobility and tend to be stable, as shown in Figure 8.

4.3. Data Transmission Success Ratio. We also measured the performance of reachability and continuity of our mechanism in terms of data transmission success ratio, which implies how much data were received correctly by the consumer in the random mobility scenario. The proposed content similarity approach increases the content availability when mobility changes the content location. Also the buffering capability, fast path switch, and handover prediction reduce the packet loss rate. The simulation result showed a significant improvement in this case as illustrated in Figure 9.

5. Conclusion

In this paper, we proposed a novel content delivery mechanism and a mobility management scheme for the evolved communication architecture such as 4G/5G to make the balance between the content diversity and network diversity. We then analyzed the performance of the proposed schemes with the LTE network in the mobile environment. By presenting different simulation results, we showed that the proposed schemes can be used as a possible solution for faster content transmission and seamless content delivery in the mobile environment. It is possible to provide accelerated, reliable, resource-efficient, and cost-effective communication, which will also be helpful for 5G.

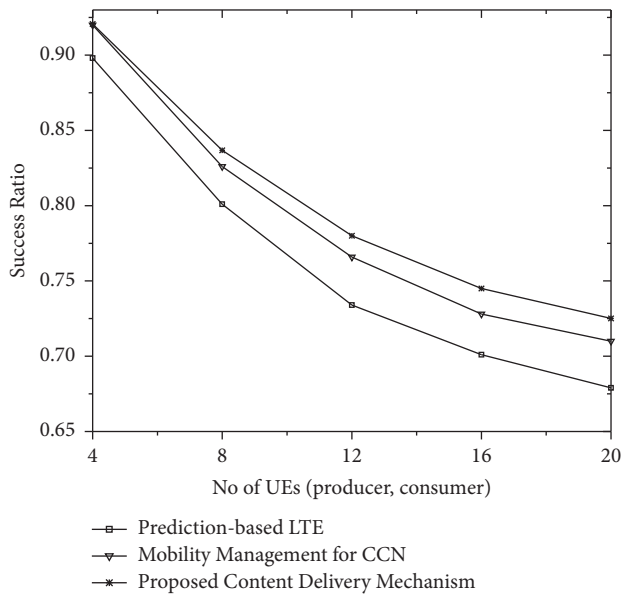


FIGURE 9: Data transmission success ratio.

Data Availability

The simulation parameters and results and other relevant data used to support the findings of this study are included within the article.

Conflicts of Interest

The authors declare that they have no conflicts of interest.

Acknowledgments

This research was financially supported by the Ministry of Trade, Industry and Energy (MOTIE) and Korea Institute for Advancement of Technology (KIAT) through the International Cooperative R&D program. This work was supported by Hankuk University of Foreign Studies Research Fund of 2018.

References

- [1] V. Jacobson, D. K. Smetters, J. D. Thornton, M. F. Plass, N. H. Briggs, and R. L. Braynard, "Networking named content," in *Proceedings of the 5th ACM Conference on Emerging Networking Experiments and Technologies (CoNEXT '09)*, pp. 1–12, December 2009.
- [2] M. R. Bosunia, A. Kim, D. P. Jeong, C. Park, and S.-H. Jeong, "Enhanced multimedia data delivery based on content-centric networking in wireless networks," *Applied Mathematics & Information Sciences*, vol. 9, no. 2, pp. 579–589, 2015.
- [3] D. Le, X. Fu, and D. Hogrefe, "A review of mobility support paradigms for the internet," *IEEE Communications Surveys & Tutorials*, vol. 8, no. 1, pp. 38–51, 2006.
- [4] D. Farinacci, V. Fuller, D. Meyer, and D. Lewis, "Locator/id separation protocol (lisp)," IETF - draft-ietf-lisp-23, 2012.
- [5] T. Koponen, M. Chawla, B.-G. Chun et al., "A data oriented (and beyond) network architecture," *Computer Communication Review*, vol. 37, no. 4, pp. 181–192, 2007.
- [6] C. Dannewitz, D. Kutscher, B. Ohlman, S. Farrell, B. Ahlgren, and H. Karl, "Network of information (NetInf)-An information-centric networking architecture," *Computer Communications*, vol. 36, no. 7, pp. 721–735, 2013.
- [7] M. D'Ambrosio, P. Fasano, M. Marchisio, V. Vercellone, and M. Ullio, "Providing data dissemination services in the future internet," in *Proceedings of the IEEE Global Telecommunications Conference (GLOBECOM '08)*, pp. 1–6, November 2008.
- [8] A. Eriksson and B. Ohlman, "Dynamic internetworking based on late locator construction," in *Proceedings of the IEEE Global Internet Symposium (GI '07)*, pp. 67–72, May 2007.
- [9] D. Trossen and G. Parisi, "Designing and realizing an information-centric internet," *IEEE Communications Magazine*, vol. 50, no. 7, pp. 60–67, 2012.
- [10] P. Jokela, A. Zahemszky, C. E. Rothenberg, S. Arianfar, and P. Nikander, "LIPSIN: Line speed publish/subscribe internetworking," in *Proceedings of the ACM SIGCOMM 2009 Conference on Data Communication (SIGCOMM '09)*, pp. 195–206, August 2009.
- [11] S. DiBenedetto, C. Papadopoulos, and D. Massey, "Routing policies in named data networking," in *Proceedings of the ACM SIGCOMM Workshop on Information-Centric Networking (ICN '11)*, pp. 38–43, August 2011.
- [12] G. Carofiglio, G. Morabito, L. Muscariello, I. Solis, and M. Varvello, "From content delivery today to information centric networking," *Computer Networks*, vol. 57, no. 16, pp. 3116–3127, 2013.
- [13] J. Lee and D. Kim, "Proxy-assisted content sharing using content centric networking (CCN) for resource-limited mobile consumer devices," *IEEE Transactions on Consumer Electronics*, vol. 57, no. 2, pp. 477–483, 2011.
- [14] S. Muhammad, K. Kwangsoo, and C. Seungoh, "Cluster-based Mobility support in Content-centric Networking," *Research Notes in Information Science (RNIS)*, vol. 14, pp. 441–444, 2013.
- [15] H. Feng, Z. Chen, and H. Liu, "Performance analysis of push-based converged networks with limited storage," *IEEE Transactions on Wireless Communications*, vol. 15, no. 12, pp. 8154–8168, 2016.
- [16] I. Loumiotis, P. Kosmidis, E. Adamopoulou, K. Demestichas, and M. Theologou, "Dynamic allocation of backhaul resources in converged wireless-optical networks," *IEEE Journal on Selected Areas in Communications*, vol. 35, no. 2, pp. 280–287, 2017.
- [17] A. Araldo, G. Dan, and D. Rossi, "Caching encrypted content via stochastic cache partitioning," *IEEE/ACM Transactions on Networking*, vol. 26, no. 1, pp. 548–561, 2018.
- [18] L. Rui, S. Yang, and H. Huang, "A producer mobility support scheme for real-time multimedia delivery in named data networking," *Multimedia Tools and Applications*, vol. 77, no. 4, pp. 4811–4826, 2018.
- [19] R. Tourani, S. Misra, and T. Mick, "IC-MCN: An architecture for an information-centric mobile converged network," *IEEE Communications Magazine*, vol. 54, no. 9, pp. 43–49, 2016.
- [20] H. Farahat and H. Hassanein, "Optimal caching for producer mobility support in Named Data Networks," in *Proceedings of the IEEE International Conference on Communications (ICC '16)*, May 2016.

- [21] F. Ren, Y. Qin, H. Zhou, and Y. Xu, "Mobility management scheme based on software defined controller for content-centric networking," in *Proceedings of the INFOCOM International Workshop on Mobility Management in the Networks of the Future World (INFOCOM WKSHPs '16)*, pp. 193–198, San Francisco, Calif, USA, April 2016.
- [22] J. Costa-Requena, M. Kimmerlin, J. Manner, and R. Kantola, "SDN optimized caching in LTE mobile networks," in *Proceedings of the 5th International Conference on Information and Communication Technology Convergence (ICTC '14)*, pp. 128–132, October 2014.
- [23] N. Zhang, M. Kimmerlin, J. Costa-Requena, and H. Hämmäinen, "Cost efficiency of mobile in-network caching," *International Journal of Network Management*, vol. 26, no. 1, pp. 44–55, 2016.
- [24] H. Wang, S. Kao, C. Hsiao, and F. Chang, "A moving direction prediction-assisted handover scheme in LTE networks," *EURASIP Journal on Wireless Communications and Networking*, 2014.
- [25] R. M. Bosunia and S.-H. Jeong, "Efficient mobility support for content delivery in mobile communications," in *Proceedings of the International Conference on Information Networking (ICOIN '17)*, pp. 118–121, 2017.
- [26] P. Vincke, *Multicriteria Decision Aid*, Wiley, 1992.

Research Article

Fuzzy Based Network Assignment and Link-Switching Analysis in Hybrid OCC/LiFi System

Moh. Khalid Hasan , Mostafa Zaman Chowdhury ,
Md. Shahjalal , and Yeong Min Jang 

Department of Electronics Engineering, Kookmin University, Seoul 02707, Republic of Korea

Correspondence should be addressed to Yeong Min Jang; yjang@kookmin.ac.kr

Received 3 August 2018; Accepted 4 November 2018; Published 19 November 2018

Academic Editor: Laurie Cuthbert

Copyright © 2018 Moh. Khalid Hasan et al. This is an open access article distributed under the Creative Commons Attribution License, which permits unrestricted use, distribution, and reproduction in any medium, provided the original work is properly cited.

In recent times, optical wireless communications (OWC) have become attractive research interest in mobile communication for its inexpensiveness and high-speed data transmission capability and it is already recognized as complementary to radio-frequency (RF) based technologies. Light fidelity (LiFi) and optical camera communication (OCC) are two promising OWC technologies that use a photo detector (PD) and a camera, respectively, to receive optical pulses. These communication systems can be implemented in all kinds of environments using existing light-emitting diode (LED) infrastructures to transmit data. However, both networking layers suffer from several limitations. An excellent solution to overcoming these limitations is the integration of OCC and LiFi. In this paper, we propose a hybrid OCC and LiFi architecture to improve the quality-of-service (QoS) of users. A network assignment mechanism is developed for the hybrid system. A dynamic link-switching technique for efficient handover management between networks is proposed afterward which includes switching provisioning based on user mobility and detailed network switching flow analysis. Fuzzy logic (FL) is used to develop the proposed mechanisms. A time-division multiple access (TDMA) based approach, called round-robin scheduling (RRS), is also adopted to ensure fairness in time resource allocation while serving multiple users using the same LED in the hybrid system. Furthermore, simulation results are presented taking different practical application scenarios into consideration. The performance analysis of the network assignment mechanism, which is provided at the end of the paper, demonstrates the importance and feasibility of the proposed scheme.

1. Introduction

Communication currently relies on the radio-frequency (RF) spectrum, which is overcrowded and strictly regulated [1]. Because of several factors including interference, limited resources, and human safety it is obvious that RF based technologies will not be sufficient to manage the massive future data traffic. Wireless communication using the optical spectrum has been regarded as a congruent solution to the spectrum congestion of RF based technologies [2–6]. In particular, the optical wireless technology, especially visible light communication (VLC), has added a new dimension in the world of mobile communications for its huge unregulated spectrum (up to 800 THz [7]), cost effectiveness, energy efficiency, and high security [3, 8, 9]. Moreover, current indoor and outdoor environments are currently heavily congested

with light-emitting diode (LED) based lighting infrastructures, enabling VLC to be exploited as a complementary technology to RF.

Light fidelity (LiFi) is a subset of OWC technology in which a photo detector (PD) receives the variation in the intensity of light, which carries data bits encoded from the light source [3, 10, 11]. A PD can detect high-speed LED flickering, a capability that enables LiFi to support high data rates. An extensive improvement in bandwidth reuse is observed for LiFi technologies, resulting in excellent spectral efficiency. Because of these benefits provided by LiFi, several architectures integrating LiFi and RF have been already proposed to enhance the quality-of-service (QoS) of users; these architectures include those that manage resource allocation [12–15], dynamic handover [16, 17], energy harvesting [18], delay analysis [19], and channel assignment [20].

However, LiFi cannot be efficiently utilized in daylight because it suffers from extensive interference generated by sunlight [3]. In indoor environments, it can suffer from the same problem resulting from neighboring lighting infrastructures. LiFi has a low signal-to-interference-plus-noise ratio (SINR) because it is heavily affected by the interferences generated by adjacent light sources. In addition, the communication distance that can be obtained using LiFi is comparatively short with respect to other existing technologies. These limitations inspire further research on the optimum potentiality of LiFi in practical environments.

Optical camera communication (OCC) is a recently introduced VLC technique that uses an image sensor to receive optical signals [21–26]. The exponential growth in camera-mounted smart devices has enabled OCC to be utilized in innovative application scenarios, such as indoor/outdoor positioning [27, 28], localized advertising [29], digital signage, and vehicle-to-vehicle (V2V) or vehicle-to-infrastructure (V2I) communications [30–32]. OCC has added significant user flexibility with the use of smartphone cameras to receive data from LEDs. Furthermore, OCC is highly stable in terms of variations in communication distance. Because of the limited angle-of-view (AoV) of cameras, OCC is less affected by interferences generated from neighboring LEDs. However, similar to LiFi, OCC has several limitations. For example, because of the meager sampling rates of current commercial cameras, OCC offers a low data rate, which particularly decreases the user QoS.

Until now, a hybrid OCC and LiFi model had not been developed. In this study, a hybrid networking architecture integrating OCC and LiFi is proposed to enhance the user QoS. The network is assigned to users through utilization of fuzzy logic (FL). FL is a convenient approach to map an input to an output and is provided on the basis of several truth scores ranging from 0 to 1 [33]. This method is flexible and intuitive without far-reaching complexity, which are characteristics that lead us to choose this approach. We propose a new network assignment mechanism inside the LED cell (the entire coverage area of the LED) for users. Fuzzy inputs are chosen using the parameters that determine the quality of both networks. The fuzzy rules are generated by considering real-world application scenarios of users. The center-of-gravity (CoG) method is used to defuzzify the inputs and obtain mark allocations for each user. Furthermore, we develop a FL-based vertical link-switching mechanism between the networking layers, as both of the networks support user mobility. We briefly discuss the switching probability and corresponding network switching flow analysis of the hybrid system. Round-robin scheduling (RRS) [34], an existing time-division multiple access (TDMA) approach, is adopted to ensure fairness in resource allocation among users.

The remainder of the paper is organized as follows: Section 2 provides a system overview and an analysis on channel parameters, which includes theoretical representations of SINR for both technologies. The FL-based network assignment mechanism, including a discussion on user QoS, is explained in Section 3. Sections 4 and 5 describe the link-switching strategy and the network switching flow process,

respectively. The performance of the assignment mechanism is evaluated in Section 6, which also includes a discussion of the outage probability and QoS performance. A brief summary of our work is provided in Section 7. Finally, Section 8 presents future research possibilities related to our proposed hybrid infrastructure.

2. System Overview

2.1. Hybrid System Architecture. In this study, a hybrid OCC/LiFi networking layer is considered. Taking user mobility into account, this hybrid system can serve multiple users. Therefore, the hybrid system is suitable for any roaming or stationary user. A particular LED is configured by two parallel LED-driving circuitries. Although both technologies use the same optical spectrum, no interference will be generated because the TDMA based RRS method is exploited to allocate time resources when there are multiple users. A generalized block diagram of our proposed architecture is shown in Figure 1. The PD can receive high-rate LED flickering, whereas a camera cannot. Current commercial cameras are configured with low frame rates (in most cases, 30–50 frames per second). This configuration particularly reduces the modulation bandwidth of OCC [35, 36]. It is also worth noting that the LED flickering must not be observed by human eyes (equivalent to a threshold of approximately 100 Hz [37]).

2.2. OCC Channel Model. For a VLC system, the route for optical signal transmission has two components: line-of-sight (LOS) and non-line-of-sight (NLOS). Because of the nature of camera pixels, region-of-interest (RoI) mechanisms are applied for OCC, by which the reflection component of the transmitted signal is spatially separated from the LOS component [23]. An indoor hybrid system with the transmitter and receiver presented at T_x and R_x , respectively, is illustrated in Figure 2. The LED cell represents the entire coverage area of the LED.

The LOS channel for optical signal transmission is modeled by Lambertian radiant intensity, which is represented by the following equation [38]:

$$R_o(\alpha) = \frac{(m_l + 1) \cos^{m_l}(\alpha_{ir})}{2\pi} \quad (1)$$

where α_{ir} signifies the angle of irradiance of the LED. m_l is the Lambertian emission index, which originates from the radiation angle $\Psi_{1/2}$, called the radiation semiangle of the LED; m_l is defined as

$$m_l = -\log_{\cos \Psi_{1/2}} 2 \quad (2)$$

We assume that the Euclidean distance between T_x and R_x is $d_{a,b}$, which is calculated from the horizontal distance $d_{b,x}$ and the vertical distance $d_{a,h}$ ($d_{a,b} = \sqrt{d_{a,h}^2 + d_{b,x}^2}$). The overall DC channel gain for OCC is formulated as [12]

$$H_{t,r}^{IS} = g_{op} \cos(\alpha_{in}) \Delta_{occ} \frac{R_o(\alpha) A_c}{d_{a,b}^2} \quad (3)$$

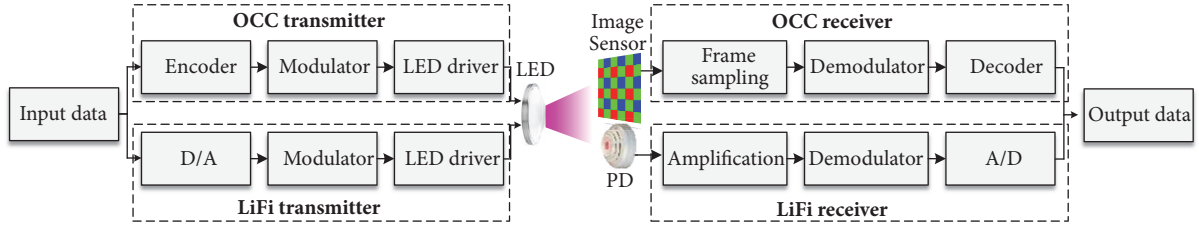


FIGURE 1: Basic block diagram of the hybrid OCC/LiFi architecture.

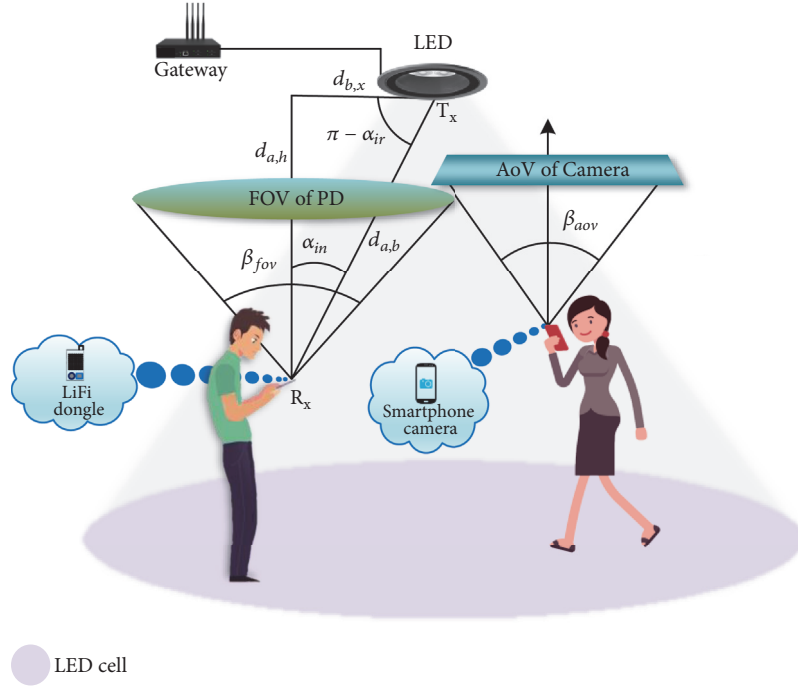


FIGURE 2: Data transmission model for the hybrid network.

where α_{in} implies the corresponding angle of incidence, g_{op} represents the gain of the optical filter, and Δ_{occ} is a rectangular function whose value implies that the channel has no gain if the LED remains outside of the angle-of-view (AoV) of camera receiver. If β_{aov} is the AoV of the camera, then Δ_{occ} is represented as

$$\Delta_{occ} = \begin{cases} 0, & \alpha_{in} \geq \beta_{aov} \\ 1, & \alpha_{in} < \beta_{aov} \end{cases} \quad (4)$$

A_c is the area of the entire image of the LED projected in the image sensor. It is often signified by the number of pixels occupied by the image. If ρ denotes the pixel edge length, then the projected area is

$$A_c = \frac{A_l f_o^2}{\rho^2 d_{a,b}^2} \quad (5)$$

where f_o denotes the focal length of the camera and A_l represents the physical area of the LED.

There is a minimum area of the projected image in the image sensor, below which the transmitted data cannot be

decoded. The power received by the image sensor in this case is termed as the threshold power and expressed as

$$\begin{aligned} P_{th}^{IS} &= \arg \min P_r^{IS} \\ &= \arg \min \left[g_{op} \cos(\alpha_{in}) \Delta_{occ} \frac{R_o(\alpha) A_c P_t}{d_{a,b}^2} \right] \end{aligned} \quad (6)$$

where P_r^{IS} is the power received by the image sensor and P_t denotes the optical power transmitted by the LED.

Most existing commercial cameras offer a low AoV. As a result, the LOS components of neighboring LEDs do not reach inside the camera's AoV. Moreover, as mentioned above, introducing RoI signaling techniques significantly reduces the effect of the reflected components. Thus, OCC offers an excellent SINR, which is represented as

$$SINR_{occ} = \frac{(\zeta_c P_t H_{t,r}^{IS})^2}{\sum_{i=0}^N (\zeta_c P_t H_{i,r}^{occ})^2 + N_o f_r} \quad (7)$$

where ζ_c denotes the optical-to-electrical conversion efficiency at the image sensor, N_o is the spectral density of the

noise power, f_r is the sampling rate of the camera, N is the number of interfering transmitters, and $H_{i,r}^{occ}$ is the DC gain from these transmitters. The channel capacity can be expressed by the Shannon capacity formula [23], which is

$$C_{occ} = f_r W_s \log_2 (1 + SINR_{occ}) \quad (8)$$

where W_s represents the number of data symbols transmitted to the pixels within each image frame.

2.3. LiFi Channel Model. The NLOS part of the transmitted signal is disregarded in terms of LiFi because our baseband modulation bandwidth B is 20 MHz, which does not exceed the maximum allowable value [16, 39]. Thus, the LOS transmission model for LiFi is represented as

$$H_{t,r}^{PD} = g_{op} g_{con} \cos(\alpha_{in}) \Delta_{lifi} \frac{R_o(\alpha) A_p}{d_{a,b}^2} \quad (9)$$

where A_p denotes the physical area of the PD sensitive to light and g_{con} is the gain of the optical concentrator, which is a function of the refractive index and field-of-view (FoV) of PD. The rectangular function Δ_{lifi} is expressed as

$$\Delta_{lifi} = \begin{cases} 0, & \alpha_{in} \geq \beta_{fov} \\ 1, & \alpha_{in} < \beta_{fov} \end{cases} \quad (10)$$

where β_{fov} denotes the PD FoV. The PD should receive a certain amount of power to generate a minimum electrical current in order to decode the actual sent data bits. The threshold power of LiFi is denoted as

$$\begin{aligned} P_{th}^{PD} &= \arg \min P_r^{PD} \\ &= \arg \min \left[g_{op} g_{con} \cos(\alpha_{in}) \Delta_{lifi} \frac{R_o(\alpha) A_p P_t}{d_{a,b}^2} \right] \end{aligned} \quad (11)$$

where P_r^{PD} denotes the total amount of power received by the PD. LiFi uses an intensity based modulation scheme; as such, LiFi is affected by the interference generated by neighboring LEDs and other background lights. This interference ultimately results in reducing the SINR to a great extent, as LED infrastructures are commonly developed for indoor environments. Several studies [16, 40] have investigated the SINR in terms of LiFi, which can be expressed as

$$SINR_{lifi} = \frac{((\zeta_p \sqrt{P_e}/P_t) P_t H_{t,r}^{PD})^2}{\sum_{i=0}^N ((\zeta_p \sqrt{P_e}/P_t) P_t H_{i,r}^{PD})^2 + N_o B} \quad (12)$$

where ζ_p is the optical-to-electrical conversion efficiency at the PD and P_e is the amount of electrical power converted after receiving the optical signals. The LiFi channel capacity can also be calculated from the Shannon capacity formula, which is

$$C_{lifi} = B \log_2 (1 + SINR_{lifi}) \quad (13)$$

3. FL-Based Network Assignment

Inside the hybrid network, the network is selected according to the type of service and quality that the user requires. FL is dispensed to assign a particular user to a network. Instead of making decisions for choosing a network in a hybrid system in terms of Boolean logic (only true or false values), the FL-based assignment considers truth values of variables ranging from 0 to 1 [33, 41–43]. We apply the Mamdani fuzzy inference system to evaluate our proposed scheme; this system includes three principal steps: fuzzification of input variables, rules evaluation, and defuzzification.

Fuzzification refers to the process of transforming the crisp inputs into degrees of functional blocks through using the different types of fuzzifiers, called membership functions. A fuzzy set is graphically represented by membership functions. For example, a triangular function is presented in Figure 3(a) and described as

$$\mu(x; a_T, b_T) = \begin{cases} 0, & x \leq a_T \text{ [Red line]} \\ \frac{x - a_T}{b_T - a_T}, & a_T \leq x \leq b_T \text{ [Blue line]} \\ 1, & x \geq b_T \text{ [Green line]} \end{cases} \quad (14)$$

where a_T and b_T are the breakpoints of the membership functions and x is a particular input.

We considered four input variables to perform the network assignment mechanism: data rate requirement, SINR requirement, amount of instantaneous received power, and LOS Euclidean distance between the access point (AP) and the receiver. The variables are chosen on the basis of application scenarios. For example, if a user wants to localize its position, it will definitely need an excellent SINR rather than high data rate to minimize the localization resolution. On the contrary, both data rate and SINR must be high for a real-time video call. Moreover, the instantaneous power significantly contributes to determining the bit-error performance of connectivity. In addition, a low received power degrades the user's QoS level by increasing the outage probability to a great extent. On the other hand, the maximum communication distance varies for different optical wireless systems and user achieves satisfactory QoS when the communication distance is short. A long distance between the LED and receiver increases the interference for LiFi, although OCC is less affected by interference. In particular, the maximum communication distance for LiFi is very short compared to OCC for stable communications.

The membership functions are chosen on the basis of several experiments involving the use of training data. The grades of the membership functions are assigned according to the effect of variations in the value of a particular input. Figure 3(b) shows an illustration of the fuzzification of the SINR requirement of a specific user on the basis of service type and quality. The procedure is characterized by four different membership grades: low, average, high, and excellent. These grades are distributed from -10 to 60 dB. As shown in

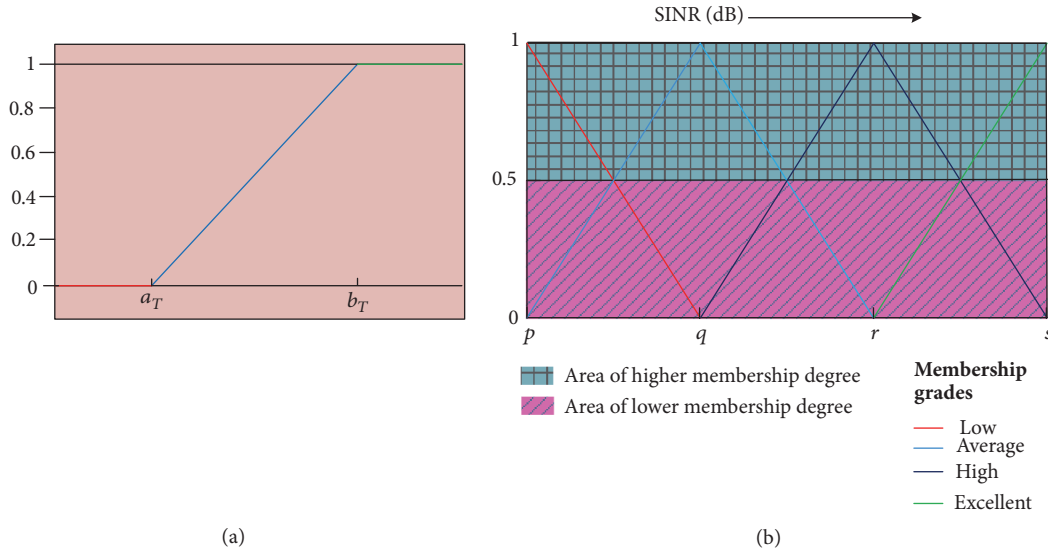


FIGURE 3: Fuzzification process: (a) a generalized triangular function; (b) SINR requirement.

Figure 3(b), the four membership grades can be represented in a similar approach, which is

$$\begin{aligned}
 \text{Low} &\longrightarrow \mu(x; p, q), \quad x \geq p \\
 \text{Average} &\longrightarrow \begin{cases} 1 - \mu(x; p, q), & x > p \\ \mu(x; q, r), & x \geq q \end{cases} \\
 \text{High} &\longrightarrow \begin{cases} 1 - \mu(x; q, r), & x > q \\ \mu(x; r, s), & x \geq r \end{cases} \\
 \text{Excellent} &\longrightarrow 1 - \mu(x; r, s), \quad x < s
 \end{aligned} \tag{15}$$

The chosen SINR values of the breakpoints are -10 , 10 , 30 , and 40 dB. For example, if a user requires an SINR of around 25 dB, then the user will be categorized as “average” in the fuzzification process. Other inputs are fuzzified through a similar approach. However, the status of the membership grades is varied according to the numerical information of the input variables. For example, the data rate requirement is fuzzified through three membership grades: low, average, and high.

After fuzzifying the inputs, different rules are used to evaluate the performance of the hybrid system [41]. These if/then rules are generated by assigning a membership grade to each of the input variables, and a decision is made after multiplying (also can be referred to as “and” operation) the rules. For example, if the data rate requirement is low, the SINR requirement is excellent, and the instantaneous receive power is medium, then the user will be connected via LiFi for the shortest distance between the light source and receiver (or OCC for the highest distance). It is worth noting here that the rules are comprehensive and are generated keeping the nature and quality of the user requirements in mind. In general, rules are the guidelines generated according to the

membership functions and serve as a basis for why we choose a particular network in a specific kind of service scenario.

The network assignment procedure is illustrated in Figure 4. The user must remain inside the LED cell in order to get connected via LiFi or OCC. However, the connection possibility significantly depends on the FoV or AoV offered by the PD or camera, respectively. Because the effects of the NLOS components on the optical signal are disregarded, the LED must appear inside the coverage area of the receiver. After getting a new network access request (NAR) from the user, the service type will be investigated. The examination on the input variables will be initiated immediately following the investigation. Then, the system will go through the fuzzification process described earlier.

Subsequently, the rules are employed and evaluated. The last stage of the network assignment mechanism is the mark allocation, a process that is also referred to defuzzification. The mark indicates the possibility of choosing a network in the network assignment process. Two separate outputs are considered for LiFi and OCC. Both outputs are characterized with triangular membership functions. We have considered five membership grades for each output to obtain a precise result in the network selection mechanism. In this paper, the mark is termed as network assignment factor (NAF) and denoted as ϑ_{lifi} and ϑ_{occ} for LiFi and OCC, respectively. We have adopted CoG [33] method for defuzzification because it shows better performance results than the bisector-of-area (BoA) method, which is realized through several experiments on training data. The NAF is provided as a crisp value by the CoG method, which is represented as

$$\begin{aligned}
 \text{For LiFi, } \vartheta_{\text{lifi}} &= \frac{\int_0^1 z \mu_l(z) dz}{\int_0^1 \mu_l(z) dz} \\
 \text{For OCC, } \vartheta_{\text{occ}} &= \frac{\int_0^1 z \mu_c(z) dz}{\int_0^1 \mu_c(z) dz}
 \end{aligned} \tag{16}$$

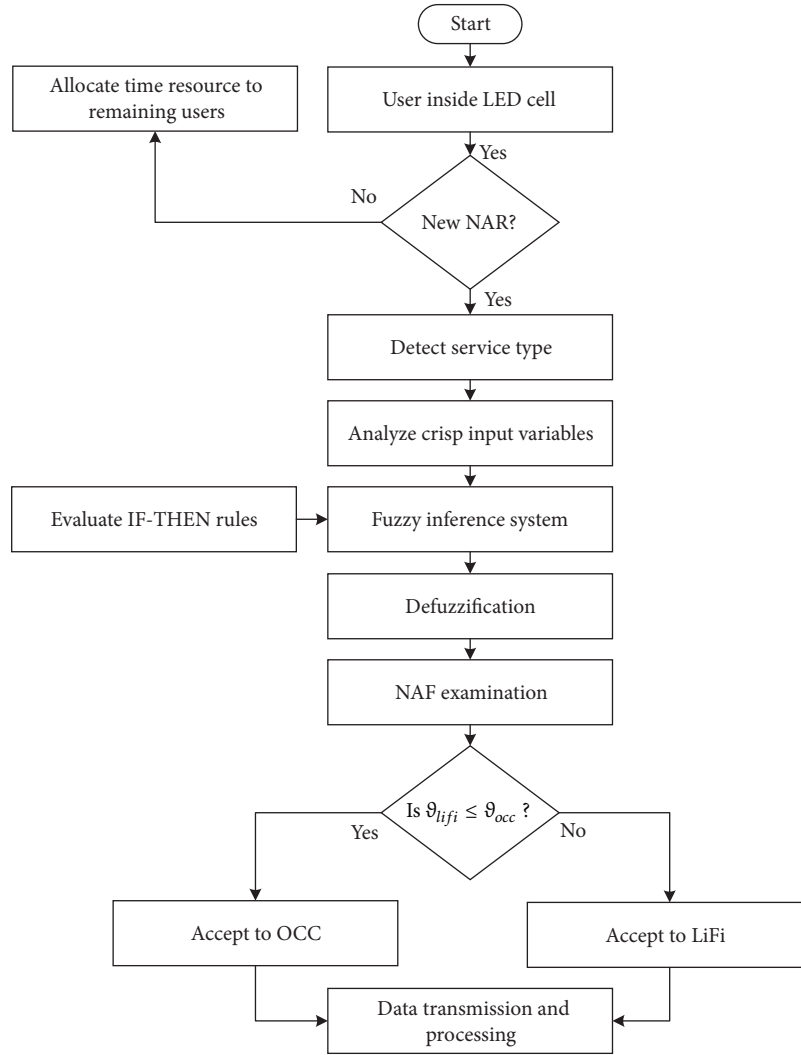


FIGURE 4: Admission strategy for a new network access request.

where $\int_0^1 \mu_i(z) dz$ indicates the total area of the region after combining all the membership functions. NAF values range from 0 to 1. In fact, a higher NAF increases the possibility of choosing a network. Thus, when a network access is requested by a new user, the NAFs of both networks will be compared. The network with the higher NAF will be chosen. For example, if LiFi achieves an NAF of 0.6 for a new user, whereas OCC obtains 0.8, then the user will be connected to OCC instead of LiFi.

When multiple users want to connect to the same AP and RRS [34], a TDMA technique is considered. Each user is allocated a particular time slot, referred to as quantum time, to ensure fairness among all users. If the process of serving the user is not entirely executed within that time slot, the process will resume after completing all other processes in the queue. Figure 5 illustrates an RRS scheduling process, in which four users want to get access from the serving light source. The process for LiFi user-2 does not finish within the allocated time slot, it gets connected again after the other time slots allocated in the queue have been completed.

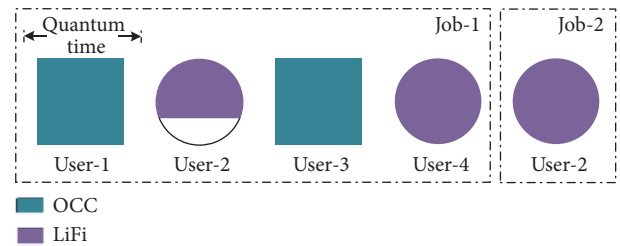


FIGURE 5: Example of RRS scheduling process.

The user QoS is measured considering achievable user data rate and SINR. We develop a parameter, referred as demand satisfaction factor (DSF), to analyze the QoS of users. If the user achieves a lower data rate or SINR than it requires, the DSF will be decreased. In general, DSF is calculated on the basis of time resource allocation to each user. The DSF of a particular user is represented as follows:

$$DSF = \begin{cases} \left(1 - \frac{n}{N_t}\right) \left(\frac{\lambda}{\sigma_i}\right) \frac{\varphi_{ai}\chi_{ai}}{\varphi_{ri}\chi_{ri}}, & \{\lambda < \sigma_i\} \& \{\varphi_{ai} < \varphi_{ri}\} \& \{\chi_{ai} < \chi_{ri}\} \\ \frac{\varphi_{ai}\chi_{ai}}{\varphi_{ri}\chi_{ri}}, & \{\lambda \geq \sigma_i\} \& \{\varphi_{ai} < \varphi_{ri}\} \& \{\chi_{ai} < \chi_{ri}\} \\ \frac{\chi_{ai}}{\chi_{ri}}, & \{\lambda \geq \sigma_i\} \& \{\varphi_{ai} \geq \varphi_{ri}\} \& \{\chi_{ai} < \chi_{ri}\} \\ \frac{\varphi_{ai}}{\varphi_{ri}}, & \{\lambda \geq \sigma_i\} \& \{\varphi_{ai} < \varphi_{ri}\} \& \{\chi_{ai} \geq \chi_{ri}\} \\ \varphi_{ri}, & \{\lambda \geq \sigma_i\} \& \{\varphi_{ai} \geq \varphi_{ri}\} \& \{\chi_{ai} \geq \chi_{ri}\} \\ 1, & \end{cases} \quad (17)$$

where φ_{ai} and φ_{ri} indicate the achievable and required data rate, respectively, and χ_{ai} and χ_{ri} indicate the achievable and required SINR, respectively. λ and σ_i represent the quantum time and burst time of the user, respectively. n indicates the total number of users waiting in queue at the particular time and N_t is the maximum number of users that can be connected inside the LED cell.

4. Link-Switching Strategy

It is already known that LiFi suffers from more interference than OCC. This interference can originate from the LOS component of other light sources or other components reflected from painted walls or mirrors. For simplicity, we assume an indoor scenario, in which a user can be connected to several LEDs. It is obvious that the user device will be affected by the LOS component of the neighboring LED near the edge of the LED cell. Thus, if just under the LED cell, the user will suffer the least amount of interference and will receive the best SINR. Therefore, the probability of allocation to the LiFi network will be high. If the user appears to be connected with OCC at that time, the probability of link-switching to LiFi will also be high because the final goal of network allocation is increasing the user QoS as much as possible. In the same way, if the user goes too close to the edge of the LED cell, then the probability of switching from a LiFi to an OCC network will be high. Figure 6 shows two LED cells, each having a diameter of ν . If $\gamma\%$ of the diameter of a specific LED cell is covered by a neighbor LED cell, the probability of user devices interfering with the neighbor LED within an LED cell will be

$$P_j = \sum_{j=1}^{\tau} \left[\frac{2\varepsilon \int_{(\nu-2\gamma\nu)/2}^{\nu/2} \sqrt{\nu^2 - 4z^2} dz}{\tau\pi\nu^2} \right] \quad (18)$$

where ε is the total number of neighbor LED cells interfering with the serving LED cell and τ is the total number of user devices inside the cell. Thus, whenever the LOS distance between the LED AP and the receiver changes, the link-switching probability of either network will also be changed according to the user service requirements. The network assignment for the network switching request can be performed in two ways: LiFi-to-OCC and OCC-to-LiFi switching.

The link-switching can be implemented within either the same LED AP or different APs. Figure 7 shows the switching policy for OCC-to-LiFi. Initially, the user communicates

using the OCC network. Then, the condition of the user will be investigated, i.e., whether the user is remaining static or roaming around the LED cells. The LOS distance from the LED AP to the camera will change for every microsecond for the moving user. Therefore, there will be chance for the camera to receive power below P_{th}^{IS} . In this case, communication between the user and LED AP will terminate. The immediate received power will be compared with P_{th}^{IS} , and when the power exceeds the threshold value, the LiFi received power will be immediately compared with P_{th}^{PD} . If the received power is higher than the threshold, then the user will be connected to LiFi. However, if the received power is also below threshold, the user will be connected to the adjacent AP and follow a new NAR strategy. There is a high possibility for a static user to switch between service and quality requirements. For example, the user can switch from 360p to 1080p video calling, or can stop real-time communication and start browsing. For this reason, whenever the user switches between different services, the NAF will be investigated. If NAF is found decreasing, then it will be compared to that of LiFi. If LiFi offers a higher NAF than OCC, then the user will be switched to LiFi. A similar strategy will be followed for LiFi-to-OCC switching, which is shown in Figure 8.

5. Network Switching Flow Process

In this section, we propose a detailed network switching flow mechanism for the hybrid system. The flow procedure is generalized and applicable to either OCC-to-LiFi or LiFi-to-OCC switching. The flow mechanism is illustrated in Figure 9.

The switching flow mechanism is implemented through 25 steps. When the user device senses that the NAF of the serving receiver (SR) is decreasing (step-1), it sends a report to the serving AP (SAP) it is connected to (step-2). The SR then searches for new signals (step-3), and the SAP by which the user will be connected to the target receiver (TR) is selected (step-4). Then the preauthentication is checked by the receiver with the target AP (TAP) (step-5). On the basis of the preauthentication and the NAF, the SR investigates the signal quality. Together, the SAP and SR decide if a switch to the TAP should be executed (step-6). The SAP initiates the switching process by sending a request to the TAP via a gateway (steps-7 and 8). Network assignment control (NAC) is initiated to specify the possibility of whether or not the network can be assigned (step-9). Afterward, the TAP responds to the switching request (steps-10 and 11). Then, a

TABLE I: System parameters for the simulation.

Transmitter parameters	
LED radius	5 cm
Transmitted optical power, P_t	10 W
Half-intensity radiation angle, $\Psi_{1/2}$	60°
Gain of optical filter, g_{op}	1.0
LiFi parameters	
Physical area of PD	1 cm^2
Gain of optical concentrator, g_{con}	1.5
Optical-to-electrical conversion efficiency, ζ_p	0.53 A/W
Optical bandwidth, B	20 MHz
FoV, β_{fov}	85°
OCC parameters	
Image sensor size	6×4 (3:2 aspect ratio)
Pixel edge length, ρ	$2 \mu\text{m}$
Frame rate, f_r	30 fps
Focal length, f_o	6 mm
Optical-to-electrical conversion efficiency, ζ_c	0.51 A/W
AoV (diagonal), β_{aov}	60°

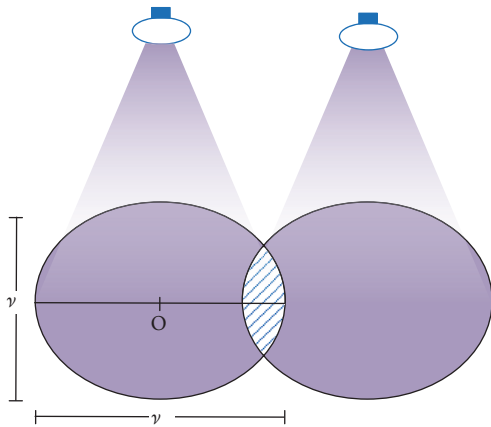


FIGURE 6: Illustration of two adjacent LED cells.

new link is set up between the TAP and gateway (steps-12 to 15), and eventually, packet data are forwarded to the TAP (step-16). An optical channel is reestablished with the TAP (step-17), reconfigured (steps-18 to 20) and finally detached from the SAP and synchronized with the TAP (step-21). The SR then sends a signal to the gateway, indicating the completion of the switching mechanism and synchronization with the TAP (steps-22 and 23). Finally, the optical link between the former SAP and gateway is deleted (steps-24 and 25), and the packets are sent to the TR via the TAP.

6. Performance Evaluation

In this section, the network assignment mechanism is simulated considering the system parameters summarized in Table 1. The hybrid system can be implemented in indoor and outdoor environments. OCC is particularly preferred in

daylight, and both LiFi and OCC can be utilized during the nighttime. We performed the simulations while considering the maximum communication distance of LiFi and OCC. When the LOS distance is high, OCC is slightly more preferred than LiFi.

Figures 10 and 11 show how the NAFs vary with increasing communication distance for both LiFi and OCC. The considered fuzzy rules are arranged in Table 2. The simulations are particularly based on the different service scenarios of users. For example, in case a user wants to localize its position, the service does not need a high data rate; rather, it requires a least bit-error rate for precise localization. This case is considered in Scenario-A. A user who wants to browse websites is reflected in Scenario D. Scenarios B and C indicate high-quality voice and video calling users, and Scenarios E and F reflect the standard quality.

As shown in Figure 10, LiFi achieves an NAF higher than 0.5 when the communication distance is kept within 6 m in all cases. The main reason that LiFi works in a limited communication distance is because of the optical signal receiving characteristics of PDs. OCC provides a good NAF for all cases except high-quality voice and video calling users because of its data rate limitation, which is shown in Figure 11.

For mobility supporting characteristics of LiFi and OCC technologies, our proposed hybrid system also ensures efficient switching between networks based on the service scenarios. The switching is very essential, as the size of the LED cell is very small, and our current indoor environment is decorated with numerous LED infrastructures. Link-switching is initiated whenever the receive power of the serving network falls below the threshold value. Figure 12 illustrates the power received by the users from different distances from LED AP.

The link-switching probability of OCC and LiFi is illustrated in Figure 13. The probability is measured considering

TABLE 2: Selected fuzzy rules for different scenarios.

Scenarios	Req. data rate	Req. SINR	Ins. receive power
A	Low	Excellent	Medium
B	Average	High	High
C	High	Excellent	High
D	Average	Poor	Low
E	Average	Average	High
F	Average	High	High

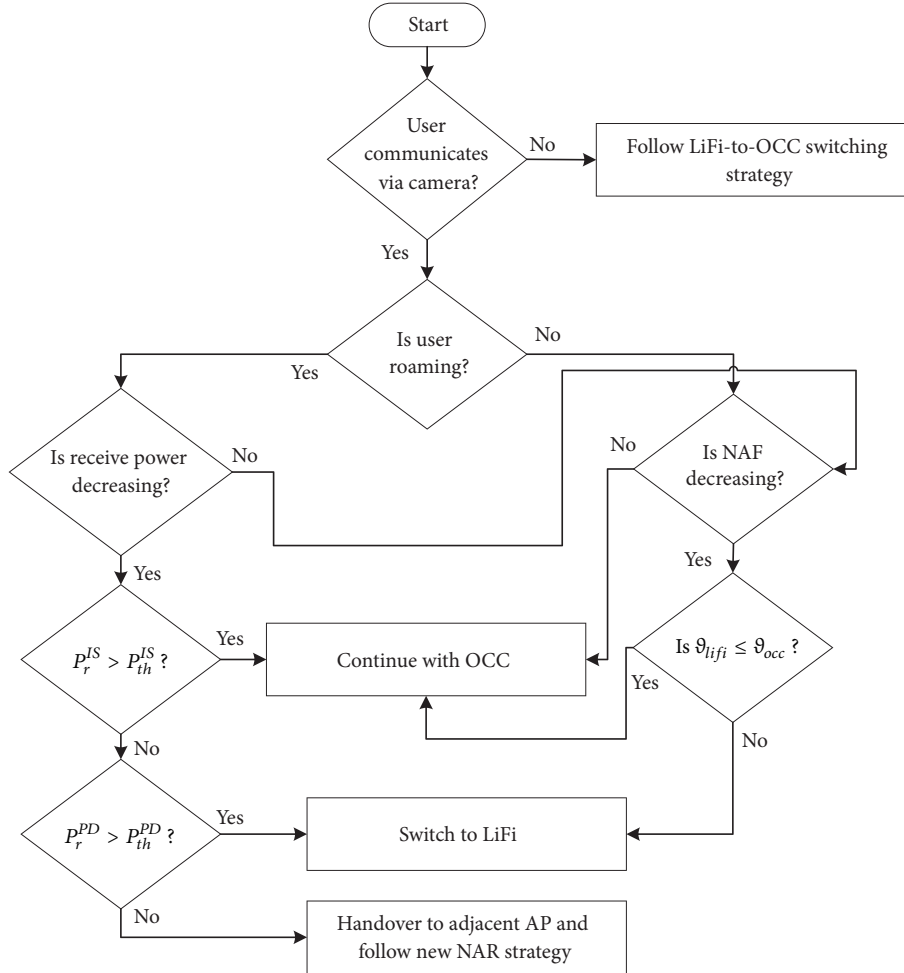


FIGURE 7: OCC-to-LiFi link-switching strategy.

an indoor scenario in which the diameter of the LED cell is 10 m. The link-switching probability is illustrated in terms of probability of user position inside the LED cell to receive highest optical signal. The highest position probability inside the LED cell corresponds with a user situated at the center of the LED cell (represented by O in Figure 6), and the lowest probability corresponds with a user located at the edge of the LED cell. It can be seen in Figure 13 that a user has a high probability of switching from LiFi-to-OCC when it remains near the LED cell origin. However, the probability decreases whenever the user comes close to the LED cell of the neighboring LED. The OCC-to-LiFi handover probability

attains the inverse situation because of the capability of the camera to spatially separate the interfering element from the image sensor.

Figure 14 illustrates the outage probability of our proposed hybrid scheme. We set the threshold of the LiFi SINR as 0 dB for the simulation. We can clearly see that the outage probability is higher when the user moves away from the AP in terms of using LiFi only. However, after integrating OCC and LiFi, a clear improvement in outage possibility can be observed. The QoS performance of users is presented in Figure 15. The average DSF is measured assuming 0.16 persons/meter² can be served inside the LED

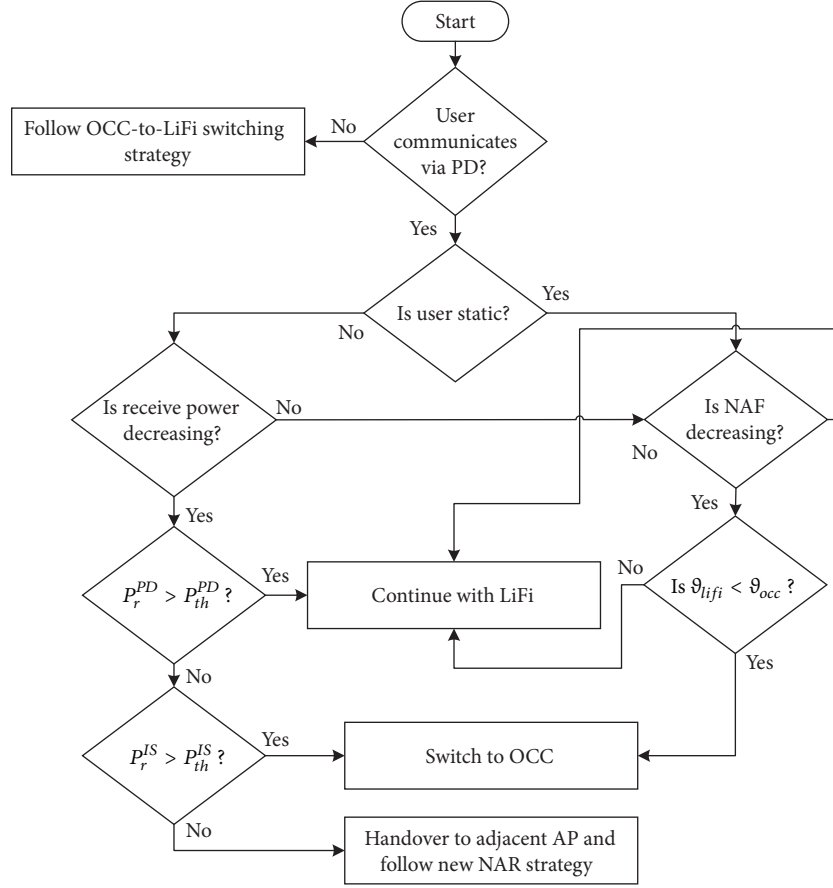


FIGURE 8: LiFi-to-OCC link-switching strategy.

cell. We also assume the number of users connected to OCC and LiFi in the hybrid infrastructure are same. Although the performance greatly depends on how much time is allocated to each user, our proposed scheme demonstrates better QoS performance than the case when only LiFi is present.

7. Conclusions

Next generation VLC networks will be exploited to achieve a higher service quality for users in all kinds of environments. One of the main advantages of using VLC is that existing lighting infrastructures can be utilized to send data to users. LiFi is a OWC technology that offers a high data rate. However, it suffers from interferences when there are multiple light sources, and the interference originated from these sources eventually degrades the service quality. Using OCC, the SINR can be significantly improved in all kinds of scenarios. Thus, the combination of high data rate and high SINR can be achieved by integrating OCC and LiFi. A hybrid OCC and LiFi architecture is proposed in this paper in which the network assignment for each user is based on FL. By using the FL concept, optimality can be achieved with less computational complexity. After defuzzification, each network generates a score called NAF, which is utilized to assign

the appropriate network to a particular user. Furthermore, a link-switching mechanism based on FL is proposed, and a network switching flow analysis is provided. Performance is evaluated on the basis of different practical scenarios, and this evaluation includes switching and outage probability analysis inside the LED cell. The user QoS is also analyzed, and the results of this analysis demonstrate the importance of our proposed scheme.

8. Future Research

Currently, researchers are working on enabling the coexistence of RF and OWC to achieve high-data-rate output with improved coverage. The coexistence of different OWC technologies for the same kind of AP can be utilized to achieve a better service quality for users. The implementation of our proposed hybrid system in different application scenarios will be a momentous topic in future OWC related research, which will include testing our system's optimality with respect to other future homogenous hybrid infrastructures.

Data Availability

The data used to support the findings of this study are available from the corresponding author upon request.

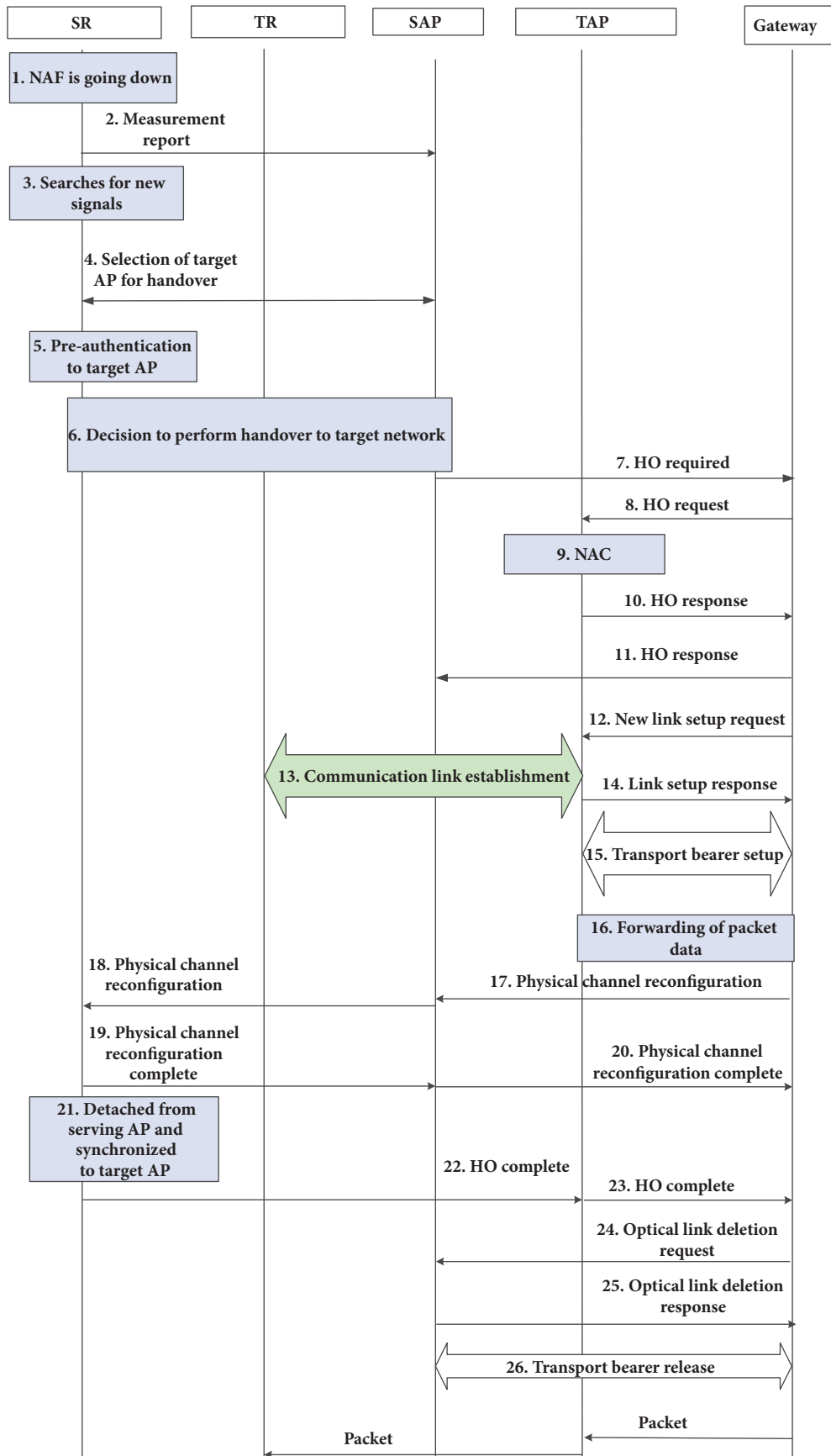


FIGURE 9: Network switching flow strategy.

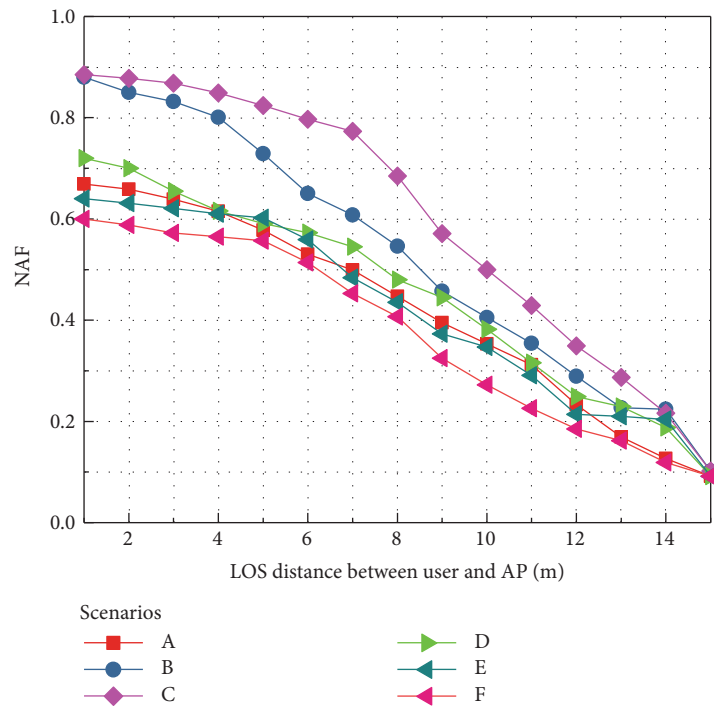


FIGURE 10: NAF variation using LiFi with increasing distance between user and LED AP.

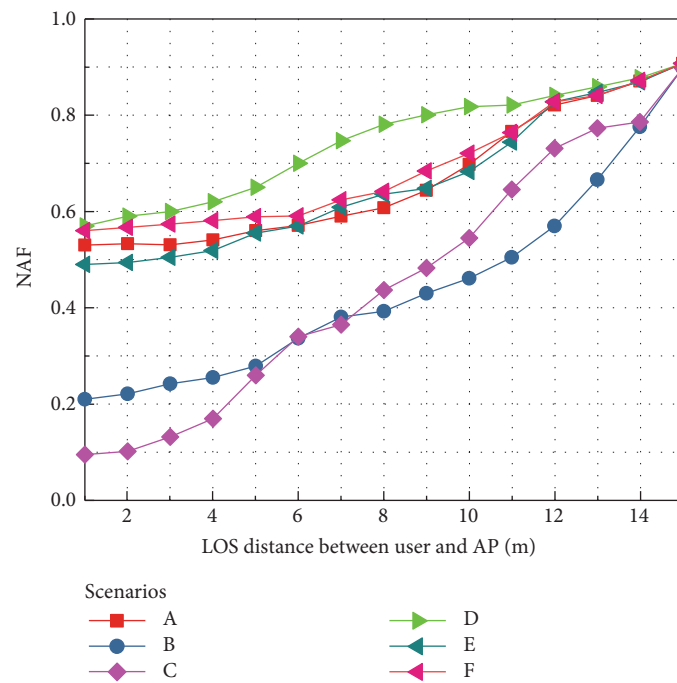


FIGURE 11: NAF variation using OCC with increasing distance between user and LED AP.

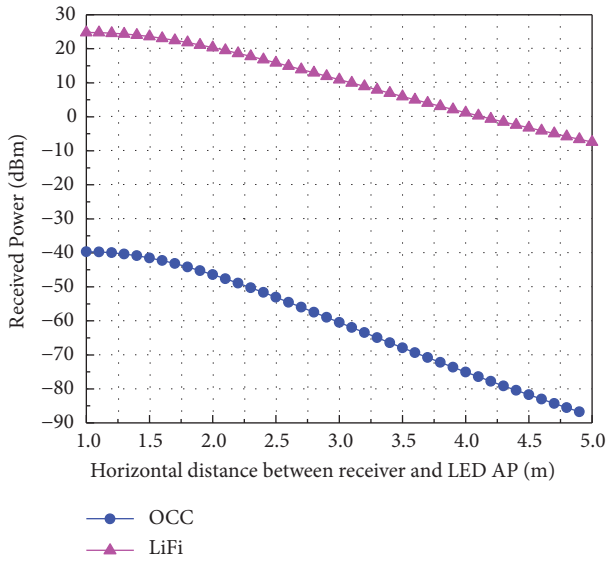


FIGURE 12: Distribution of received power for LiFi and OCC.

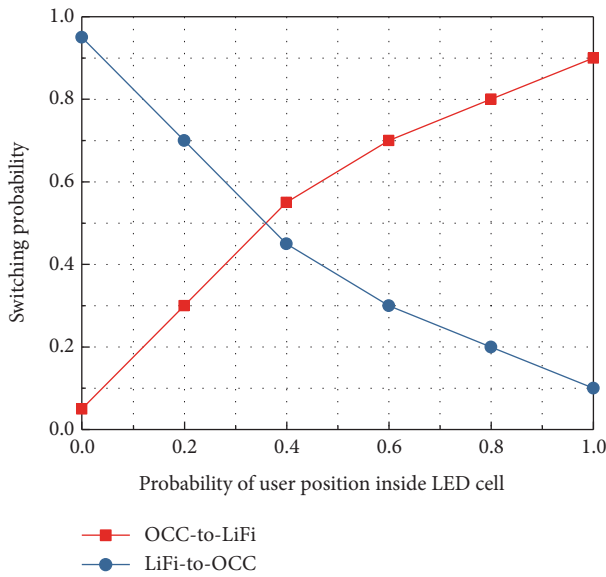


FIGURE 13: Link-switching probability analysis.

Disclosure

This article is an extended version of a paper presented in the International Conference on Ubiquitous and Future Networks (ICUFN 2018), Prague, Czech Republic, July 2018.

Conflicts of Interest

The authors do not have any conflicts of interest.

Acknowledgments

This work was supported by Institute for Information & Communications Technology Promotion (IITP) grant funded by

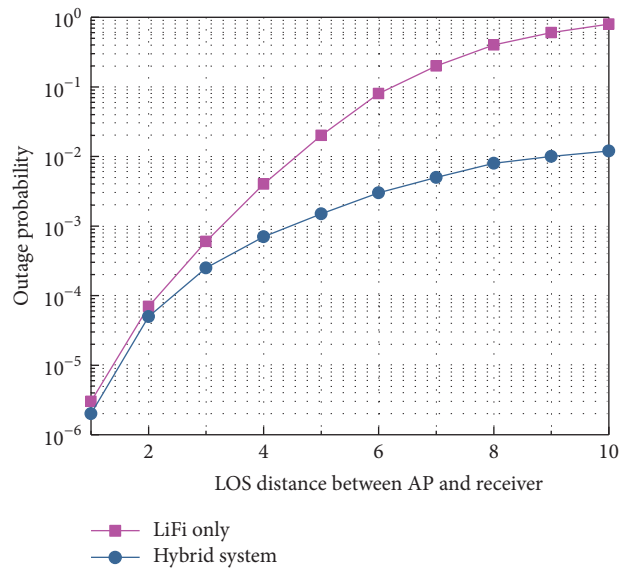


FIGURE 14: Comparison of outage probability.

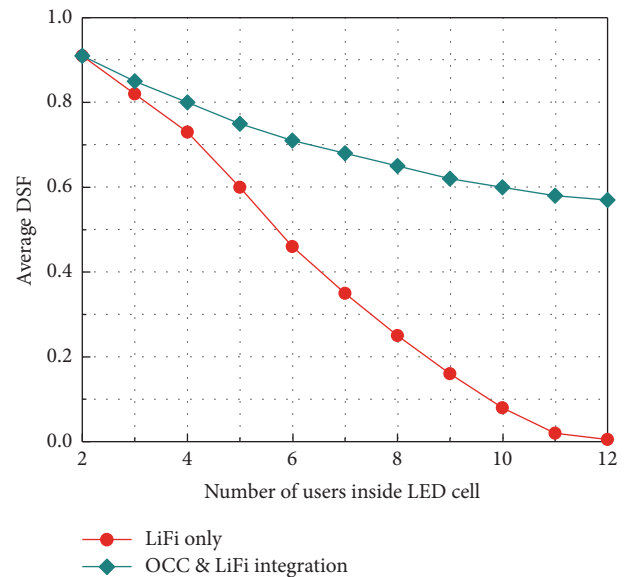


FIGURE 15: Average DSF comparison for multiple users served by the same LED AP.

the Korea Government (MSIT) (no. 2017-0-00824, Development of Intelligent and Hybrid OCC-LiFi Systems for Next Generation Optical Wireless Communications).

References

- [1] Z. Ghassemlooy, S. Arnon, M. Uysal, Z. Xu, and J. Cheng, "Emerging Optical Wireless Communications-Advances and Challenges," *IEEE Journal on Selected Areas in Communications*, vol. 33, no. 9, pp. 1738–1749, 2015.
- [2] P. H. Pathak, X. Feng, P. Hu, and P. Mohapatra, "Visible Light Communication, Networking, and Sensing: A Survey, Potential and Challenges," *IEEE Communications Surveys & Tutorials*, vol. 17, no. 4, pp. 2047–2077, 2015.

- [3] M. Z. Chowdhury, M. T. Hossan, A. Islam, and Y. M. Jang, "A Comparative Survey of Optical Wireless Technologies: Architectures and Applications," *IEEE Access*, vol. 6, pp. 9819–9840, 2018.
- [4] H. Chen, H. P. A. Van Den Boom, E. Tangdiongga, and T. Koonen, "30-Gb/s bidirectional transparent optical transmission with an MMF access and an indoor optical wireless link," *IEEE Photonics Technology Letters*, vol. 24, no. 7, pp. 572–574, 2012.
- [5] D. K. Borah, A. C. Boucouvalas, C. C. Davis, S. Hranilovic, and K. Yiannopoulos, "A review of communication-oriented optical wireless systems," *EURASIP Journal on Wireless Communications and Networking*, vol. 91, pp. 1–28, 2012.
- [6] H. Elgala, R. Mesleh, and H. Haas, "Indoor optical wireless communication: Potential and state-of-the-art," *IEEE Communications Magazine*, vol. 49, no. 9, pp. 56–62, 2011.
- [7] D. Karunatilaka, F. Zafar, V. Kalavally, and R. Parthiban, "LED based indoor visible light communications: state of the art," *IEEE Communications Surveys & Tutorials*, vol. 17, no. 3, pp. 1649–1678, 2015.
- [8] R. Zhang, J. Wang, Z. Wang, Z. Xu, C. Zhao, and L. Hanzo, "Visible light communications in heterogeneous networks: Paving the way for user-centric design," *IEEE Wireless Communications Magazine*, vol. 22, no. 2, pp. 8–16, 2015.
- [9] A. C. Boucouvalas, P. Chatzimisios, Z. Ghassemlooy, M. Uysal, and K. Yiannopoulos, "Standards for indoor Optical Wireless Communications," *IEEE Communications Magazine*, vol. 53, no. 3, pp. 24–31, 2015.
- [10] M. Leba, S. Riurean, and A. Lonica, "LiFi - The path to a new way of communication," in *Proceedings of the 12th Iberian Conference on Information Systems and Technologies, CISTI 2017*, Portugal, June 2017.
- [11] Y. Perwej, "The Next Generation of Wireless Communication Using Li-Fi (Light Fidelity) Technology," *Computer Networks*, vol. 4, no. 1, pp. 20–29, 2017.
- [12] Y. Wang, X. Wu, and H. Haas, "Load Balancing Game with Shadowing Effect for Indoor Hybrid LiFi/RF Networks," *IEEE Transactions on Wireless Communications*, vol. 16, no. 4, pp. 2366–2378, 2017.
- [13] M. Kashef, M. Ismail, M. Abdallah, K. A. Qaraq, and E. Serpedin, "Energy efficient resource allocation for mixed RF/VLC heterogeneous wireless networks," *IEEE Journal on Selected Areas in Communications*, vol. 34, no. 4, pp. 883–893, 2016.
- [14] F. Jin, R. Zhang, and L. Hanzo, "Resource allocation under delay-guarantee constraints for heterogeneous visible-light and RF femtocell," *IEEE Transactions on Wireless Communications*, vol. 14, no. 2, pp. 1020–1034, 2015.
- [15] Y. Wang, D. A. Basnayaka, X. Wu, and H. Haas, "Optimization of Load Balancing in Hybrid LiFi/RF Networks," *IEEE Transactions on Communications*, vol. 65, no. 4, pp. 1708–1720, 2017.
- [16] Y. Wang and H. Haas, "Dynamic Load Balancing with Handover in Hybrid Li-Fi and Wi-Fi Networks," *Journal of Lightwave Technology*, vol. 33, no. 22, pp. 4671–4682, 2015.
- [17] M. Ayyash, H. Elgala, A. Khreishah et al., "Coexistence of WiFi and LiFi toward 5G: concepts, opportunities, and challenges," *IEEE Communications Magazine*, vol. 54, no. 2, pp. 64–71, 2016.
- [18] G. Pan, J. Ye, and Z. Ding, "Secure Hybrid VLC-RF Systems with Light Energy Harvesting," *IEEE Transactions on Communications*, vol. 65, no. 10, pp. 4348–4359, 2017.
- [19] S. Shao and A. Khreishah, "Delay Analysis of Unsaturated Heterogeneous Omnidirectional-Directional Small Cell Wireless Networks: The Case of RF-VLC Coexistence," *IEEE Transactions on Wireless Communications*, vol. 15, no. 12, pp. 8406–8421, 2016.
- [20] H.-S. Kim, D.-H. Kwon, S.-H. Yang, Y.-H. Son, and S.-K. Han, "Channel assignment technique for RF frequency reuse in CA-VLC-based accurate optical indoor localization," *Journal of Lightwave Technology*, vol. 32, no. 14, pp. 2544–2555, 2014.
- [21] P. Luo, Z. Ghassemlooy, H. Le Minh, X. Tang, and H.-M. Tsai, "Undersampled phase shift ON-OFF keying for camera communication," in *Proceedings of the 6th International Conference on Wireless Communications and Signal Processing (WCSP '14)*, pp. 1–6, IEEE, Hefei, China, October 2014.
- [22] T. Yamazato, I. Takai, H. Okada et al., "Image-sensor-based visible light communication for automotive applications," *IEEE Communications Magazine*, vol. 52, no. 7, pp. 88–97, 2014.
- [23] T. Nguyen, A. Islam, T. Hossan, and Y. M. Jang, "Current status and performance analysis of optical camera communication technologies for 5G networks," *IEEE Access*, vol. 5, pp. 4574–4594, 2017.
- [24] Y. Goto, I. Takai, T. Yamazato et al., "A New Automotive VLC System Using Optical Communication Image Sensor," *IEEE Photonics Journal*, vol. 8, no. 3, pp. 1–17, 2016.
- [25] R. D. Roberts, "Undersampled frequency shift ON-OFF keying (UFSOOK) for camera communications (CamCom)," in *Proceedings of the 22nd Wireless and Optical Communications Conference, WOCC '13*, pp. 645–648, China, May 2013.
- [26] I. Takai, S. Ito, K. Yasutomi, K. Kagawa, M. Andoh, and S. Kawahito, "LED and CMOS image sensor based optical wireless communication system for automotive applications," *IEEE Photonics Journal*, vol. 5, no. 5, 2013.
- [27] M. T. Hossan, M. Z. Chowdhury, A. Islam, and Y. M. Jang, "A Novel Indoor Mobile Localization System Based on Optical Camera Communication," *Wireless Communications and Mobile Computing*, vol. 2018, 17 pages, 2018.
- [28] B. Lin, Z. Ghassemlooy, C. Lin, X. Tang, Y. Li, and S. Zhang, "An Indoor Visible Light Positioning System Based on Optical Camera Communications," *IEEE Photonics Technology Letters*, vol. 29, no. 7, pp. 579–582, 2017.
- [29] T. Nguyen, A. Islam, T. Yamazato, and Y. M. Jang, "Technical Issues on IEEE 802.15.7m Image Sensor Communication Standardization," *IEEE Communications Magazine*, vol. 56, no. 2, pp. 213–218, 2018.
- [30] I. Takai, T. Harada, M. Andoh, K. Yasutomi, K. Kagawa, and S. Kawahito, "Optical vehicle-to-vehicle communication system using LED transmitter and camera receiver," *IEEE Photonics Journal*, vol. 6, no. 5, pp. 1–14, 2014.
- [31] T. Yamazato, M. Kinoshita, S. Arai et al., "Vehicle Motion and Pixel Illumination Modeling for Image Sensor Based Visible Light Communication," *IEEE Journal on Selected Areas in Communications*, vol. 33, no. 9, pp. 1793–1805, 2015.
- [32] P. Ji, H.-M. Tsai, C. Wang, and F.-Q. Liu, "Vehicular visible light communications with led taillight and rolling shutter camera," in *Proceedings of the IEEE 79th Vehicular Technology Conference (VTC '14)*, pp. 1–6, Seoul, Republic of Korea, May 2014.
- [33] T. J. Ross, *Fuzzy Logic with Engineering Applications*, John Wiley & Sons, Ltd, 3rd edition, 2011.
- [34] M. Kawser, "Performance Comparison between Round Robin and Proportional Fair Scheduling Methods for LTE," *International Journal of Information and Electronics Engineering*, vol. 2, no. 5, pp. 678–681, 2012.
- [35] P. Luo, M. Zhang, Z. Ghassemlooy, S. Zvanovec, S. Feng, and P. Zhang, "Undersampled-Based Modulation Schemes for Optical Camera Communications," *IEEE Communications Magazine*, vol. 56, no. 2, pp. 204–212, 2018.

- [36] R. D. Roberts, "A MIMO protocol for camera communications (CamCom) using undersampled frequency shift ON-OFF keying (UFSOOK)," in *Proceedings of the IEEE Globecom Workshops (GC Wkshps '13)*, pp. 1052–1057, Atlanta, GA, December 2013.
- [37] P. Luo et al., "Experimental demonstration of RGB LED-based optical camera communications," *IEEE Photonics Journal*, vol. 7, no. 5, pp. 1–12, 2015.
- [38] J. M. Kahn and J. R. Barry, "Wireless infrared communications," *Proceedings of the IEEE*, vol. 85, no. 2, pp. 265–298, 1997.
- [39] V. Jungnickel, V. Pohl, S. Nönnig, and C. Von Helmolt, "A physical model of the wireless infrared communication channel," *IEEE Journal on Selected Areas in Communications*, vol. 20, no. 3, pp. 631–640, 2002.
- [40] X. Wu, M. Safari, and H. Haas, "Access Point Selection for Hybrid Li-Fi and Wi-Fi Networks," *IEEE Transactions on Communications*, vol. 65, no. 12, pp. 5375–5385, 2017.
- [41] M. Kaya and R. Alhajj, "Utilizing genetic algorithms to optimize membership functions for fuzzy weighted association rules mining," *Applied Intelligence*, vol. 24, no. 1, pp. 7–15, 2006.
- [42] T. Bouali and S. Senouci, "A fuzzy logic-based communication medium selection for QoS preservation in vehicular networks," in *Proceedings of the IEEE International Conference on Communications (ICC '16)*, pp. 1–6, Kuala Lumpur, Malaysia, May 2016.
- [43] A. I. Aziz, S. Rizvi, and N. M. Saad, "Fuzzy logic based vertical handover algorithm between LTE and WLAN," in *Proceedings of the International Conference on Intelligent and Advanced Systems (ICIAS '10)*, pp. 1–4, IEEE, Kuala Lumpur, Malaysia, June 2010.

Research Article

Exploiting Opportunistic Scheduling for Physical-Layer Security in Multitwo User NOMA Networks

Kyusung Shim ¹ and Beongku An ²

¹Department of Electronics and Computer Engineering in Graduate School, Hongik University, 30016, Republic of Korea

²Department of Software and Communications Engineering, Hongik University, 30016, Republic of Korea

Correspondence should be addressed to Beongku An; beongku@hongik.ac.kr

Received 1 August 2018; Revised 17 September 2018; Accepted 2 October 2018; Published 23 October 2018

Guest Editor: Mostafa Zaman Chowdhury

Copyright © 2018 Kyusung Shim and Beongku An. This is an open access article distributed under the Creative Commons Attribution License, which permits unrestricted use, distribution, and reproduction in any medium, provided the original work is properly cited.

In this paper, we address the opportunistic scheduling in multitwo user NOMA system consisting of one base station, multilinear user, multifar user, and one eavesdropper. To improve the secrecy performance, we propose the users selection scheme, called best-secure-near-user best-secure-far-user (BSNBSF) scheme. The BSNBSF scheme aims to select the best near-far user pair, whose data transmission is the most robust against the overhearing of an eavesdropper. In order to facilitate the performance analysis of the BSNBSF scheme in terms of secrecy outage performance, we derive the exact closed-form expression for secrecy outage probability (SOP) of the selected near user and the tight approximated closed-form expression for SOP of the selected far user, respectively. Additionally, we propose the descent-based search method to find the optimal values of the power allocation coefficients that can minimize the total secrecy outage probability (TSOP). The developed analyses are corroborated through Monte Carlo simulation. Comparisons with the random-near-user random-far-user (RNRF) scheme are performed and show that the proposed scheme significantly improves the secrecy performance.

1. Introduction

To support the 5G-and-beyond-5G communication networks, called future communication networks, nonorthogonal multiple access (NOMA) has been considered as a solution to increase the spectral efficiency by superposing multiple users in resource domain (e.g., time and frequency) [1–3]. More specifically, the downlink scenario of the multitwo user NOMA networks consisting of one base station, a near user (that has strong channel state information (CSI)), and a far user (that has low CSI) is actively considered. The base station simultaneously transmits message to both users using the superposition coding; then the transmit power of the far user message is allocated more than that of the near user message. Under the NOMA scenario, the near user first subtracts the far user message using the successive interference cancellation (SIC) technique [4]; after that the near user decodes its own message. Different from the near user, the far user directly decodes its own message from the received signal without the interference elimination process

since the far user message has allocated higher transmit power than that of the near user message.

The NOMA system can allocate the multiple information on the transmit signal using the superposition coding. Thus, the NOMA system has an advantage in terms of spectrum efficiency compared to that of the OMA system [5–7]. However, this point is a disadvantage in terms of the security [8, 9]. For example, if the eavesdropper succeeds in the interception of one NOMA signal, then the eavesdropper can obtain multiple user information [10]. Thus, the security issue is more important in the NOMA system. Physical layer security (PLS) is one of the possible solutions against the attack of the malicious user. More specifically, from the information-theoretical aspect, the message can be confidentially transmitted if the main channel (between legitimate users) and the eavesdropper channel (between a legitimate user and an eavesdropper) can be controlled so that the legitimate user can decode the received message successfully while the eavesdropper is not able to decode their intercepted message [11]. It is shown that PLS is on the cutting edge of the

technique of security in wireless communication to prevent eavesdropping attacks [12–14].

In PLS, the secrecy outage probability is defined as the probability that the achievable system secrecy capacity of the near/far user drops below a predefined target secrecy rate as in [15]. From the secrecy outage probability, we can measure the degree of security on the system. For example, the low secrecy outage probability system means that the system is more robust compared to that of the high secrecy outage probability system in the viewpoints of security. To improve the PLS performance, the CSI-based opportunistic scheduling [16], that is, the source (destination), communicates with one scheduled destination (source) in a certain resource block (e.g., time and frequency). It has been recognized as an attractive scheduling scheme [17–19] since the time-varying nature of wireless channels is exploited. Thus, opportunistic scheduling is expected as one of techniques to enhance the secrecy performance on NOMA system.

Indeed, the authors of [20] studied the security performance of single-input-single-output (SISO) NOMA system. The authors confirmed that the secrecy sum rate of SISO NOMA system has better performance than that of the OMA system. Liu *et al.* [21] compared the multiple-input-multiple-output (MIMO) NOMA system and MIMO OMA system. Additionally, the authors proved that MIMO NOMA system is better than MIMO OMA system in terms of sum channel capacity. In [22], the authors proposed the transmit antenna selection (TAS) scheme to improve the secrecy performance for downlink multiple-input-single-output (MISO) NOMA system. The first proposed antenna selection scheme is the optimal antenna selection scheme for near user and far user, respectively, while the second proposed antenna selection scheme is the suboptimal antenna selection scheme for the main channel performance of the near user and far user, respectively. The authors of [23] addressed the PLS of large-scale NOMA system. This network consisted of the multiple-antenna base station; the legitimate users were uniformly distributed within a disc, and the eavesdroppers were distributed in an infinite two-dimensional plane via a homogeneous Poisson point process (PPP). The authors derived new exact and asymptotic analyses for the secrecy outage probability (SOP). Li *et al.* [24] optimized the secure beamforming and power allocation design on the MISO NOMA system. From the numerical results, the authors demonstrated that their proposed scheme outperformed that of the conventional OMA system. The authors of [25] designed a secure NOMA system under secrecy constraints where a transmitter sends a signal to multiusers in the presence of an eavesdropper. The authors minimized the total transmit power subject to the QoS and secrecy constraints. The authors of [26] exploited the artificial-noise-aided secure transmission for NOMA full-duplex relay network. The authors proposed the novel joint NOMA and artificial-noise-aided full-duplex relay (NOMA-ANFDR) scheme to enhance the physical security. Specifically, this paper derived the SOP and secrecy throughput. The NOMA-ANFDR outperformed the joint NOMA and artificial-noise half-duplex relay (NOMA-ANHDR) scheme.

Very recently, in [8], the authors proposed the cooperative NOMA system to enhance PLS performance. The authors

considered the NOMA system including a base station, two users (near user and far user), a relay, and an eavesdropper. The authors derived the closed-form and asymptotic analysis for security outage probability and strictly positive secrecy capacity, respectively. The authors of [27] designed a secure massive NOMA system with multiclouds. The authors studied the interuser interference in the designed NOMA system and proposed the power control and power allocation algorithm for maximizing the secrecy capacity. In [28], the authors studied the security impact in the multiuser visible light communication (VLC) [29] with NOMA system. The authors considered both single eavesdropper and multiple eavesdroppers scenarios when the one transmitter communicates with multiple users. The authors derived the exact secrecy outage probability in this network. The author in [30] proposed the relay-supported cooperative NOMA system. The proposed system helped to transmit data using the multiple antenna equipped with relay. In a certain time block, this system selected the transmitted antenna in the relay based on the legitimate channel state information. The authors derived the exact closed-form expression in the proposed system. Lei *et al.* [31] proposed the NOMA system consisting of multiple-antenna base station, multidestinations equipped with multiple antennas, and multieavesdroppers equipped with multiple antennas. Then, the authors proposed and analyzed the max-min based transmit antenna selection scheme when the eavesdroppers work independently or collude.

In the related works, the authors proposed the several schemes to improve the PLS performance. However, the opportunistic scheduling in the multitwo user NOMA network was not considered in the literature. Thus, in this paper, we propose a new users selection scheme to improve the PLS performance in downlink multitwo user NOMA system using the opportunistic scheduling in the presence of one eavesdropper. Compared with the aforementioned works, the main contribution and feature of this paper can be summarized as follows.

- (i) In this paper, we propose a new near/far user selection scheme on the multiple-two user NOMA system. The proposed scheme, denoted by best-secure-near-user best-secure-far-user (BSNBSF) scheme, aims to select the best near-far user pairs, whose data transmission is the most robust combat against the eavesdropper's attack. More specifically, in a certain resource block, we take into account the main/eavesdropper channel state information to select the received user pairs.
- (ii) We derive novel expressions for the selected user pairs, respectively, to estimate the secrecy performance achieved by the proposed scheme. The analyses are not reported in the literature. More specifically, for the selected near user case, we derive an exact closed-form expression on the SOP, whereas, for the selected far user case, we obtain a tight approximated closed-form expression on the SOP, respectively.
- (iii) We present other results, called the asymptotic SOP, for the proposed scheme. These expressions provide the insight into the behavior of the average far user channel power gain (λ_{SF}).

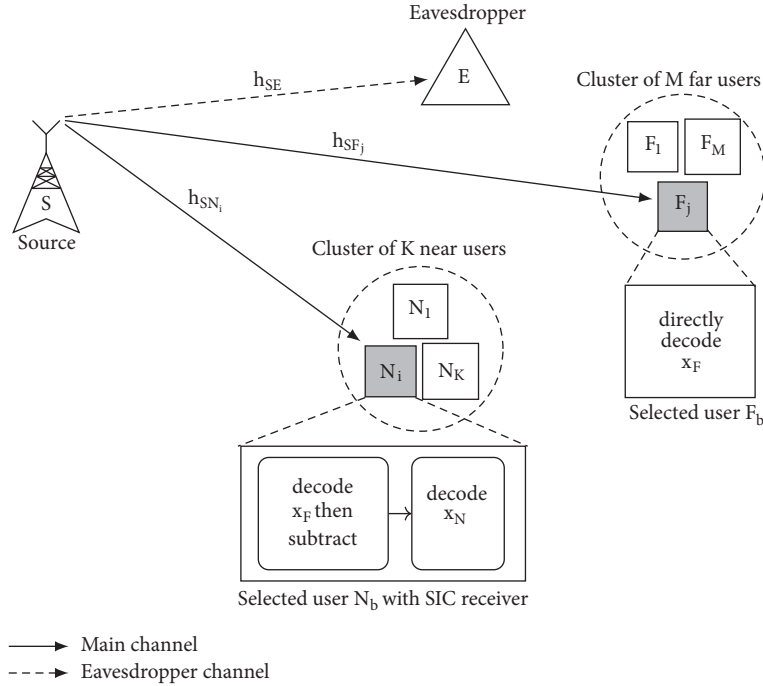


FIGURE 1: Schematic illustration of the multiuser NOMA system with the presence of an eavesdropper.

- (iv) We conduct the optimal analysis of the power allocation coefficient (θ_N). More specifically, the proposed optimal analysis finds the optimal power allocation coefficient value to make the total SOP minimum on the proposed system based on the descent method.
- (v) Through the numerical results, we demonstrate that the BSNBSF scheme significantly enhances the secrecy performance on the multiuser NOMA system compared to that of the benchmarked scheme. More specifically, in the case of the SOP for the selected near user, the floor occurs and the selected far user shows the convex pattern as a function of the transmit SNR. Additionally, the secrecy sum throughput of the BSNBSF scheme shows better performance than that of the RNRF scheme.

The rest of this paper is organized as follows. In Section 2, the proposed system model and user pair selection scheme are described. Section 3 investigates the closed-form and asymptotic analyses of the multiuser NOMA systems. Section 4 presents the optimal analysis of the power allocation coefficients. Section 5 presents some illustrative numerical results based on the insightful discussion. Monte Carlo simulations are shown to corroborate the proposed analyses. Finally, Section 6 concludes the paper.

Notations: $X \sim \mathcal{CN}(0, \sigma^2)$ denotes a circularly symmetric complex Gaussian random variable X with zero mean and variance σ^2 ; $\Pr(\cdot)$ is the probability; $f_X(\cdot)$ and $F_X(\cdot)$ represent the probability density function (PDF) and cumulative distribution function (CDF) of the random variable X , respectively.

2. System Model

Let us consider a downlink multiuser NOMA system including a base station (S), a set of K near users, $\mathcal{N} = \{N_i \mid i = 1, 2, \dots, K\}$, and a set of M far users, $\mathcal{F} = \{F_j \mid j = 1, 2, \dots, M\}$, and an eavesdropper (E), as shown in Figure 1. More specifically, the near users can perfectly use the SIC technique to subtract the far x_F [22]. Both the legitimate and the illegitimate receivers are equipped with a single antenna and operate in half-duplex mode. In this paper, h_{XY} and $|h_{XY}|^2$, where $X \in \{S\}$, $Y \in \mathcal{N} \cup \mathcal{F} \cup \{E\}$, present the channel coefficient and the corresponding channel gain of $X \rightarrow Y$, respectively. Assuming that all wireless channels exhibit Rayleigh block fading channel, h_{XY} can be modeled as independent and identically distributed (i.i.d.) complex Gaussian random variable with zero mean and variance λ_{XY} . Thus, the corresponding channel gain, $|h_{XY}|^2$, is an exponential random variable with probability density function (PDF), $f_{|h_{XY}|^2}(z) = (1/\lambda_{XY})\exp(-z/\lambda_{XY})$, if $z \geq 0$; otherwise, $f_{|h_{XY}|^2}(z) = 0$ as in [32–34]. More specifically, the average channel gain can be written as $\lambda_{XY} = (d_{XY}/d_0)^{-\epsilon} \mathcal{L}$, where \mathcal{L} is the reference signal power attenuation, d_{XY} denotes the distance between X and Y , d_0 presents the reference distance, and ϵ is the path-loss exponent [33]. And the channel noise is followed by $\omega_Y \sim \mathcal{CN}(0, \sigma_Y^2)$. We also assume that the source perfectly knows the channel state information (CSI) of all legitimate users and eavesdropper, as in [11, 35].

2.1. Communication Process. In this subsection, we present in detail the communication process in two-user NOMA system. Assuming that N_i and F_j are selected to receive its data from the S in a certain time slot. From the principle of NOMA, the messages x_N and x_F that will be allocated to θ_N

and θ_F , respectively, are superposed as $\sqrt{\theta_N}x_N + \sqrt{\theta_F}x_F$ and then broadcasted by S, where θ_N and θ_F denote the power allocation coefficients. We suppose that $|h_{SN_i}|^2 > |h_{SF_j}|^2$, and set $0 < \theta_N < \theta_F$ and $\theta_N + \theta_F = 1$ as in [21].

At the near user N_i , the received signal is given by

$$y_{SN_i} = \sqrt{P_S \theta_N} h_{SN_i} x_N + \sqrt{P_S \theta_F} h_{SN_i} x_F + \omega_{N_i}, \quad (1)$$

where P_S denotes the transmit power of the S. Because of the power allocation coefficient condition, the near user needs to subtract the component, x_F , from the y_{SN_i} using the SIC process [36]. The signal-to-interference-plus-noise-ratio (SINR) of the eliminated component, x_F , is expressed as

$$\gamma_{SN_i}^{x_F} = \frac{P_S \theta_F |h_{SN_i}|^2}{P_S \theta_N |h_{SN_i}|^2 + \sigma_{SN_i}^2}. \quad (2)$$

After the SIC process, the N_i archives its own message, x_N , from the received signal in which signal-to-noise-ratio (SNR) is obtained as

$$\gamma_{SN_i}^{x_N} = \frac{P_S \theta_N |h_{SN_i}|^2}{\sigma_{SN_i}^2}. \quad (3)$$

At the far user F_j , the received signal is given by

$$y_{SF_j} = \sqrt{P_S \theta_F} h_{SF_j} x_F + \sqrt{P_S \theta_N} h_{SF_j} x_N + \omega_{F_j}. \quad (4)$$

Different from the near user, the F_j directly decodes the SINR from the received signal because of the power allocation coefficient condition. The received SINR at F_j to decode x_F is given by

$$\gamma_{SF_j}^{x_F} = \frac{P_S \theta_F |h_{SF_j}|^2}{P_S \theta_N |h_{SF_j}|^2 + \sigma_{SF_j}^2}. \quad (5)$$

Meanwhile, the eavesdropper can intercept the signal due to the broadcast nature of wireless medium. Thus, the received signal at E can be written as

$$y_{SE} = \sqrt{P_S \theta_N} h_{SE} x_N + \sqrt{P_S \theta_F} h_{SE} x_F + \omega_E. \quad (6)$$

Different from the legitimate user, we assume that the E has enough ability to distinguish each message from the received signal. Thus, the SINRs of the received signal are given by

$$\gamma_{SE}^{x_F} = \frac{P_S \theta_F |h_{SE}|^2}{P_S \theta_N |h_{SE}|^2 + \sigma_{SE}^2}, \quad (7)$$

and

$$\gamma_{SE}^{x_N} = \frac{P_S \theta_N |h_{SE}|^2}{\sigma_{SE}^2}, \quad (8)$$

respectively.

In physical-layer security, the secrecy capacity means the difference between main channel capacity and eavesdropper channel capacity. Thus, in two-user NOMA system, the secrecy capacities of x_N and x_F are given by [22, 37]

$$C_{s,N_i} = \left[\log_2 \left(1 + \gamma_{SN_i}^{x_N} \right) - \log_2 \left(1 + \gamma_{SE}^{x_N} \right) \right]^+, \quad (9)$$

$$C_{s,F_j} = \left[\log_2 \left(1 + \gamma_{SF_j}^{x_F} \right) - \log_2 \left(1 + \gamma_{SE}^{x_F} \right) \right]^+, \quad (10)$$

respectively, where $[x]^+ = \max\{x, 0\}$.

2.2. The Proposed Best-Secure-Near-User Best-Secure-Far-User (BSNBSF) Scheme. The proposed user selection process is conducted through the channel state information (CSI) estimation/calculation system. Thus, this process is carried out before the data communication process as in [11, 35]. In this paper, we propose the BSNBSF user selection scheme to maximize the secrecy capacity at N_i and F_j , respectively. The proposed scheme can be mathematically expressed as

$$N_b = \arg \max_{i \in \mathcal{N}} \left\{ \log_2 \left(\frac{1 + \gamma_{SN_i}^{x_N}}{1 + \gamma_{SE}^{x_N}} \right) \right\}, \quad (11)$$

and

$$F_b = \arg \max_{j \in \mathcal{F}} \left\{ \log_2 \left(\frac{1 + \gamma_{SF_j}^{x_F}}{1 + \gamma_{SE}^{x_F}} \right) \right\}. \quad (12)$$

(11) and (12) mean that the selected users are the best secrecy capacity of a certain time slot.

3. Secrecy Outage Performance Analysis

In this section, the performance investigation of the proposed user selection scheme in terms of secrecy outage probability (SOP) is presented. Because the wireless channels undergo i.i.d. Rayleigh fading, for the sake of notational convenience, we assume that $\lambda_{SN_i} = \lambda_{SN_2} = \dots = \lambda_{SN_i} = \lambda_{SN}$, $\lambda_{SF_1} = \lambda_{SF_2} = \dots = \lambda_{SF_j} = \lambda_{SF}$.

We also assume the all nodes have the same noise variance. Let $\gamma = P_S/\sigma^2$ present the transmit SNR as in [11, 22]. The SOP of a user can be defined as the probability that the instantaneous secrecy capacity of the user falls below a predefined target data rate [23]. Thus, the SOPs at N_b and F_b are obtained as

$$P_{SOP,N_b} = \Pr \left(C_{s,N_b} < R_{th,N_b} \right), \quad (13)$$

and

$$P_{SOP,F_b} = \Pr \left(C_{s,F_b} < R_{th,F_b} \right), \quad (14)$$

where R_{th,N_b} and R_{th,F_b} denote the target data rate at N_b and F_b , respectively.

3.1. The Exact Secrecy Outage Probability. At the selected near user, the SOP of N_b can be expressed as

$$P_{SOP,N_b} = \Pr \left(\log_2 \left(\frac{1 + \gamma \theta_N |h_{SN_b}|^2}{1 + \gamma \theta_N |h_{SE}|^2} \right) < R_{th,N_b} \right). \quad (15)$$

Because all wireless channels are assumed to be independent, (15) can be rewritten as

$$P_{\text{SOP},N_b} = \Pr \left(\max_{i \in \mathcal{N}} \left\{ \frac{1 + \gamma\theta_N |h_{\text{SN}_i}|^2}{1 + \gamma\theta_N |h_{\text{SE}}|^2} \right\} < \gamma_{\text{th},N_b} \right), \quad (16)$$

where $\gamma_{\text{th},N_b} \triangleq 2^{R_{\text{th},N_b}}$. As we can observe that the events of the probability in (16) are not mutually exclusive because they include the same components $|h_{\text{SE}}|^2$, therefore conditioning on $|h_{\text{SE}}|^2 = z$, the P_{SOP,N_b} can be further expressed as

$$P_{\text{SOP},N_b} = \int_0^\infty \Pr \left(\bigcap_{i=1}^K \left(\frac{1 + \gamma\theta_N |h_{\text{SN}_i}|^2}{1 + \gamma\theta_N z} < \gamma_{\text{th},N_b} \right) \right) \cdot f_Z(z) dz. \quad (17)$$

Since the assumption that all wireless channels are identical, (17) can be further expressed as

$$P_{\text{SOP},N_b} = \int_0^\infty \prod_{i=1}^K \Pr \left(|h_{\text{SN}_i}|^2 < \frac{\gamma_{\text{th},N_b} - 1}{\gamma\theta_N} + \gamma_{\text{th},N_b} z \right) \cdot f_Z(z) dz. \quad (18)$$

For the sake of notational convenience, let $X_i \triangleq |h_{\text{SN}_i}|^2$; Ψ in (18) can be rewritten as

$$\Psi = \int_0^{(\gamma_{\text{th},N_b} - 1)/\gamma\theta_N + \gamma_{\text{th},N_b} z} f_{X_i}(x) dx. \quad (19)$$

After some algebra manipulations, Ψ can be obtained as

$$\Psi = 1 - \exp \left(-\frac{1}{\lambda_{\text{SN}}} \left(\frac{\gamma_{\text{th},N_b} - 1}{\gamma\theta_N} + \gamma_{\text{th},N_b} z \right) \right). \quad (20)$$

Plugging (20) into (18) and making use of the binomial theorem [38, Eq. (1.111)]

$$(a + b)^N = \sum_{k=0}^N \binom{N}{k} a^{N-k} b^k, \quad (21)$$

P_{SOP,N_b} in (18) can be further expressed as

$$P_{\text{SOP},N_b} = \sum_{n=0}^K \binom{K}{n} (-1)^n \frac{1}{\lambda_{\text{SE}}} \exp \left(-\frac{n(\gamma_{\text{th},N_b} - 1)}{\lambda_{\text{SN}} \gamma \theta_N} \right) \cdot \int_0^\infty \exp \left(-\left(\frac{n\gamma_{\text{th},N_b}}{\lambda_{\text{SN}}} + \frac{1}{\lambda_{\text{SE}}} \right) z \right) dz. \quad (22)$$

After some algebra manipulations and making use of the fact that $\int_0^\infty \exp(-1/a)x dx = a$ [38, Eq. (3.310)], consequently, the exact closed-form expression for SOP of the selected near user can be obtained as

$$P_{\text{SOP},N_b} = \sum_{n=0}^K \binom{K}{n} (-1)^n \frac{\lambda_{\text{SN}}}{n\gamma_{\text{th},N_b} \lambda_{\text{SE}} + \lambda_{\text{SN}}} \cdot \exp \left(-\frac{n(\gamma_{\text{th},N_b} - 1)}{\lambda_{\text{SN}} \gamma \theta_N} \right). \quad (23)$$

At the selected far user, the SOP of F_b can be expressed as

$$P_{\text{SOP},F_b} = \Pr \left(\log_2 \left(\frac{1 + \gamma\theta_F |h_{\text{SF}_b}|^2 / (\gamma\theta_N |h_{\text{SF}_b}|^2 + 1)}{1 + \gamma\theta_F |h_{\text{SE}}|^2 / (\gamma\theta_N |h_{\text{SE}}|^2 + 1)} \right) < R_{\text{th},F_b} \right). \quad (24)$$

Similar to the case of the selected near user, all wireless channels are independent and identical. And the events of the probability in (24) are not mutually exclusive because they include the same components $\gamma\theta_F |h_{\text{SE}}|^2 / (\gamma\theta_N |h_{\text{SE}}|^2 + 1)$. Therefore, conditioning on $\gamma\theta_F |h_{\text{SE}}|^2 / (\gamma\theta_N |h_{\text{SE}}|^2 + 1) = t$, (24) can be further expressed as

$$P_{\text{SOP},F_b} = \int_0^\infty \prod_{j=1}^M \Pr \left(\underbrace{\frac{\gamma\theta_F |h_{\text{SF}_j}|^2}{\gamma\theta_N |h_{\text{SF}_j}|^2 + 1}}_{\phi} < \gamma_{\text{th},F_b} - 1 + \gamma_{\text{th},F_b} t \right) \cdot f_T(t) dt. \quad (25)$$

In order to further simplify the integral (25), the following lemma enables us to characterize the SINR at far user and eavesdropper to decode x_F .

Lemma 1. Suppose that $U \triangleq \gamma\theta_F \rho / (\gamma\theta_N \rho + 1)$ ($\rho \in \{|h_{\text{SF}_j}|^2, |h_{\text{SE}}|^2\}$); the cumulative distribution function (CDF) and probability density function (PDF) can be expressed as

$$F_U(u) = \begin{cases} 1 - \varphi(\lambda_U, u), & \text{if } 0 \leq u < \frac{\theta_F}{\theta_N}, \\ 1, & \text{if } \frac{\theta_F}{\theta_N} \leq u, \end{cases} \quad (26)$$

and

$$f_U(u) = \begin{cases} \frac{\theta_F}{\lambda_U \gamma (\theta_F - \theta_N u)^2} \varphi(\lambda_U, u), & \text{if } 0 \leq u < \frac{\theta_F}{\theta_N}, \\ 0, & \text{if } \frac{\theta_F}{\theta_N} \leq u, \end{cases} \quad (27)$$

respectively, where $\varphi(\alpha, t) = \exp(-t/\alpha\gamma(\theta_F - \theta_N t))$; λ_U represents the average channel power gain.

Proof. The CDF of U can be written as

$$F_U(u) = \Pr(\gamma\theta_F \rho < (\gamma\theta_N \rho + 1)u). \quad (28)$$

After some basic manipulations, (28) can be rewritten as

$$F_U(u) = \Pr \left(\rho < \frac{u}{\gamma(\theta_F - \theta_N u)} \right), \quad (29)$$

if $\rho < \theta_F/\theta_N$; otherwise, $F_U(u) = 1$. After some calculation steps, the PDF of U can be obtained as presented in equation (27). This completes the proof of Lemma 1. \square

For the sake of notational convenience, let $Y_j \triangleq |h_{SF_j}|^2$. After some algebra manipulations, since Y_j is a nonnegative random variable and constants are strictly positive constants, Φ in (25) can be further obtained as

$$\begin{aligned} \Phi &= \Pr\left(Y_j < \frac{\gamma_{\text{th},F_b} - 1 + \gamma_{\text{th},F_b} t}{\gamma(\theta_F - \theta_N(\gamma_{\text{th},F_b} - 1 + \gamma_{\text{th},F_b} t))}\right) \\ &= \int_0^{(\gamma_{\text{th},F_b} - 1 + \gamma_{\text{th},F_b} t)/\gamma(\theta_F - \theta_N(\gamma_{\text{th},F_b} - 1 + \gamma_{\text{th},F_b} t))} f_{Y_j}(y) dx \\ &= \begin{cases} 1 - \varphi(\lambda_{SF}, \gamma_{\text{th},F_b} - 1 + \gamma_{\text{th},F_b} t), & \text{if } \frac{1}{\theta_N \gamma_{\text{th},F_b}} - 1 > t, \\ 1, & \text{if } \frac{1}{\theta_N \gamma_{\text{th},F_b}} - 1 \leq t. \end{cases} \end{aligned} \quad (30)$$

By plugging (27) and (30) into (25), since $\theta_F/\theta_N \geq 1/\gamma_{\text{th},F_b} \theta_N - 1$, the P_{SOP,F_b} can be further expressed as

$$P_{\text{SOP},F_b} = \int_0^{1/\gamma_{\text{th},F_b} \theta_N - 1} \prod_{j=1}^M [1 - \varphi(\lambda_{SF}, \gamma_{\text{th},F_b} - 1 + \gamma_{\text{th},F_b} t)]$$

$$\begin{aligned} &\cdot \frac{\theta_F}{\lambda_{SE} \gamma (\theta_F - \theta_N t)^2} \varphi(\lambda_{SE}, t) dt \\ &+ \int_{1/\gamma_{\text{th},F_b} \theta_N - 1}^{\theta_F/\theta_N} \frac{\theta_F}{\lambda_{SE} \gamma (\theta_F - \theta_N t)^2} \varphi(\lambda_{SE}, t) dt. \end{aligned} \quad (31)$$

Similar to (20), we rely on the binomial theorem [38, eq. (1.111)]. Consequently, (31) can be further written as

$$\begin{aligned} P_{\text{SOP},F_b} &= \int_0^{1/\gamma_{\text{th},F_b} \theta_N - 1} \sum_{k=0}^M \binom{M}{k} (-1)^k \\ &\cdot \exp\left(-\frac{k(\gamma_{\text{th},F_b} - 1 + \gamma_{\text{th},F_b} t)}{\lambda_{SF} \gamma [\theta_F - \theta_N(\gamma_{\text{th},F_b} - 1 + \gamma_{\text{th},F_b} t)]}\right) \\ &\cdot \frac{\theta_F}{\lambda_{SE} \gamma (\theta_F - \theta_N t)^2} \exp\left(-\frac{t}{\lambda_{SE} \gamma (\theta_F - \theta_N t)}\right) dt \\ &+ \int_{1/\gamma_{\text{th},F_b} \theta_N - 1}^{\theta_F/\theta_N} \frac{\theta_F}{\lambda_{SE} \gamma (\theta_F - \theta_N t)^2} \exp\left(-\frac{t}{\lambda_{SE} \gamma (\theta_F - \theta_N t)}\right) dt. \end{aligned} \quad (32)$$

To the best of the authors' knowledge, it is very difficult to obtain the exact closed-form expression of (32). Thus, in this paper, we approximate (32) using Gaussian-Chebyshev quadrature [39, eq. (25.4.38)]. First, to utilize the Gaussian-Chebyshev quadrature, the range of (32) can be coordinated as

$$\begin{aligned} P_{\text{SOP},F_b} &= \beta_1 \int_{-1}^1 \sum_{k=0}^M \binom{M}{k} (-1)^k \exp\left(-\frac{k(\gamma_{\text{th},F_b} - 1 + \gamma_{\text{th},F_b}(\beta_1 x + \beta_1))}{\lambda_{SF} \gamma [\theta_F - \theta_N(\gamma_{\text{th},F_b} - 1 + \gamma_{\text{th},F_b}(\beta_1 x + \beta_1))]\right) \\ &\cdot \frac{\theta_F}{\lambda_{SE} \gamma (\theta_F - \theta_N(\beta_1 x + \beta_1))^2} \exp\left(-\frac{\beta_1 x + \beta_1}{\lambda_{SE} \gamma (\theta_F - \theta_N(\beta_1 x + \beta_1))}\right) dx \\ &+ \beta_2 \int_{-1}^1 \frac{\theta_F}{\lambda_{SE} \gamma (\theta_F - \theta_N(\beta_2 x + \beta_3))^2} \exp\left(-\frac{\beta_2 x + \beta_3}{\lambda_{SE} \gamma (\theta_F - \theta_N(\beta_2 x + \beta_3))}\right) dx, \end{aligned} \quad (33)$$

where $\beta_1 = ((1/\gamma_{\text{th},F_b} \theta_N) - 1)/2$, $\beta_2 = ((\theta_F/\theta_N) - (1/\gamma_{\text{th},F_b} \theta_N) + 1)/2$, $\beta_3 = ((\theta_F/\theta_N) + (1/\gamma_{\text{th},F_b} \theta_N) - 1)/2$. Next, to approximate P_{SOP,F_b} in (33), (33) can be transformed using the fact that

$$\int_{-1}^1 \frac{f(x) \sqrt{1-x^2}}{\sqrt{1-x^2}} dx = \sum_{i=1}^N w_i \sqrt{1-\tau_i^2} f(x_i), \quad (34)$$

where $w_i = \pi/N$, $\tau_i = \cos(((2i-1)/2N)\pi)$, and N is the number of terms, respectively. Plugging (33) into (34), and after some manipulations, eventually, the tight approximated closed-form expression for SOP of the selected far user can be obtained as

$$P_{\text{SOP},F_b} = \beta_1 \sum_{i=1}^N \frac{\pi}{N} \sqrt{1-\tau_i^2} \sum_{k=0}^M \binom{M}{k} (-1)^k \cdot \exp\left(-\frac{k(\gamma_{\text{th},F_b} - 1 + \gamma_{\text{th},F_b}(\beta_1 \tau_i + \beta_1))}{\lambda_{SF} \gamma [\theta_F - \theta_N(\gamma_{\text{th},F_b} - 1 + \gamma_{\text{th},F_b}(\beta_1 \tau_i + \beta_1))]\right)$$

$$\begin{aligned} &\cdot \frac{\theta_F}{\lambda_{SE} \gamma [\theta_F - \theta_N(\beta_1 \tau_i + \beta_1)]^2} \\ &\cdot \exp\left(-\frac{\beta_1 \tau_i + \beta_1}{\lambda_{SE} \gamma [\theta_F - \theta_N(\beta_1 \tau_i + \beta_1)]}\right) \\ &+ \beta_2 \sum_{i=1}^N \frac{\pi}{N} \sqrt{1-\tau_i^2} \frac{\theta_F}{\lambda_{SE} \gamma [\theta_F - \theta_N(\beta_2 \tau_i + \beta_3)]^2} \\ &\cdot \exp\left(-\frac{\beta_2 \tau_i + \beta_3}{\lambda_{SE} \gamma [\theta_F - \theta_N(\beta_2 \tau_i + \beta_3)]}\right). \end{aligned} \quad (35)$$

3.2. The Asymptotic Analysis. In this subsection, we derive the asymptotic SOP in the high SINR regime, which is mathematically described as $\lambda_{SF} \rightarrow \infty$ and $\lambda_{SN} = \beta \lambda_{SF}$ ($\beta > 1$) [21, 40]. This expression gives insight into the behavior of

Input: system parameters such as γ_{th,N_b} , γ_{th,F_b} , λ_{SN} , λ_{SF} , λ_{SE} , θ_N , θ_F , γ ; and the given optimization parameters such as step size, $s_t = 10^{-2}$, search length, $\Delta k = 1$

Output: θ_{N^*}

- (1) Assign iteration index to the initial: $k \leftarrow 1$
- (2) Choose a starting point of the searching optimal value: $\theta_{N_k} \leftarrow 10^{-9}$
- (3) **while** $P_{\text{TSOP}}(\theta_{N_k}) > P_{\text{TSOP}}(\theta_{N_k} + s_t \Delta k)$ **do**
- (4) Update the searching optimal value: $\theta_{N_{k+1}} \leftarrow \theta_{N_k} + s_t \Delta k$, $k \leftarrow k + 1$
- (5) **end while**
- (6) **return** θ_{N_k}

ALGORITHM 1: The Descent-based Algorithm for Finding θ_{N^*} .

the secrecy outage for high SINR. Using the Taylor's series approximation of the term, that is, $\exp(-a/x) \approx 1 - a/x$, and after some algebraic manipulations, the asymptotic SOP of the selected near user can be obtained as

$$P_{\text{SOP},N_b}^{\text{asym}} = \sum_{n=0}^K \binom{K}{n} (-1)^n \cdot \frac{\beta \lambda_{\text{SF}}}{n \gamma_{\text{th},N_b} + \beta \lambda_{\text{SF}}} \left(1 - \frac{n(\gamma_{\text{th},N_b} - 1)}{\gamma \theta_N \beta \lambda_{\text{SF}}} \right). \quad (36)$$

Similar to the asymptotic SOP for the selected near user, the asymptotic SOP for selected far user can be expressed as

$$P_{\text{SOP},F_b}^{\text{asym}} = \beta_1 \sum_{i=1}^N \frac{\pi}{N} \sqrt{1 - \tau_i^2} \cdot \sum_{k=0}^M \binom{M}{k} (-1)^k \frac{\theta_F}{\lambda_{\text{SE}} \gamma [\theta_F - \theta_N (\beta_1 \tau_i + \beta_1)]^2} \cdot \exp \left(- \frac{\beta_1 \tau_i + \beta_1}{\lambda_{\text{SE}} \gamma [\theta_F - \theta_N (\beta_1 \tau_i + \beta_1)]} \right) \cdot \left(1 - \frac{k(\gamma_{\text{th},F_b} - 1 + \gamma_{\text{th},F_b} (\beta_1 \tau_i + \beta_1))}{\gamma [\theta_F - \theta_N (\gamma_{\text{th},F_b} - 1 + \gamma_{\text{th},F_b} (\beta_1 \tau_i + \beta_1))] \lambda_{\text{SF}}} \right) + \beta_2 \sum_{i=1}^N \frac{\pi}{N} \sqrt{1 - \tau_i^2} \frac{\theta_F}{\lambda_{\text{SE}} \gamma [\theta_F - \theta_N (\beta_2 \tau_i + \beta_3)]^2} \cdot \exp \left(- \frac{\beta_2 \tau_i + \beta_3}{\lambda_{\text{SE}} \gamma [\theta_F - \theta_N (\beta_2 \tau_i + \beta_3)]} \right). \quad (37)$$

4. Optimal Analysis of the Power Allocation Coefficients θ_N

In this section, we carry out the optimal analysis of the power allocation coefficient θ_N . Specifically, using the descent algorithm [41], we propose a descent-based algorithm (Algorithm 1) for finding the optimal point of θ_N , denoted as θ_{N^*} , which results from the minimum value of the total secrecy outage probability (TSOP) as follows.

In our paper, the optimization algorithm is applied to obtain the optimal power allocation coefficient of $\theta_N \in$

(0, 0.5) that minimizes the TSOP. The process of the proposed optimization algorithm can be explained as follows.

- (i) At the starting point θ_{N_k} , we determine a descent direction satisfying $P_{\text{TSOP}}(\theta_{N_k}) > P_{\text{TSOP}}(\theta_{N_{k+1}})$, where k presents the index of the iteration.
- (ii) We update the searching optimal value, that is, $\theta_{N_{k+1}} = \theta_{N_k} + s_t \Delta k$, where s_t means the step size. If $\theta_{N_k} < \theta_{N_{k+1}}$, we can obtain $P_{\text{TSOP}}(\theta_{N_k}) > P_{\text{TSOP}}(\theta_{N_{k+1}})$; otherwise θ_{N_k} is optimal.
- (iii) As we can see, when θ_{N_k} is its optimal value, $P_{\text{TSOP}}(\theta_{N_k})$ becomes the smallest value. Therefore, the iteration process of updating θ_{N_k} will be stopped when $P_{\text{TSOP}}(\theta_{N_k}) < P_{\text{TSOP}}(\theta_{N_{k+1}})$.

Please note that the proposed algorithm is operated on the system parameters collected through CSI estimation process before data transmission process.

5. Numerical Results

In this section, we present the representative numerical results to illustrate the achievable performance of the proposed scheme. Monte Carlo simulation results are generated to validate the developed analysis. In simulation setting, we assume that positions of the source S, the cluster of near users, the cluster of far users, and the eavesdropper E are randomly deployed satisfying some given distance constraints. Specifically, we set that the distance between S and the cluster near users is $d_{\text{SN}} = 10\text{m}$, the distance between S and the cluster of far users is $d_{\text{SF}} = 20\text{m}$, and the distance between S and eavesdropper is $d_{\text{SE}} = 30\text{m}$, respectively. It is noted that although multiple near or far users are located at the same location, their channel characteristics are different from one to another. The power allocation coefficients of the near user (θ_N) and far user (θ_F) are 0.2 and 0.8, respectively. Additionally, the reference distance $d_0 = 1\text{m}$, and power degradation at d_0 is $L = 30$ (dB), the path-loss exponent $\epsilon = 2.7$.

Figure 2 presents the performance comparison of the BSNBSF scheme and random near user and random far user (RNRF) scheme, in which the number of the near users is 3, and the number of the far users is 3, respectively. As can be seen in Figure 2, the SOP of the BSNBSF scheme is lower than that of random selection scheme. The reason is that

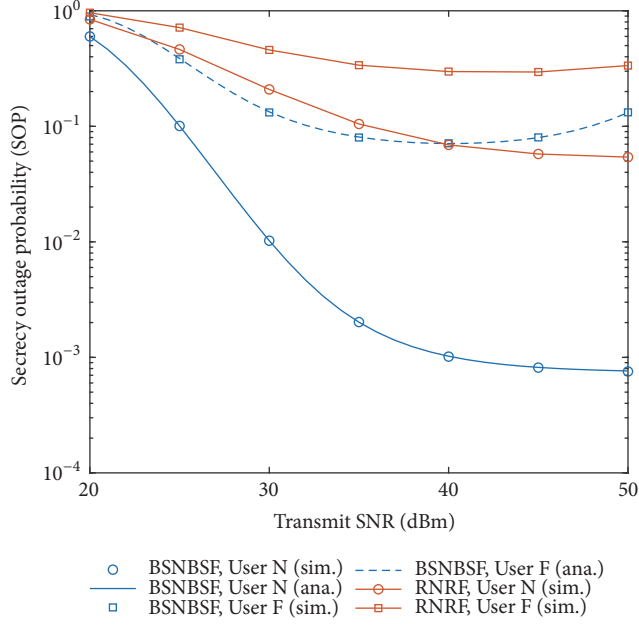


FIGURE 2: Performance comparison between the proposed BSNBSF scheme and the RNRF scheme with secrecy outage probability as a function of the transmit SNR, where $\theta_N = 0.2$, $R_{th,N_b} = R_{th,F_b} = 0.1$ bps/Hz.

the proposed scheme considers the secrecy channel capacity to select the near user and far user, respectively. When the transmit power increases, the SOP of the selected near user is increased until it reaches a performance floor. Different from the case of the selected near user, the SOP of the selected far user is plotted as in convex pattern with respect to the transmit SNR.

Next, we investigate the TSOP of the proposed scheme and RNRF scheme, which can be mathematically defined as [23]

$$P_{TSOP} = 1 - (1 - P_{SOP,N_b})(1 - P_{SOP,F_b}). \quad (38)$$

Figure 3 illustrates the impact of the transmit SNR and the number of near and far users on the performance of the proposed scheduling scheme. As can be seen in Figure 3, increasing the number of near and far users does not improve the performance of the RNRF while the performance of the proposed scheme is improved when the number of the near and far users is higher. The reason is that the BSNBSF scheme exploits the difference in channel conditions between users to select the best near and far users pair.

In Figure 4, we plot the SOP as a function of the transmit SNR with different numbers of the near user and the far user, respectively. As can be observed in Figure 4, the SOP decreases when the number of the near user increases. The reason is that the security performance increases when more nodes take into account the data transmission. In contrast to the case of near user, when the number of the far user increases, the secrecy performance is impacted a little bit. One of possible reasons is that the channel condition of the far user is not so much stronger than that of near user.

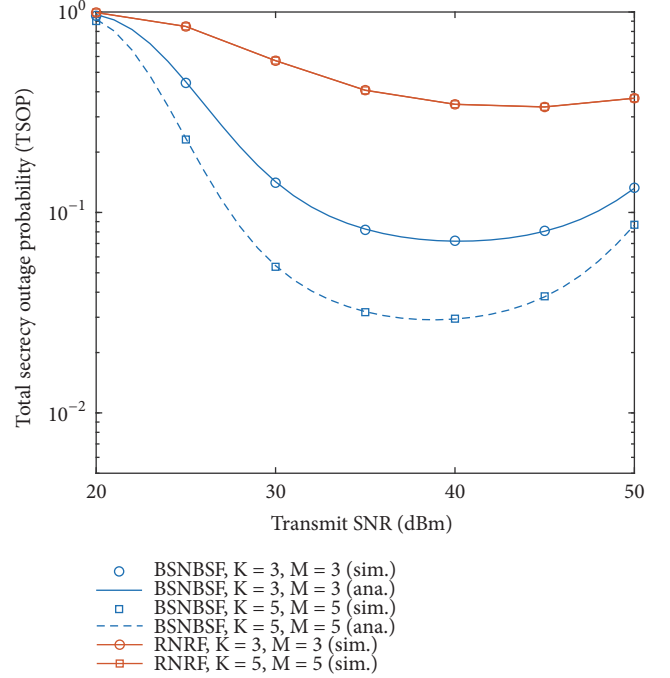


FIGURE 3: Illustration of the impact of the number of near users and far users as a function of the transmit SNR, where $R_{th,F_b} = R_{th,N_b} = 0.1$.

Thus, security performance does not have much effect on the number of far participants. Additionally, we can observe that the results of the asymptotic analysis tightly approximate the closed-form analysis as a function of the increase of average far user channel power gain.

Figure 5 illustrates the TSOP as a function of the distance between the base station and eavesdropper with different numbers of the near users and the far users. As can be seen in Figure 5, when the distance between the base station and eavesdropper increases, the TSOP decreases. The reason is that, when the distance between the base station and eavesdropper increases, it is difficult for the eavesdropper to intercept the information between the legitimate users. Additionally, we can observe that the proposed scheme has better secrecy performance than the benchmarked scheme with the same transmit power.

Figure 6 presents the TSOP as a function of the secrecy target data rate, R_{th} (bps/Hz), with different numbers of the near users and the far users. As can be seen in Figure 6, the total secrecy outage probability increases when the secrecy target data rate increases. This means that if the base station is allowed to transmit with a higher secrecy data rate (in order to obtain higher secrecy throughput), the data transmission will be vulnerable to the eavesdropper.

We investigate the effect on power allocation mechanism on the secrecy performance of the proposed scheduling scheme as shown in Figure 7, where the total secrecy outage probability of the selected user pair is plotted as a function of the transmit power and power allocation coefficient of the near user, θ_N . It is noted that $\theta_F = 1 - \theta_N$. As can be observed, the TSOP poses a complicated convex characteristic with

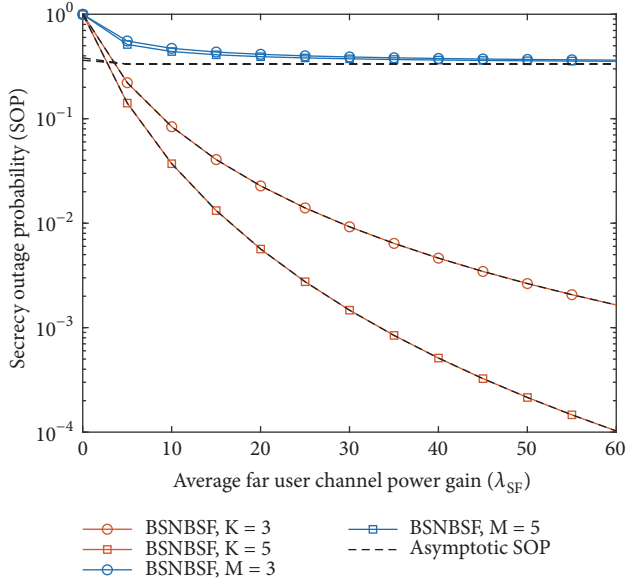


FIGURE 4: Illustration of the impact of the number of near users and far users on the secrecy outage probability as a function of the average far user channel power gains, where transmit SNR = 30 dBm, $R_{th,F_b} = R_{th,N_b} = 0.1$ bps/Hz.

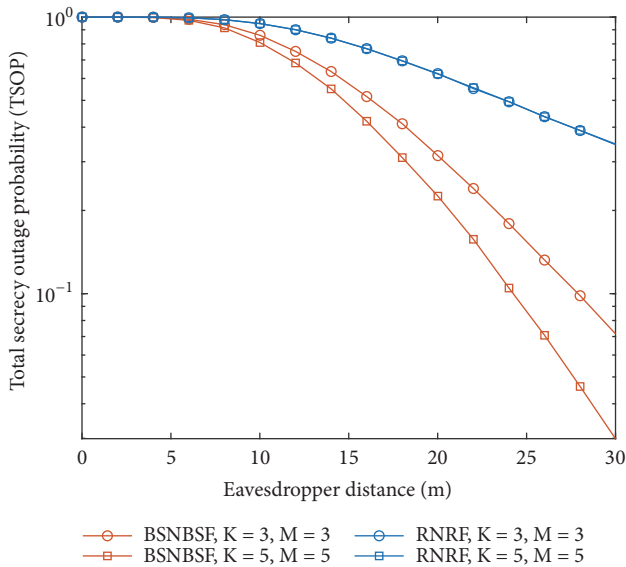


FIGURE 5: Illustration of the total secrecy outage probability as a function of the distance between base station and eavesdropper with different numbers of the near users and the far users, where transmit SNR = 30 dBm, $R_{th,F_b} = R_{th,N_b} = 0.1$ bps/Hz.

respect to θ_N . More specifically, the total secrecy outage probability is a convex function with respect to θ_N when the transmit SNR is less than 30 dBm or greater than 45 dBm under our setting, while it is not a convex function when the transmit power is in the range from 30 dBm to 45 dBm. Hence, we apply the optimization algorithm for finding the minimum power allocation coefficient of the near user, θ_N , when the transmit SNR is less than 30 dBm.

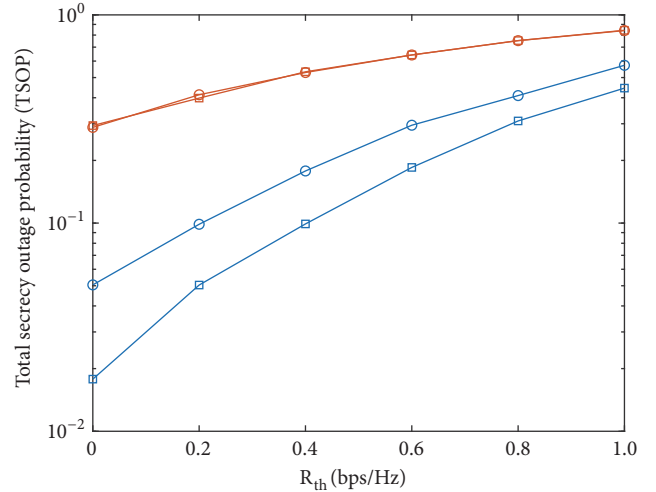


FIGURE 6: Illustration of the total secrecy outage probability as a function of the secrecy target data rate, R_{th} (bps/Hz), with different numbers of the near users and far users, where transmit SNR = 30 dBm.

Figure 8 illustrates the TSOP with different transmit SNR as a function of the power allocation coefficient of the near user, denoted as θ_N . When the transmit SNR increases, the TSOP decreases. Additionally, there is the optimal value of θ_N where the TSOP is minimum as presented in Figure 8. It is noted that the minimum TSOPs are obtained using the proposed descent-based search method.

Finally, we investigate the secrecy performance improvements of the proposed scheme in terms of the secrecy sum throughput as a function of the transmit SNR. The secrecy sum throughput can be defined as [42]

$$\mathcal{T}_{\text{sum}} = (1 - P_{\text{SOP},N_b}) R_{th,N_b} + (1 - P_{\text{SOP},F_b}) R_{th,F_b}. \quad (39)$$

As can be observed in Figure 9, comparing the proposed scheme with the RNRF scheme, the proposed scheme significantly improves the secrecy sum throughput. More specifically, when the number of the near and far users increases, the secrecy sum throughput increases. Different from the proposed scheme, the RNRF scheme does not affect the number of the near and far users. The reason is that, when the near and far users are selected in the proposed system, we consider the channel condition of the main channel and eavesdropper channel. However, the benchmarked scheme does not consider that condition to select the near and far users, respectively.

6. Conclusion

In this paper, we propose the opportunistic scheduling scheme to enhance the secrecy performance in multiuser NOMA system. The proposed BSNBSF scheme aims to improve the physical layer security of the considered NOMA system. Specifically, the BSNBSF scheme selects the

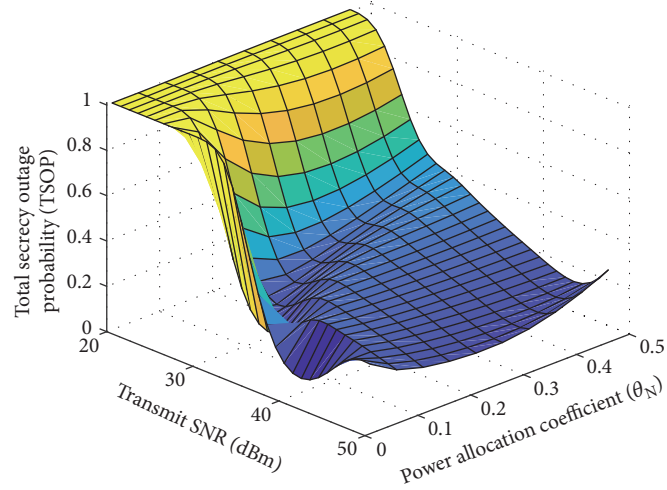


FIGURE 7: The total secrecy outage probability of the selected users pair as a function of the transmit SNR and the power allocation coefficients of the near user, with $K = 3$, $M = 3$, $R_{th,N_b} = R_{th,F_b} = 0.1$ bps/Hz.

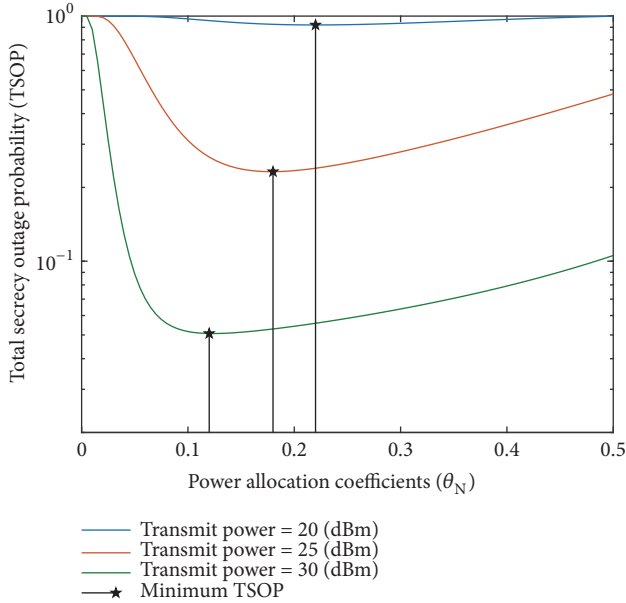


FIGURE 8: Illustration of the total secrecy outage probability with different transmit power as a function of the power allocation for the near user (θ_N), with $K = 5$, $M = 5$, $R_{th,N_b} = R_{th,F_b} = 0.1$ bps/Hz.

user pair by estimating both main channel and eavesdropper channel characteristics to select the most robust near and far users, respectively. The exact closed-form expression for the SOP of the selected near user and the tight approximated closed-form expression for the SOP of the selected far user are presented. In order to get more insightful results, the asymptotic results for the SOP of the selected near user and the selected far user are obtained. Moreover, we propose the optimization algorithm, called the descent-based search algorithm, to find the optimal value of θ_N that minimizes the TSOP when the transmit SNR is less than 35 dBm. The obtained results are verified by the computer simulation. From the numerical results, the proposed scheme provides

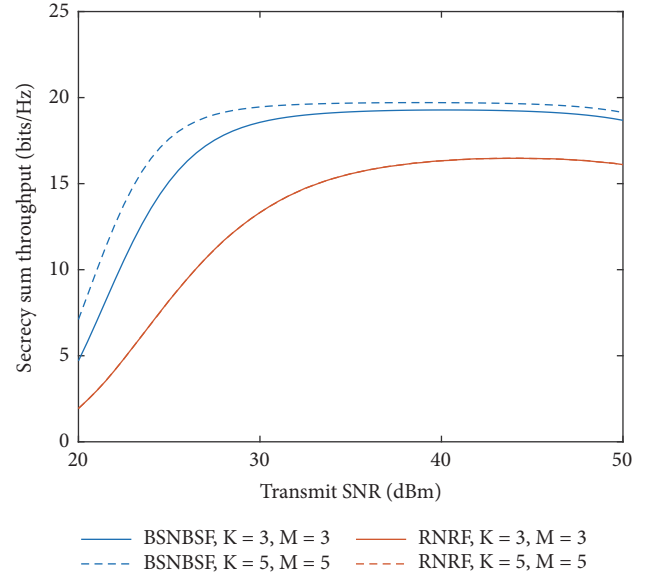


FIGURE 9: Illustration of the secrecy sum throughput with the different numbers of the near users and far users as a function of the transmit power, where $R_{th,F_b} = R_{th,N_b} = 0.1$ bps/Hz.

better secrecy performance compared to that of the RNRF scheme. Additionally, the increasing number of participant near and/or far users improves the robustness of the BSNBSF scheme. The descent-based search algorithm has been proposed to find out the optimal value of θ_N^* that minimizes the secrecy performance. The BSNBSF scheme can also support better performance than the RNRF scheme in terms of the secrecy sum throughput.

Data Availability

The data used to support the findings of this study are available from the corresponding author upon request.

Disclosure

This article is the extended version based on International Conference on Ubiquitous and Future Networks (ICUFN 2018), Prague, Czech Republic, July 2018 [43].

Conflicts of Interest

The authors declare that there are no conflicts of interest regarding the publication of this paper.

Acknowledgments

This work was supported by the Basic Science Research Program through the National Research Foundation of Korea (NRF) funded by the Ministry of Education (Grant no. 2016R1D1A1B03934898) and by the Leading Human Resource Training Program of Regional Neo Industry through the National Research Foundation of Korea (NRF) funded by the Ministry of Science, ICT and future planning (Grant no. 2016H1D5A1910577).

References

- [1] IMT-2020 (5G) Promotion Group, "5G Vision and Requirements," *White Paper*, pp. 1–18, 2015, Available: <http://www.imt-2020.org.cn/en/documents/download/3>.
- [2] NTT DOCOMO, "5G radio access: Requirements, concept and technologies," *White Paper*, June 2014.
- [3] K. Saito, Y. Saito, and Y. Kishiyama, "Special articles on 5G technologies toward deployment," *NTT DOCOMO Technical Journal*, vol. 17, no. 4, pp. 16–28, 2016.
- [4] Y. Saito, Y. Kishiyama, A. Benjebbour, T. Nakamura, A. Li, and K. Higuchi, "Non-orthogonal multiple access (NOMA) for cellular future radio access," in *Proceedings of the IEEE 77th Vehicular Technology Conference (VTC '13)*, pp. 1–5, Dresden, Germany, June 2013.
- [5] L. Dai, B. Wang, Y. Yuan, S. Han, C. I, and Z. Wang, "Non-orthogonal multiple access for 5G: solutions, challenges, opportunities, and future research trends," *IEEE Communications Magazine*, vol. 53, no. 9, pp. 74–81, 2015.
- [6] Z. Ding, Y. Liu, J. Choi et al., "Application of Non-Orthogonal Multiple Access in LTE and 5G Networks," *IEEE Communications Magazine*, vol. 55, no. 2, pp. 185–191, 2017.
- [7] M. Shirvanimoghaddam, M. Dohler, and S. J. Johnson, "Massive Non-Orthogonal Multiple Access for Cellular IoT: Potentials and Limitations," *IEEE Communications Magazine*, vol. 55, no. 9, pp. 55–61, 2017.
- [8] J. Chen, L. Yang, and M. Alouini, "Physical Layer Security for Cooperative NOMA Systems," *IEEE Transactions on Vehicular Technology*, vol. 67, no. 5, pp. 4645–4649, 2018.
- [9] Y. Wu, A. Khisti, C. Xiao, G. Caire, K. Wong, and X. Gao, "A Survey of Physical Layer Security Techniques for 5G Wireless Networks and Challenges Ahead," *IEEE Journal on Selected Areas in Communications*, vol. 36, no. 4, pp. 679–695, 2018.
- [10] Z. Qin, Y. Liu, Z. Ding, Y. Gao, and M. Elkashlan, "Physical layer security for 5G non-orthogonal multiple access in large-scale networks," in *Proceedings of the 2016 IEEE International Conference on Communications, ICC 2016*, Malaysia, May 2016.
- [11] K. Shim, N. T. Do, and B. An, "Performance analysis of physical layer security of opportunistic scheduling in multiuser multirelay cooperative networks," *Sensors*, vol. 17, no. 2, 2017.
- [12] N. Yang, L. Wang, G. Geraci, M. Elkashlan, J. Yuan, and M. Di Renzo, "Safeguarding 5G wireless communication networks using physical layer security," *IEEE Communications Magazine*, vol. 53, no. 4, pp. 20–27, 2015.
- [13] W. Trappe, "The challenges facing physical layer security," *IEEE Communications Magazine*, vol. 53, no. 6, pp. 16–20, 2015.
- [14] H. V. Poor and R. F. Schaefer, "Wireless physical layer security," *Proceedings of the National Academy of Sciences of the United States of America*, vol. 114, no. 1, pp. 19–26, 2017.
- [15] L. Dong, Z. Han, A. P. Petropulu, and H. V. Poor, "Improving wireless physical layer security via cooperating relays," *IEEE Transactions on Signal Processing*, vol. 58, no. 3, pp. 1875–1888, 2010.
- [16] A. Asadi and V. Mancuso, "A survey on opportunistic scheduling in wireless communications," *IEEE Communications Surveys & Tutorials*, vol. 15, no. 4, pp. 1671–1688, 2013.
- [17] L. Yang, J. Chen, H. Jiang, S. A. Vorobyov, and H. Zhang, "Optimal relay selection for secure cooperative communications with an adaptive eavesdropper," *IEEE Transactions on Wireless Communications*, vol. 16, no. 1, pp. 26–42, 2017.
- [18] L. Fan, N. Yang, T. Q. Duong, M. Elkashlan, and G. K. Karagiannis, "Exploiting direct links for physical layer security in multiuser multirelay networks," *IEEE Transactions on Wireless Communications*, vol. 15, no. 6, pp. 3856–3867, 2016.
- [19] N. T. Do, D. B. Da Costa, T. Q. Duong, and B. An, "A BNBF user selection scheme for NOMA-based cooperative relaying systems with SWIPT," *IEEE Communications Letters*, vol. 21, no. 3, pp. 664–667, 2017.
- [20] Y. Zhang, H.-M. Wang, Q. Yang, and Z. Ding, "Secrecy sum rate maximization in non-orthogonal multiple access," *IEEE Communications Letters*, vol. 20, no. 5, pp. 930–933, 2016.
- [21] Y. Liu, G. Pan, H. Zhang, and M. Song, "On the capacity comparison between MIMO-NOMA and MIMO-OMA," *IEEE Access*, vol. 4, pp. 2123–2129, 2016.
- [22] H. Lei, J. Zhang, K.-H. Park et al., "On secure NOMA systems with transmit antenna selection schemes," *IEEE Access*, vol. 5, pp. 17450–17464, 2017.
- [23] Y. Liu, Z. Qin, M. Elkashlan, Y. Gao, and L. Hanzo, "Enhancing the physical layer security of non-orthogonal multiple access in large-scale networks," *IEEE Transactions on Wireless Communications*, vol. 16, no. 3, pp. 1656–1672, 2017.
- [24] Y. Li, M. Jiang, Q. Zhang, Q. Li, and J. Qin, "Secure beamforming in downlink MISO nonorthogonal multiple access systems," *IEEE Transactions on Vehicular Technology*, vol. 66, no. 8, pp. 7563–7567, 2017.
- [25] B. He, A. Liu, N. Yang, and V. K. N. Lau, "On the design of secure non-orthogonal multiple access systems," *IEEE Journal on Selected Areas in Communications*, vol. 35, no. 10, pp. 2196–2206, 2017.
- [26] Y. Feng, Z. Yang, and S. Yan, "Non-orthogonal multiple access and artificial-noise aided secure transmission in FD relay networks," in *Proceedings of the 2017 IEEE Globecom Workshops (GC Wkshps)*, pp. 1–6, Singapore, December 2017.
- [27] X. Chen, Z. Zhang, C. Zhong, D. W. Ng, and R. Jia, "Exploiting inter-user interference for secure massive non-orthogonal multiple access," *IEEE Journal on Selected Areas in Communications*, vol. 36, no. 4, pp. 788–801, 2018.

- [28] X. Zhao, H. Chen, and J. Sun, "On physical-layer security in multiuser visible light communication systems with non-orthogonal multiple access," *IEEE Access*, vol. 6, pp. 34004–34017, 2018.
- [29] A. Mostafa and L. Lampe, "Physical-layer security for indoor visible light communications," in *Proceedings of the 1st IEEE International Conference on Communications (ICC '14)*, pp. 3342–3347, Sydney, Australia, June 2014.
- [30] D. Deng, C. Li, L. Fan, X. Liu, and F. Zhou, "Impact of antenna selection on physical-layer security of NOMA networks," *Wireless Communications and Mobile Computing*, vol. 2018, Article ID 2390834, 11 pages, 2018.
- [31] H. Lei, J. Zhang, K. Park et al., "Secrecy outage of maximin tas scheme in mimo-noma systems," *IEEE Transactions on Vehicular Technology*, vol. 67, no. 8, pp. 6981–6990, August 2018.
- [32] K. Shim, H. Oh, T. N. Do, and B. An, "A physical layer security-based transmit antenna selection scheme for NOMA systems," in *Proceedings of the 2018 Tenth International Conference on Ubiquitous and Future Networks (ICUFN)*, pp. 597–602, Prague, Czech Republic, July 2018.
- [33] T. N. Do, D. B. da Costa, T. Q. Duong, and B. An, "Improving the performance of cell-edge users in NOMA systems using cooperative relaying," *IEEE Transactions on Communications*, vol. 66, no. 5, pp. 1883–1901, 2018.
- [34] H. Liu, K. J. Kim, K. S. Kwak, and H. V. Poor, "Power splitting-based SWIPT with decode-and-forward full-duplex relaying," *IEEE Transactions on Wireless Communications*, vol. 15, no. 11, pp. 7561–7577, 2016.
- [35] N. T. Do, D. B. Da Costa, T. Q. Duong, V. N. Q. Bao, and B. An, "Exploiting direct links in multiuser multirelay SWIPT cooperative networks with opportunistic scheduling," *IEEE Transactions on Wireless Communications*, vol. 16, no. 8, pp. 5410–5427, 2017.
- [36] T. M. Cover and J. A. Thomas, *Elements of Information Theory*, John Wiley & Sons, 2012.
- [37] K. Shim, N. T. Do, B. An, and S.-Y. Nam, "Outage performance of physical layer security for multi-hop underlay cognitive radio networks with imperfect channel state information," in *Proceedings of the 15th International Conference on Electronics, Information, and Communications, ICEIC 2016*, pp. 1–4, Da Nang, Vietnam, January 2016.
- [38] I. S. Gradshteyn and I. M. Ryzhik, *Table of Integrals, Series, and Products*, Academic Press is an imprint of Elsevier, 7th edition, 2007.
- [39] M. Abramowitz and I. A. Stegun, *Handbook of Mathematical Functions: with Formulas, Graphs, and Mathematical Tables*, vol. 55, Courier Corporation, 1964.
- [40] H. Lei, C. Gao, I. S. Ansari et al., "Secrecy outage performance of transmit antenna selection for MIMO underlay cognitive radio systems over nakagami-m channels," *IEEE Transactions on Vehicular Technology*, vol. 66, no. 3, pp. 2237–2250, 2017.
- [41] S. Boyd and L. Vandenberghe, *Convex Optimization*, Cambridge University Press, 2004.
- [42] A. A. Nasir, X. Zhou, S. Durrani, and R. A. Kennedy, "Relaying protocols for wireless energy harvesting and information processing," *IEEE Transactions on Wireless Communications*, vol. 12, no. 7, pp. 3622–3636, 2013.
- [43] K. Shim, T. N. Do, and B. An, "Improving physical layer security of noma networks by using opportunistic scheduling," in *Proceedings of the 2018 Tenth International Conference on Ubiquitous and Future Networks (ICUFN)*, pp. 262–267, Prague, Czech Republic, July 2018.

Research Article

An Implementation Approach and Performance Analysis of Image Sensor Based Multilateral Indoor Localization and Navigation System

Md. Shahjalal , Md. Tanvir Hossan , Moh. Khalid Hasan ,
Mostafa Zaman Chowdhury , Nam Tuan Le , and Yeong Min Jang 

Department of Electronics Engineering, Kookmin University, Seoul, Republic of Korea

Correspondence should be addressed to Yeong Min Jang; yjang@kookmin.ac.kr

Received 30 April 2018; Revised 10 September 2018; Accepted 4 October 2018; Published 22 October 2018

Academic Editor: Tony T. Luo

Copyright © 2018 Md. Shahjalal et al. This is an open access article distributed under the Creative Commons Attribution License, which permits unrestricted use, distribution, and reproduction in any medium, provided the original work is properly cited.

Optical camera communication (OCC) exhibits considerable importance nowadays in various indoor camera based services such as smart home and robot-based automation. An android smart phone camera that is mounted on a mobile robot (MR) offers a uniform communication distance when the camera remains at the same level that can reduce the communication error rate. Indoor mobile robot navigation (MRN) is considered to be a promising OCC application in which the white light emitting diodes (LEDs) and an MR camera are used as transmitters and receiver, respectively. Positioning is a key issue in MRN systems in terms of accuracy, data rate, and distance. We propose an indoor navigation and positioning combined algorithm and further evaluate its performance. An android application is developed to support data acquisition from multiple simultaneous transmitter links. Experimentally, we received data from four links which are required to ensure a higher positioning accuracy.

1. Introduction

Currently, optical wireless communication (OWC) is extensively used to mitigate the data traffic from mobile communications among which the ultraviolet (UV), infrared (IR), or visible light (VL) spectrums are used as the propagation mediums. The VL spectrum is extensively used by OCC, light fidelity (Li-Fi), and visible light communication (VLC) [1, 2]. OCC is becoming a promising technology in terms of localization and navigation because of global positioning system (GPS) using radio frequency (RF) based wireless networks such as wireless fidelity (Wi-Fi), ultra wideband (UWB), Bluetooth, and wireless local area network (WLAN) which are not much accurate location based communication services. Also GPS works well only in the case of outdoor applications, such as tracking and robot navigation, and it is considerably difficult to estimate the accurate locations using RF technology in an indoor environment. WLAN based localization schemes, such as AOA, TDOA, and WLAN fingerprint, have several challenges as it was developed

initially only for wireless networking. In the AOA and TDOA approaches the users have to know the locations of access points (APs) and are not able to provide maximum network coverage. Also the localization errors are high for the NLOS cases [3]. Although fingerprint method which uses power of the received signal has recently captured lots of attention, it faces several challenges. Specific RSS measurement is not possible for individual APs due to dense deployment. Moreover, surveying stage is more time consuming and records the RSS for a time period which increases the complexity of the system. Also RSS weakens in case of NLOS propagation due to the presence of obstacles like walls, furnitures, and doors [4]. In addition, if there are many WLANs in a typical region this would cause extra interference between each other, whereas, OCC is a new technology that offers low cost, simple and low latency communication, and higher positioning accuracy. We used smartphone based localization technique using OCC where image is processed by controlling the camera properties so that other lights cannot make any interference among each other. As each

room contains LED light so there is no possibility that objects will make any interruption during the LOS communication.

OCC uses an unlicensed spectrum in which the LED infrastructures are used as the transmitters. LED is an electronic light source in which illumination intensity can be controlled at a high frequency using an externally driven circuit. LED is a useful transmitter because it is energy efficient, has common indoor lighting infrastructures, and is cheap; additionally, a highly accurate data transmission is possible due to the variable luminary properties of LED. Digital data is transmitted through the LED light by varying the properties of LED according to the different modulation schemes. Typically, for low frame rate (25~30 fps) commercial cameras undersampling modulation techniques are used. This technique includes phase-shift on-off keying (PSOOK) [5], frequency-shift on-off keying (FSOOK) [6], and m-array pulse amplitude modulation (PAM) [7].

A color camera, which is used as the receiver for OCC applications, typically comprises an image sensor (IS), lens, and Bayer filter. A camera exhibits several benefits over a photo diode (PD) in terms of the extended field of view (FOV) and because of the fact that the pixels of the IS can receive light from various directions, thereby providing a high signal to noise ratio (SNR). Localization is possible at the cm-level of accuracy in an indoor environment under stable illumination from an external light source. Several reports on positioning using a VLC system have already been proposed. In one report, a VLC-based positioning system in which the LEDs wirelessly transmit the location information has been proposed [8]. The location information signals were received by a PD, and the spatial distribution was measured at each reference point. Further, the information from people or objects can be obtained using map positioning. There are some localization or navigation services using OCC exhibit an external cloud server to store the mapping data and to compute the position at which the camera is connected to server via Wi-Fi or Bluetooth during location estimation [9]. This approach exhibits a few drawbacks because it requires an external server and an additional RF network, which is expensive and time consuming.

For localizing a rolling shutter (RS) camera that was mounted on an MR, the location information should be received using the camera from multiple LEDs. We propose an android phone mounted mobile robot positioning (MRP) approach using multiple frequency-shift keying (MFSK) in which we are able to obtain four locations ID from four different LEDs simultaneously. We enhance distance measurement technique that allows maximum 2 cm error at 100 cm horizontal distance in case of single LED inside the FOV when camera and LED are not even in vertical line-of-sight (LOS). An MRN algorithm is also proposed to navigate MR to different location. Relevant work on indoor localization is described in Section 2. Section 3 describes the overall scenario of the indoor MRP and MRN systems as well as the transmitter characteristics. A brief description of the android application and the openCV libraries, rolling shutter effects, and MR specifications are provided in Section 4. The proposed algorithm and the remaining operational characteristics, such as the camera FOV and the exploration

of ID distribution systems, are described in Section 5. In Section 6, the details of the accuracy enhancement technique are provided. A demonstration scenario and results are presented in Section 7. Finally, this research work concludes in Section 8.

2. Related Works

Currently, camera-bearing mobile phones are commonly used and are important commodities in e-commerce. Therefore, location based services (LBS) have become an important issue. To ensure better performance in LBS, it is mandatory to measure the location of these mobile devices accurately especially indoors.

GPS is a pseudo-lite system, which faces challenges at the point of indoor localization. This system is a LOS based localization solution which accumulates the sensor information from satellites that are located at a considerable distance (20,000 km) from the ground. The signals of the satellites are interrupted by the obstacles on the ground, such as trees and buildings, due to the LOS channel characteristic and the considerable distance between satellites and sensors. Therefore, a considerably large modification is required to make the GPS system to be suitable for indoor localization. For example, the integration of GPS signals with the indoor transmitting antennas has been reported to localize sensor nodes [10]; however, it is not cost effective, and the localization error is observed to be 1 m in delay of 10 sec.

The distinctness and novel characteristics of OWC-based techniques are considered important supporting candidate over existing solutions for indoor localization and navigation scenarios. Several approaches of VL-based localization and navigation schemes for mobiles, PDs, or wearable computers have been reported [11–17]. There is still considerable debate about the value of localization resolution. A lower value of localization resolution was observed from the simulation results of various conditional approaches. An important subpart of OWC is OCC in which the camera receives a signal from the modulated light beam that was observed from an LED. An IS detects the intensity of the metameric LEDs within a fixed indoor environment [18]. The localization performance exhibits a 1-degree orientation measurement, and the calculated resolution was observed to be 1.5 and 3.58 cm for 2D and 3D space, respectively. Without measuring the angular displacement, 0.001-m localization resolution has been observed [19]. In a similar approach, the localization using an LED transmitter and a camera as the receiver has been discussed by other groups [20, 21]. Additionally, the information from an accelerometer sensor has been included; further, the demodulated data from the IS could be used to improve the overall performance in a 3D indoor environment [22].

Popular methods for localization can be used to measure the signal strength of the receiver, i.e., a photodiode or camera. This signal can be either visible light or RF. An RSS-based localization scheme for an aperture-based receiver, which exhibits a wide FOV and a better angular diversity, has been proposed [23]. They derived the Cramer-Rao lower bound of position estimation for improving the overall

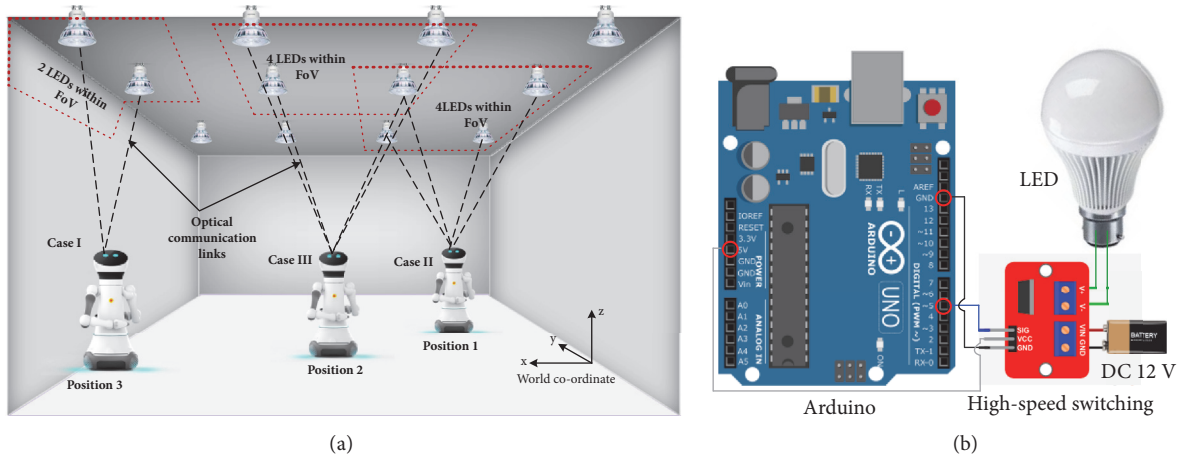


FIGURE 1: A scenario of the proposed model (a) MRP and MRN system using OCC and (b) transmitter set.

performance. Meanwhile, a generic framework of RSS has been introduced to enrich the positioning performance [24]. Alternatively, the combination of spatiotemporal constraints in RSS fingerprint-based localization has achieved the same purpose [25]. Compressive sensing has been applied to improve the localization performance in noisy scenarios [26]. The implication of the RSS approach was also observed in the VL-based positioning schemes [27–29]. Here, the localization resolution was observed to be 4 m [30]. Importantly, an artificial intelligence algorithm that was applied to collect the location-labeled fingerprints was reported for optimizing the overall performance [31, 32]. Although the positioning accuracy that was obtained for the RSS fingerprints was observed to be 80% [33], a 3D space fingerprint required considerable overhead for positioning a high speed object as compared with that obtained in a simpler 2D space fingerprint.

Time-of-arrival (TOA) and time-difference-of-arrival (TDOA) are two methods that have been used several times to provide a solution for localization in indoor environments. A TDOA-based localization scheme has been proposed in which a light beam with a unique frequency was transmitted in different phases [34–36]. A TOA-based localization algorithm has also been developed [37]. The most important issue is that the TOA- and TDOA-based localization schemes are cost-effective and accurate. Furthermore, these schemes depend on the location information from a central node as well as from other reference nodes in the same indoor space. An extended Kalman filter-based TDOA approach that ignores the impact of this dependency on the reference node information has also been proposed [38]. However, deploying such a tracking algorithm is not always advantageous because the extended Kalman filter failed to accurately estimate the position as a first-order approximation.

Angle-of-arrival (AOA) is another method that can be applied for indoor localization. In this approach, the receiver estimates the angle of the transmitted signal by calculating the time difference of arrival from the individual transmitter. Transmitting the gain difference from the LED has been considered by AOA for indoor localization [30, 39, 40]. Simulation results depicted that the average value for

localization resolution was 3.5 cm. However, in our proposed system, it is not essential to gather the angle information from LEDs to measure the position of the camera. The position is calculated with the help of distance comparison among several LEDs (e.g., more than two LEDs). These distances are calculated using the photogrammetry technique [41], where the occupied image area of the LEDs on the image sensor varies with the distance. Furthermore, AOA exhibits some disadvantages, e.g., the accuracy degrades with the increasing distance between the transmitter and receiver and the reflections of the signal from the multipath add some error during the location measurement and require large and complex hardware devices and the shadowing and directivity of the measuring aperture have significant effect on the overall performance of location estimation.

3. Indoor Transmitter Scenario

Figure 1(a) depicts a scenario of the proposed indoor transmitter and receiver scenario for MR positioning and navigation system using OCC. A circular shaped white LED having a diameter of 9.5 cm was used as the transmitter. Because the LED exhibits an altering luminary property, it can flicker at ultrahigh speeds that are beyond the perception of the human eye. The indoor location ID is modulated with a high modulation frequency and encoded with additional bits using an LED driver circuit. This encoded signal is further fed to the LED, which continuously transmits this ID using the flickering light. The driver circuit comprises a 12-V dc power supply, an Arduino board, and a high speed switching device including metal-oxide-semiconductor field-effect transistor (MOSFET). The transmitter set with an LED driver circuit is depicted in Figure 1(b). LEDs are installed on the ceiling, and the location number is transmitted to the MR receiver camera. In our system, transmitters are arranged in a square-shaped regular pattern in which each side of LEDs is 50 cm apart from each other. In this case, the positioning system of the camera is mounted on top of the MR, which maintains an equal height along the z-axis. Therefore, the LEDs transmit the modulated data bits that contain only the (x, y) location information.

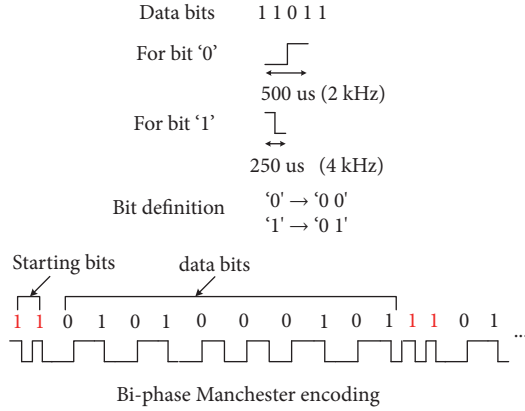


FIGURE 2: Transmitted data bit mechanisms.

The visual flickering in an optical wireless communication is a major problem that can be defined as the change in the illumination of the LED when it transmits a binary '1', '0' code-word in terms of the light that is perceived by the human eyes. Generally, human eyes can avoid flickering if the data is modulated with a frequency that is greater than 200 Hz [42]. The LED transmitter should be driven using the accurate LED driver circuit to avoid any noticeable flicker. Multiple frequency-shift keying (MFSK) is used as the modulation technique to generate the modulated binary code-words using the LED driver circuit. Figure 2 depicts the characteristics of the transmitted bit pattern. Our proposed study uses the modulation frequencies 2 and 4 kHz, which are safe enough to avoid flickering. Further, the modulated signal can be encoded using bi-phase Manchester line coding. Each of the binary bits, 1 and 0, is defined using a different code. Bit '1' is defined as '01', whereas bit '0' is defined as '00'. We transmitted five bits of data from each LED. Therefore, in a single indoor system, 32 location IDs can be provided to 32 LEDs. Furthermore, if the actual data is '11011', the encoded signal will be '0101000101' after bi-phase Manchester line coding as shown in Figure 2. Although there are 3 consecutive '0's in this example, the bi-phase Manchester encoding eliminates the possibility of visual flickering because it confirms one transition in the middle of each bit. As this code stream is continuously transmitted, a starting bit symbol '11' is added at the beginning of the code-word to differentiate between every simultaneous code-word.

4. Receiver Characteristics

4.1. Android Application Background. An application is designed for the android studio platform using the camera 2 hardware package which is added in API level 21. Some android features are described in this study that are used to create the camera device and process the requests. One request acts to capture a single frame and output a set of image buffers for the request. A *cameraManager* is required when multiple requests are in queue to maintain the full frame rate. To accumulate the captured frame data a *getCameraCharacteristics* class is used. The image data is encapsulated in *Image* objects and can be directly accessed through a class named

ImageReader using a YUV_420_888 format. The image data is rendered onto a surface with defined size. For processing the captured image frames openCV320 libraries were imported into the application. Initially, the camera shutter speed is controlled to focus only to the white LEDs and to detect only the region of interest (RoI).

4.2. Rolling Shutter Effect. Currently, most of the consumer cameras contain complementary metal-oxide-semiconductor (CMOS) sensors, which include rolling shutter mechanisms. The sequential read-out technique is a key feature of the rolling shutter camera in which each frame is not captured at exactly the same instant [43]. The scene is captured by scanning rapidly, either horizontally or vertically, unlike a global shutter camera in which the complete scene is captured at the same time. In a rolling shutter camera, each row of the pixels is exposed at once at the exposure time. The read-out time protects the rows of pixels from overlapping. In a single captured image, the rolling shutter allows multiple exposures. Therefore, for an LED, which flickers on-off according to the modulated binary bit stream, the captured image contains a bunch of dark and white strips. The width of the strips depends on the modulation frequencies, and the number of strips depends on the distance.

Although a different camera receives signals of similar frequencies from the same transmitter, the width of the strips is different as the specifications of the camera sensors may differ from device to device. In our system, a multiple frequency-modulated signal is transmitted, and the dark and white strips are received at different distances, as depicted in Figure 3. The camera captured the pictures with a fixed clockwise rotation of *ImageView* of 270° . As the distance increases, the size of the LED in the IS decreases; further, the number of strips also decreases because the width remains identical for fixed frequencies at any distance for a particular camera.

4.3. Introduction to MR Functionalities. Localization and navigation are challenging issues in optical camera communication for the existing MRs. The initial requirement is to connect to the input interface of the MR to provide necessary data from the android phone such as the location ID and its distribution system. When a camera captures the rolling images from multiple LEDs, it processes the images and obtains the locations, thereby making a decision about the location distribution system and then feeds the data to the MR. The MR must exhibit a user input interface (UI) to set a target location ID, a data base (DB) to store the ID distribution information, and a display screen to exhibit the location information and the subsequent direction to move after making a decision. Figure 4 depicts the specifications of the MR and its required functionalities. It also exhibits a data and image-processing unit to compare the IDs and a database to store the previous tracking information. The MR receives the IDs and can therefore localize itself. It also has a capability to compare the stored IDs and navigate by itself if the user sets a destination.

5. Operational Principle

5.1. Navigation Algorithm. The objective of the MRN system is to navigate an MR by receiving the locations or location

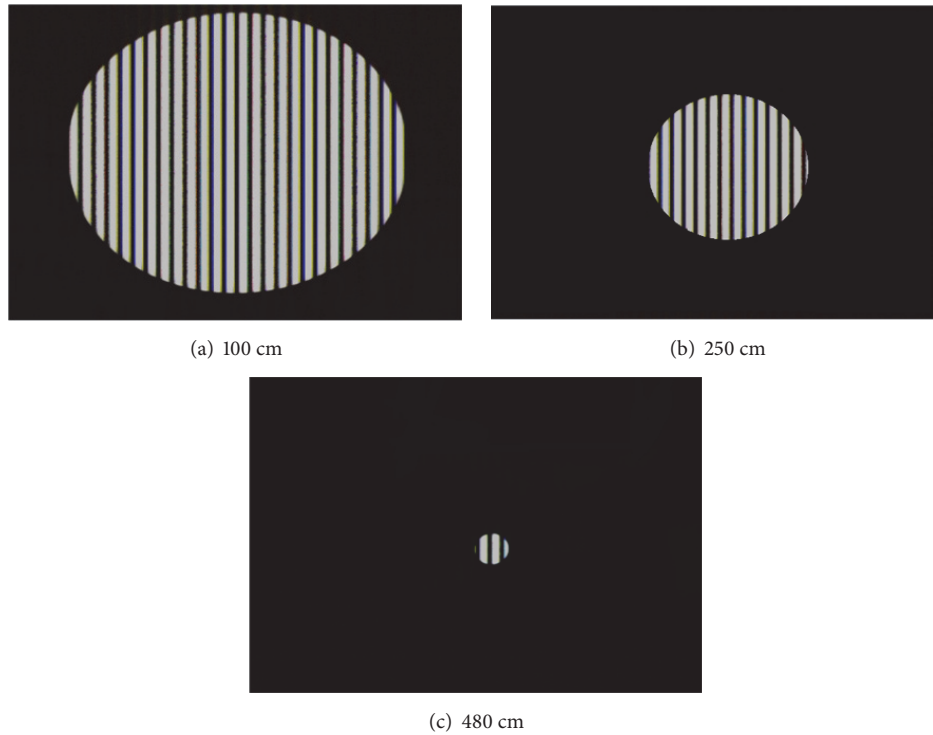


FIGURE 3: Experimentally, the number of dark and white strips decreases with the increase in distance. (a) 52 strips at a distance of 100 cm. (b) 28 strips at a distance of 250 cm. (c) 5 strips at a distance of 480 cm.

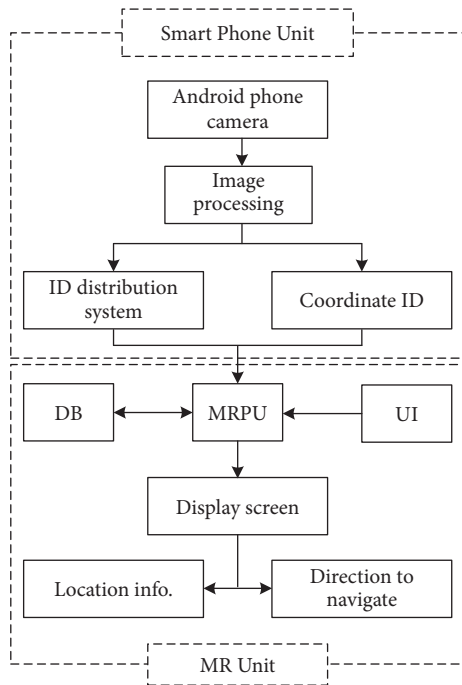


FIGURE 4: Block diagram of the mobile robot functionalities.

ID using multiple LED lights. Figure 5 describes a flowchart of the applied navigation algorithm in our proposed system. A user inputs a target location into the smart phone that is

mounted on the top of an indoor MR. Because the complete environment in the room is unknown to an MR, it should fix its position first, which indicates that a location should be observed inside the room. Therefore, it estimates the number of LEDs that are within the camera’s FOV. To perform navigation, the MR should perceive the direction in which the location values are changing. Thus, a minimum of three LEDs should be within the camera’s FOV, as depicted in Figure 1(a) in previous section. Here, in case I, the IS can only detect two LEDs among which each LED exhibits the same value for the x location; further, it is difficult to observe a variation in the value of the x location. In cases II and III, there are four LEDs within the camera’s FOV as MR is situated deep inside the room. If three or more LEDs are detected using the IS, the smart phone receives the LED locations and compares them with the target location. If the target location matches any of the received locations, the MR moves in a horizontal distance toward the LED that is located directly below the target location.

As mentioned in the previous paragraph, to localize the MR to a floor position of a target LED, we need to measure the horizontal distance from the MR to that floor position. Here, floor position of an LED means the position on the floor which is just below the LED. Suppose, the target LED is transmitting (x, y) location ID. When the MR is located in its initial position as depicted in Figure 6, the implemented android smartphone app calculates the direct distance, D , from the ceiling LED. The direction towards the LED is predicted from the image formation on the IS (image formation technique on IS is well described in [42]). After

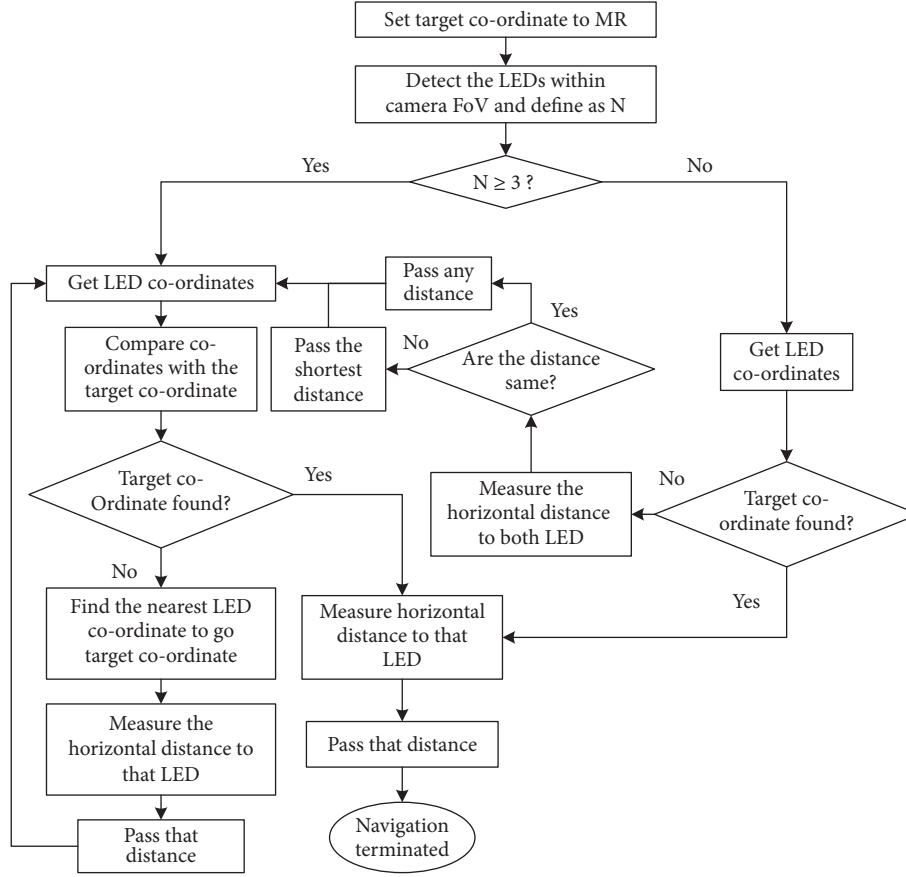


FIGURE 5: The mobile robot navigation flowchart.

obtaining the direct distance, we can easily find the horizontal distance, s , using Pythagoras distance formula for right angle triangle as the vertical distance is fixed inside a room. After calculating the value of s and understanding the direction to move, MR navigates this distance and fixes its location to (x, y) location. If the target location is not matched with any of the received location ID, the MR estimates the nearest LED that is required to reach the destination. Subsequently, the MR traverses a certain amount of distance to go a point that is exactly below that particular LED. Further, the MR again receives the locations of the LEDs that are within camera's FOV. Subsequently, the procedure continues until the destination is reached. If the camera detects two LEDs within its FOV, the MR cannot detect the location distribution system. Therefore, it initially chooses one ID and goes to a point that is located exactly below that LED, and then MR continues with the aforementioned procedure.

5.2. Camera Field of View. We considered the indoor environment to possess a uniform square distribution of LEDs. Figure 7 depicts the manner in which the number of LEDs within camera's FOV depends on different factors such as the height of the room, the distance between two adjacent LEDs, and the angle of view (AOV), i.e., the FOV angle. For the purpose of navigation, the MR should understand the location distribution system among the LEDs. It is obvious

that at least two diagonally located LED locations should be considered to make a decision about the direction in which the X and Y locations are increasing or decreasing. A relation has been derived to estimate the number of LEDs that were captured within the FOV at any time considering the camera view angle, the height of the roof, and the surface area taken by a single LED.

The horizontal and vertical FOV can be estimated using the following two equations:

$$\phi_h = 2 \tan^{-1} \frac{d_h}{2f} \quad (1)$$

$$\phi_v = 2 \tan^{-1} \frac{d_v}{2f} \quad (2)$$

where ϕ_v and ϕ_h are the FOV in vertical and horizontal directions and d_h, d_v are the sensor dimensions, respectively. f represents the focal length of the camera lens. Figure 7 shows the camera FOV and its area is projected vertically on the roof of height h_r . We can represent the area of the FOV using the following equation.

$$A_{FOV} = 4h_r^2 \tan(\phi_v) \tan(\phi_h) \quad (3)$$

Because the LEDs are distributed in a square pattern and each LED separated by a distance a along each side (where $a >$ LED diameter) then each LED will occupy an area of a^2 .

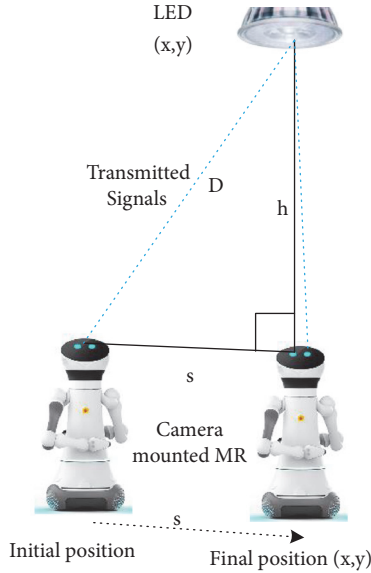


FIGURE 6: Calculation procedure of the distance to move horizontally.

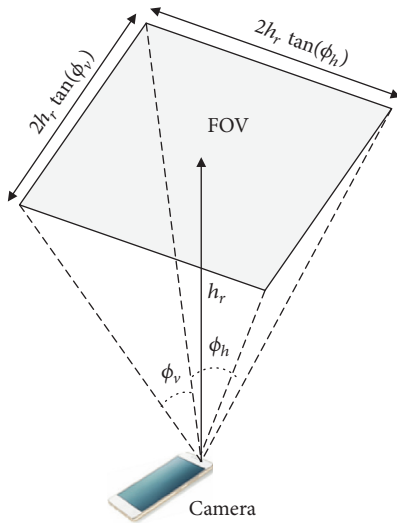


FIGURE 7: Analysis of the camera's FOV.

Now we can find the number of LEDs will be in the camera FOV using (3).

$$N_{LED} = \frac{4h_r^2 \tan(\phi_v) \tan(\phi_h)}{a^2} \quad (4)$$

5.3. Exploring the ID Distribution System. The smart phone that was used to perform this study was a Samsung S7 edge, which contained a 26-mm camera and a focal length of 4.2 mm. The height of the room that was observed using the camera was 2.56 m. We set up the android camera with a height and width of 600 and 800 px, respectively. In a general scenario, there were always at least four LEDs within the camera's FOV under this type of consideration. To define the coordination distribution system, we divided

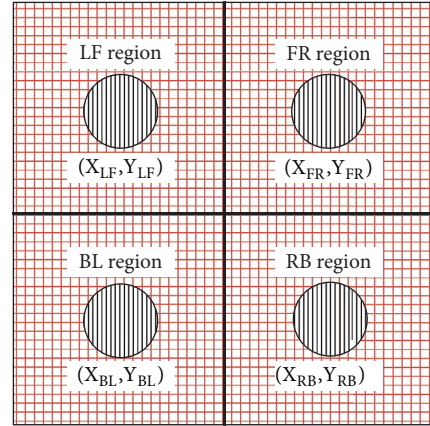


FIGURE 8: Region basis locations selection and exploring their distribution system.

the IS into four regions, i.e., left-front region (LFR), front-right region (FRR), right-back region (RBR), and back-left region (BLR), as depicted in Figure 8, where each region contains an equal number of pixels. The camera will detect a single LED per region and receive the location ID as well. We defined the locations on a regional basis, which are (X_{LF}, Y_{LF}) , (X_{FR}, Y_{FR}) , (X_{RB}, Y_{RB}) , and (X_{BL}, Y_{BL}) , respectively, within the four regions. It is obvious that the LEDs will be present either in both LF and RB regions or in both FR and BL regions. If $X_{LF} < X_{RB}$ or $X_{FR} > X_{BL}$, the x-location increases in the right direction; otherwise, it increases in the left direction. Further, if $Y_{LF} > Y_{RB}$ or $Y_{FR} > Y_{BL}$, the y-location increases in the front direction; otherwise, it increases in the back direction.

6. Performance Analysis

6.1. Measurement of Distance Accuracy. The direct distance from the camera to an LED can be measured by considering a few distance parameters. If D is the direct distance of the LED (x_i, y_j) from the camera lens and d is the distance of the formed image on the sensor from the camera lens, then we can write from the general lens equation:

$$\frac{1}{D} + \frac{1}{d} = \frac{1}{F} \quad (5)$$

$$\frac{d}{D} = \frac{F}{D - F} \quad (6)$$

where F is the focal length of the lens. Here, magnification factor is required to introduce and compare the relative size of the actual size and the detected size on the IS.

The magnification factor, m can be written as follows:

$$m = \sqrt{\frac{a_{ij}}{A_{ij}}} = \frac{d}{D} \quad (7)$$

where A_{ij} is the actual surface area of the nearest LED (x_i, y_j) and the area covered by the detected image on the IS is a_{ij} .

TABLE 1: Distance measurement data from an LED at different floor positions.

Horizontal distance, d_h (cm)	Measured direct distance, (cm)	Actual direct distance, (cm)	Error in distance measurement (cm)	Detected area (px)	1 st Radius, r (px)	2 nd Radius, r' (px)
00	255.5	255.5	0	348		11
10	255.88	255.9	0.02	347		10
20	256.65	256.7	0.05	341		10
30	257.6	257.7	0.1	337		10
40	258.85	259	0.15	336		10
50	260	260.2	0.2	330	11	9
60	262.5	262.8	0.3	324		9
70	264.3	264.7	0.4	314		9
80	267.1	267.7	0.6	306		9
90	269.5	270.61	1.11	298		8
100	272.5	274.5	2	288		8

Normally, it is observed that $F \ll D$; therefore, we can combine the above equation as follows:

$$a_{ij} = m^2 A_{ij} \quad (8)$$

$$a_{ij} = \frac{F^2}{D^2} A_{ij} \quad (9)$$

$$D = F \sqrt{\frac{A_{ij}}{a_{ij}}} \quad (10)$$

where the focal length F and the actual LED size A_{ij} are known. The only requirement is to obtain the detected LED area, a_{ij} , from the IS.

Using (10), the distance can be measured accurately at a position at which the camera is vertically in the LOS of the LED. But when it navigates through some other places which are not just below the LED, can be experienced some errors during this measurement. Because at that time the shape of the circular LED will be seemed like an ellipse to the camera. This happens due to the radial distortion of the camera [44]. The wide-angle camera, short focal-lengths camera, or the fisheye camera are the main reason behind the radial distortion. Determining intrinsic, extrinsic, and distortion coefficient of IS and lens of the camera is required to omit the effect of radial distortion. This radial distortion makes a significant transformation of the projected object from the actual object with a normal focal length. To verify the localization scheme, a back-projection method deploys to measure area of LED from distorted image from read-world space [45]. In the following section we will exhibit a figure to illustrate the accuracy of the distance measurement. Although at the boundary position the accuracy remains greater than 98%, we have undertaken one further step to mitigate this error. Let us take r as the radius of circular LED and the area will be πr^2 . Now when circular shape changes to eclipse, one radius r reduces to r' and the area becomes $\pi r r'$. Table 1, presents the data measured from a LED with a size of 71 cm² located at a ceiling of height of 2.56 m. The pixels allocated for the detected LED at different positions are

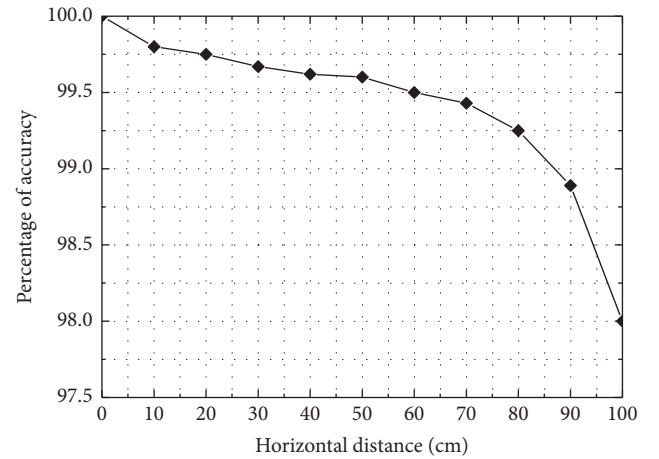


FIGURE 9: Percentage of accuracy of the measured direct distances from the camera to the LED at different horizontal points.

recorded to show at far distance detected contour becomes smaller than nearer. We tabulated the radius of eclipse which is required to calculate the actual size of eclipse and correct the positioning error.

This radius data is integrated within the application and will be called when this radius will be measured by smartphone through image processing. Comparing the existing data with the actual area of the LED can predict to measure the direct distance.

The distance between the LED and the camera changes when the MR moves horizontally. The direct distance from a particular LED is required to calculate the horizontal distance that is required to move and to get the floor location of that particular LED. We used (10) to measure the direct distance between the camera and the LED. We graphically represented the percentage of accuracy that is observed while measuring the direct distance at a particular point on the floor in Figure 9. The distance is measured with 100% accuracy when the camera is situated directly below the LED. When the

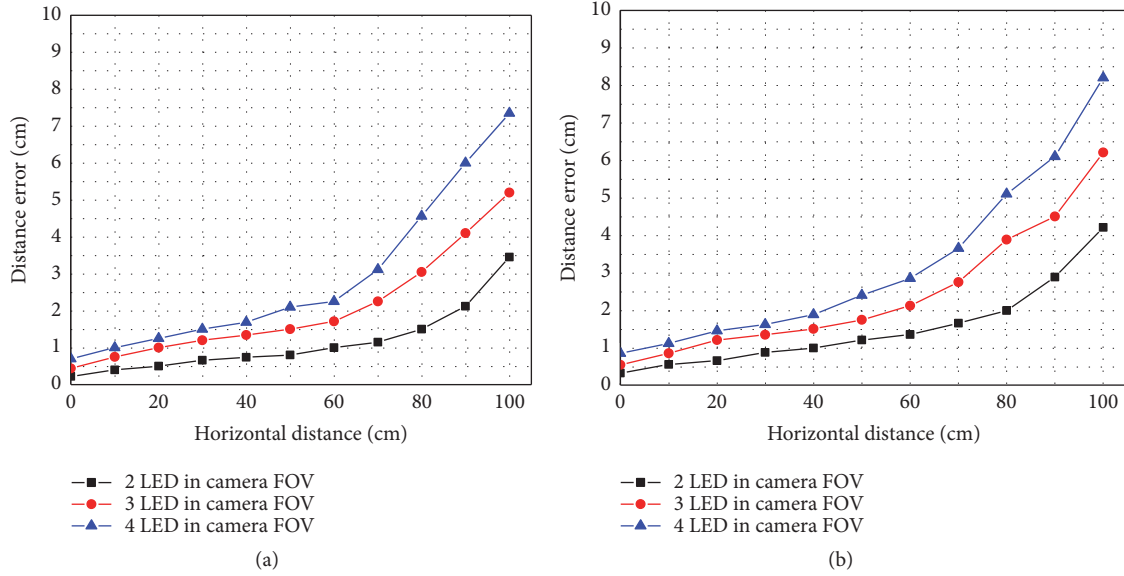


FIGURE 10: Distance error comparison in terms of variation of no. of LEDs inside the camera FOV at different horizontal points. (a) Inter-LED distance = 50 cm and (b) inter-LED distance = 100 cm.

camera is shifted horizontally far away from the floor location of the LED, the accuracy is reduced.

To evaluate the performance of the proposed localization algorithm we have tested the accuracy of measuring the distance for different type of scenarios. We have got the distance measurement error of 2 cm maximum in case of single LED inside the camera FOV. However, when there are multiple LEDs inside the camera FOV, the distance error increases as the probability of LED being at the middle of the IS reduces. Figure 10 depicts the comparison of error in measuring the distance between LEDs and camera for different cases varying the number of LEDs into the camera FOV. We have taken two scenarios: first is for the case where the inter-LED distance is 50 cm and second is for the case where it is 100 cm. In each scenario we have considered 2 to 4 LEDs for the comparison. We started measuring from the floor position of an LED and took 10 more reading going away about 10 cm in each step. We can see from the figure that if there are more LEDs into the IS at the same time, the error for measuring the distance increases. This is because the chance of an LED to be detected at the center of IS is being reduced accordingly. As our system comprises LEDs that are distributed in a rectangular pattern there is more possibility of being 4 LEDs at a time in the IS. And for this case we have to consider up to 7.5 cm distance error for positioning and navigation purpose when the inter-LED distance is 50 cm. But for the second case described in Figure 10(b) the value of the distance error increases up to 8.5 cm for 4 LEDs due to increase of the inter-LED spacing to 100 cm.

Though the distance error reducing with the reduced number of LEDs being allowed into the camera FOV, it is required to have more than two LEDs into the camera FOV to get the navigation information and we should accept this error anyway. Also, we have described a way in this section that can be applied to reduce the distance error to a certain level for moving to a horizontal distance to reach the target LED location increasing the positioning performance.

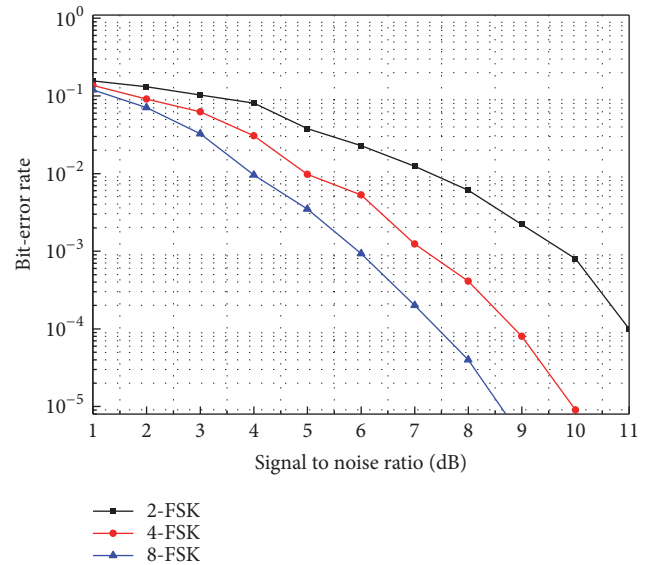


FIGURE 11: BER comparison for M-FSK ($M=2,4,8$) in indoor wireless Rician fading channel.

6.2. *Bit Error Rate for MFSK.* To evaluate bit error rate (BER) performance we considered an indoor wireless Rician fading channel. MFSK is simple and flexible for multilink communication over this channel. It is known [46] that the bit error probability for MFSK is

$$\rho_s = \frac{1}{M} \sum_{i=2}^M (-1)^i \binom{M}{i} \exp \left[- \left(1 - \frac{1}{i} \right) \rho \right] \quad (11)$$

where M is the number of orders and ρ is the instantaneous signal-to-noise ratio (SNR) value. In Figure 11, we depicted a BER comparison graph between different modulation

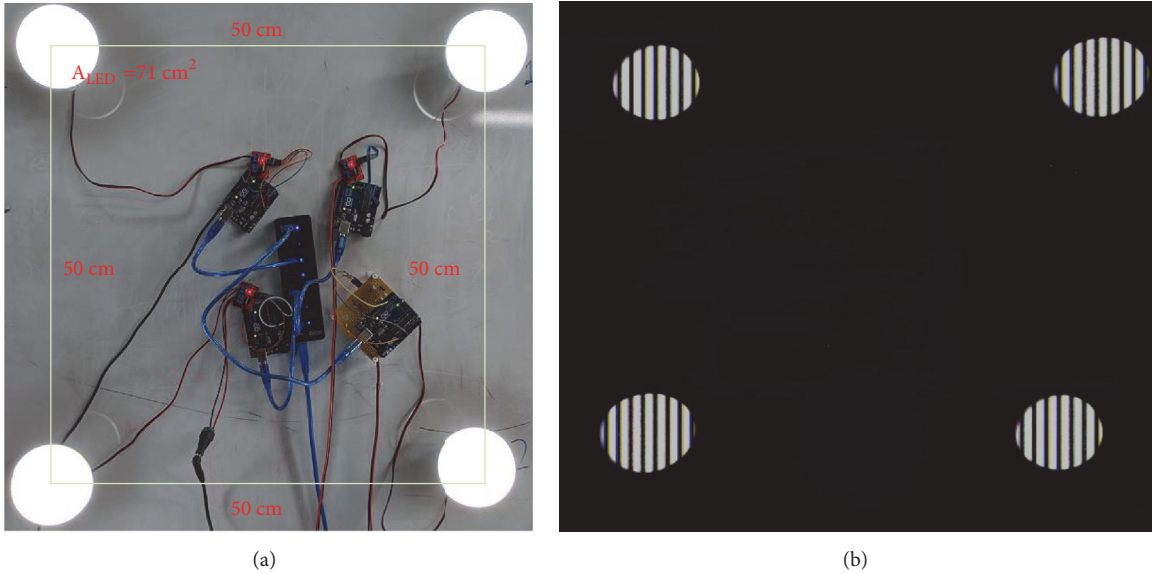


FIGURE 12: Experimental setup. (a) Four LEDs that are 50 cm apart from each other transmit the location IDs. (b) Captured image after setting the exposure time to 1/8000 sec.

orders ($M=2,4,8$). We have seen, for increasing M , bit error probability decreases. When the transmission is done keeping the same bit energy which means that the symbol duration becomes double for the case of 4-FSK compared to 2-FSK, maintaining the same bit rate meanwhile. In such case the BER becomes lower as symbol duration increases with higher modulation index.

7. Demonstration Results

We used a platform to demonstrate our OCC system to evaluate its performance. To understand the ID distribution system, we should receive the location information using a minimum of two diagonally located LEDs that are described in Section 5. The platform comprises four LED transmitter links that are placed in a square shape, as depicted in Figure 12(a). The LEDs are arranged by maintaining a distance of 50 cm between them. For better explanation, we considered these transmitters to be a single unit. These four transmitters are linked continuously and transmit four different locations, which are encoded with the help of a PC and an LED driver circuit.

To focus only on the target-transmitting LED, we controlled the camera exposure time. The exposure time is the duration at which each pixel is exposed to light. Using this process, we can obtain the dark and white strips at a region at which the LEDs are captured by darkening all the parts of the image except the parts that depict the target LEDs. Figure 12(b) depicts the captured image using the Samsung S7 (edge) camera of the transmitting LED unit after setting the camera's `CaptureRequest.SENSOR_EXPOSURE_TIME` to 1/8000 sec. We can observe that all the four LEDs represent the same dark and bright strip width. This is because same modulation frequencies were used for all the four transmitters, and the frequencies ranged from 2 to 4 kHz. Generally,

the characteristics of the rolling image are such that the strips can be formed horizontally. However, in our case, we rotated the image using `imageView` at 270° , and this is the reason for the observation of vertically formed strips.

To demodulate the data from the detected strip pattern we should initially measure the width of each dark and white strip. We know different camera has different frame rate and also for a fixed camera, frame rate fluctuates within a short range. For this reason, the width also varies and as the width is measured in a scale of number of pixels in a row, it should be an integer value. In our system, we observed brighter strips at which the width varied between 5 and 7 pixels, whereas it varied between 1 and 3 pixels for darker strips. Therefore, the midvalue was considered to be four to distinguish between dark and white patterns. When the measured width was greater than four, smart phone will consider the LED to be in the ON state and store a binary '1' value. Otherwise, the LED is assumed to be in the OFF state and stores a '0' value. Figure 13 illustrates the android implementation software that can simultaneously receive data from four LEDs. We received five bits of ID per LED and defined each combination of the received binary ID to a fixed location in the application system. The table in Figure 13 depicts the manner in which the location is assigned to different IDs. To receive multiple LEDs, the overall time for processing one frame should be within the critical frame time. Otherwise the application may unfortunately be stopped. The critical frame time is defined as the maximum processing time for one frame. In our system, we used 20 fps to limit the critical frame time to 50 msec. We add a starting symbol to recognize when the data is starting. So, the time to get the data obviously depends on the timing of getting the frame containing that symbol. We test in real-time debugging the software in android studio. We observe the time which is required for initialization, frame processing, demodulating, and device response. We figure out that almost

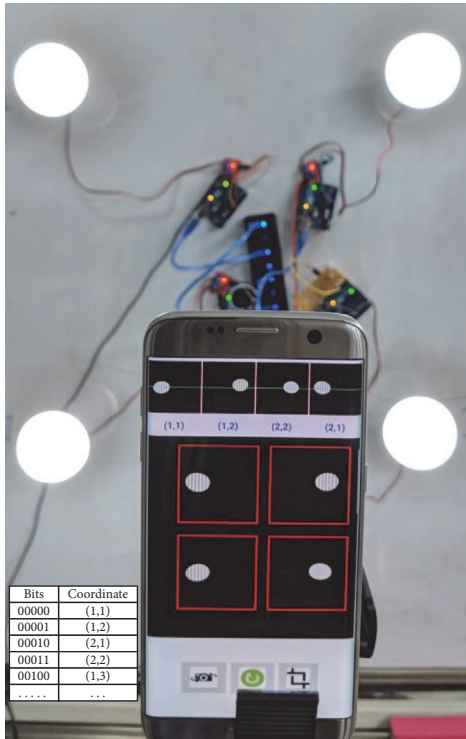


FIGURE 13: Implemented android application receiving multiple LEDs ID simultaneously.

1000 ms is required to debug and getting device response when communicating with 4 LEDs simultaneously. As each LED is transmitting 10 bits, we got data at 40 bps rate for 4 LEDs with this device.

8. Conclusion

This work focuses on the reception of data from multiple indoor LED transmitters as well as on the localization and navigation of the MR, processing the received data. The indoor LED locations are received as binary data of five bits per link at a data rate of 40 bps. The proposed algorithm was implemented in an indoor platform where four LEDs having sizes of 71 cm² were kept at a distance of 50 cm from each other. The four LEDs transmit four different IDs, and an android application that was developed to receive these IDs performed well simultaneously. We were able to communicate with the LEDs from a maximum distance of 480 cm. As our positioning approach requires measurement of the direct distance from the camera to the LED, we compare the accuracy of measuring the distance at different floor positions. Maintaining the floor height to be constant, we experience an increase in the percentage of error when the camera moves a long distance horizontally. To mitigate this error, we fix some recorded distance values within the application to compare. We have found maximum 2 cm error at 100 cm horizontal distance from the floor position of the target LED when the MR moves horizontally toward that LED. Thus, the accuracy is improved from the localization

and navigation viewpoint as well as based on the distance for indoor communication.

Data Availability

The data used to support the findings of this study are available from the corresponding author upon request.

Conflicts of Interest

The authors declare that they have no conflicts of interest.

Acknowledgments

This research was supported by the MSIT (Ministry of Science and ICT), Korea, under the Global IT Talent support program (IITP-2017-0-01806) supervised by the IITP (Institute for Information and Communication Technology Promotion) and the National Research Foundation of Korea (NRF) grant funded by the Korea government (Performance Enhancement and Resource Management of Visual MIMO-based Camera Communication Networks) (No. NRF-2016RID1A1A09919091).

References

- [1] M. Z. Chowdhury, M. T. Hossan, A. Islam, and Y. M. Jang, "A Comparative Survey of Optical Wireless Technologies: Architectures and Applications," *IEEE Access*, vol. 6, pp. 9819–9840, 2018.
- [2] M. T. Hossan, M. Z. Chowdhury, A. Islam, and Y. M. Jang, "A Novel Indoor Mobile Localization System Based on Optical Camera Communication," *Wireless Communications and Mobile Computing*, vol. 2018, 17 pages, 2018.
- [3] A. Khalajmehrabadi, N. Gatsis, and D. Akopian, "Modern WLAN Fingerprinting Indoor Positioning Methods and Deployment Challenges," *IEEE Communications Surveys & Tutorials*, vol. 19, no. 3, pp. 1974–2002, 2017.
- [4] E. Kupershtein, M. Wax, and I. Cohen, "Single-site emitter localization via multipath fingerprinting," *IEEE Transactions on Signal Processing*, vol. 61, no. 1, pp. 10–21, 2013.
- [5] P. Luo et al., "Experimental demonstration of RGB LED-based optical camera communications," *IEEE Photonics Journal*, vol. 7, no. 5, pp. 1–12, 2015.
- [6] R. D. Roberts, "Undersampled frequency shift ON-OFF keying (UFSSOOK) for camera communications (CamCom)," in *Proceedings of the 22nd Wireless and Optical Communications Conference, WOCC 2013*, pp. 645–648, China, May 2013.
- [7] P. Luo, Z. Ghassemlooy, H. L. Minh, H. Tsai, and X. Tang, "Undersampled-PAM with subcarrier modulation for camera communications," in *Proceedings of the 20th Opto-Electronics and Communications Conference (OECC)*, pp. 1–3, Shanghai, China, 2015.
- [8] Y.-Y. Won, S.-H. Yang, D.-H. Kim, and S.-K. Han, "Three-dimensional optical wireless indoor positioning system using location code map based on power distribution of visible light emitting diode," *IET Optoelectronics*, vol. 7, no. 3, pp. 77–83, 2013.
- [9] C. Yang and H.-R. Shao, "WiFi-based indoor positioning," *IEEE Communications Magazine*, vol. 53, no. 3, pp. 150–157, 2015.

- [10] R. Xu, W. Chen, Y. Xu, and S. Ji, "A New Indoor Positioning System Architecture Using GPS Signals," *Sensors*, vol. 15, no. 5, pp. 10074–10087, 2015.
- [11] Z. Zhou, M. Kavehrad, and P. Deng, "Indoor positioning algorithm using light-emitting diode visible light communications," *Optical Engineering*, vol. 51, no. 8, 2012.
- [12] W. Zhang, M. I. S. Chowdhury, and M. Kavehrad, "Asynchronous indoor positioning system based on visible light communications," *Optical Engineering*, vol. 53, no. 4, Article ID 045105, 2014.
- [13] S.-Y. Jung, S. Hann, S. Park, and C.-S. Park, "Optical wireless indoor positioning system using light emitting diode ceiling lights," *Microwave and Optical Technology Letters*, vol. 54, no. 7, pp. 1622–1626, 2012.
- [14] H.-S. Kim, D.-R. Kim, S.-H. Yang, Y.-H. Son, and S.-K. Han, "An indoor visible light communication positioning system using a RF carrier allocation technique," *Journal of Lightwave Technology*, vol. 31, no. 1, pp. 134–144, 2013.
- [15] K. Panta and J. Armstrong, "Indoor localisation using white LEDs," *IEEE Electronics Letters*, vol. 48, no. 4, pp. 228–230, 2012.
- [16] A. D. Cheok and L. Yue, "A novel light-sensor-based information transmission system for indoor positioning and navigation," *IEEE Transactions on Instrumentation and Measurement*, vol. 60, no. 1, pp. 290–299, 2011.
- [17] M. Nakajima and S. Haruyama, "New indoor navigation system for visually impaired people using visible light communication," *EURASIP Journal on Wireless Communications and Networking*, vol. 2013, article 37, 2013.
- [18] H. Huang, A. Yang, L. Feng, G. Ni, and P. Guo, "Indoor Positioning Method Based on Metameric White Light Sources and Subpixels on a Color Image Sensor," *IEEE Photonics Journal*, vol. 8, no. 6, 2016.
- [19] M. S. Hossen, Y. Park, and K. Kim, "Performance improvement of indoor positioning using light-emitting diodes and an image sensor for light-emitting diode communication," *Optical Engineering*, vol. 54, no. 3, pp. 1–11, 2015.
- [20] M.-G. Moon, S.-I. Choi, J. Park, and J. Y. Kim, "Indoor positioning system using LED lights and a dual image sensor," *Journal of the Optical Society of Korea*, vol. 19, no. 6, pp. 586–591, 2015.
- [21] Y.-S. Kuo, P. Pannuto, K.-J. Hsiao, and P. Dutta, "Luxapose: Indoor positioning with mobile phones and visible light," in *Proceedings of the 20th ACM Annual International Conference on Mobile Computing and Networking, MobiCom 2014*, pp. 447–458, USA, September 2014.
- [22] P. Huynh and M. Yoo, "VLC-based positioning system for an indoor environment using an image sensor and an accelerometer sensor," *Sensors*, vol. 16, no. 6, 2016.
- [23] H. Steendam, T. Q. Wang, and J. Armstrong, "Theoretical lower bound for indoor visible light positioning using received signal strength measurements and an aperture-based receiver," *Journal of Lightwave Technology*, vol. 35, no. 2, pp. 309–319, 2017.
- [24] F. Yin, Y. Zhao, F. Gunnarsson, and F. Gustafsson, "Received-signal-strength threshold optimization using Gaussian processes," *IEEE Transactions on Signal Processing*, vol. 65, no. 8, pp. 2164–2177, 2017.
- [25] X. Piao, Y. Zhang, T. Li et al., "RSS fingerprint based indoor localization using sparse representation with spatio-temporal constraint," *Sensors*, vol. 16, no. 11, 2016.
- [26] C. Feng, W. S. A. Au, S. Valaee, and Z. Tan, "Received-signal-strength-based indoor positioning using compressive sensing," *IEEE Transactions on Mobile Computing*, vol. 11, no. 12, pp. 1983–1993, 2012.
- [27] W. Gu, W. Zhang, M. Kavehrad, and L. Feng, "Three-dimensional light positioning algorithm with filtering techniques for indoor environments," *Optical Engineering*, vol. 53, no. 10, 2014.
- [28] S.-H. Yang, E.-M. Jung, and S.-K. Han, "Indoor location estimation based on LED visible light communication using multiple optical receivers," *IEEE Communications Letters*, vol. 17, no. 9, pp. 1834–1837, 2013.
- [29] F. I. K. Mousa, H. Le-Minh, Z. Ghassemlooy et al., "Indoor localization system utilizing two visible light emitting diodes," *Optical Engineering*, vol. 55, no. 11, 2016.
- [30] K. Wang, A. Nirmalathas, C. Lim, K. Alameh, and E. Skafidas, "Optical wireless-based indoor localization system employing a single-channel imaging receiver," *Journal of Lightwave Technology*, vol. 34, no. 4, pp. 1141–1149, 2016.
- [31] S.-H. Jung, B.-C. Moon, and D. Han, "Unsupervised learning for crowdsourced indoor localization in wireless networks," *IEEE Transactions on Mobile Computing*, vol. 15, no. 11, pp. 2892–2906, 2016.
- [32] X. Wang, L. Gao, S. Mao, and S. Pandey, "CSI-Based Fingerprinting for Indoor Localization: A Deep Learning Approach," *IEEE Transactions on Vehicular Technology*, vol. 66, no. 1, pp. 763–776, 2017.
- [33] Y. Hu and G. Leus, "Robust differential received signal strength-based localization," *IEEE Transactions on Signal Processing*, vol. 65, no. 12, pp. 3261–3276, 2017.
- [34] T.-H. Do and M. Yoo, "TDOA-based indoor positioning using visible light," *Photonic Network Communications*, vol. 27, no. 2, pp. 80–88, 2014.
- [35] S.-Y. Jung, S. Hann, and C.-S. Park, "TDOA-based optical wireless indoor localization using LED ceiling lamps," *IEEE Transactions on Consumer Electronics*, vol. 57, no. 4, pp. 1592–1597, 2011.
- [36] U. Nadeem, N. U. Hassan, M. A. Pasha, and C. Yuen, "Highly accurate 3D wireless indoor positioning system using white LED lights," *IEEE Electronics Letters*, vol. 50, no. 11, pp. 828–830, 2014.
- [37] T. Q. Wang, Y. A. Sekercioglu, A. Neild, and J. Armstrong, "Position accuracy of time-of-arrival based ranging using visible light with application in indoor localization systems," *Journal of Lightwave Technology*, vol. 31, no. 20, pp. 3302–3308, 2013.
- [38] O. Ennasr, G. Xing, and X. Tan, "Distributed time-difference-of-arrival (TDOA)-based localization of a moving target," in *Proceedings of the 55th IEEE Conference on Decision and Control, CDC 2016*, pp. 2652–2658, USA, December 2016.
- [39] S. H. Yang, E. M. Jeong, and S. K. Han, "Indoor positioning based on received optical power difference by angle of arrival," *IEEE Electronics Letters*, vol. 50, no. 1, pp. 49–51, 2014.
- [40] A. Arafa, X. Jin, and R. Klukas, "Wireless indoor optical positioning with a differential photosensor," *IEEE Photonics Technology Letters*, vol. 24, no. 12, pp. 1027–1029, 2012.
- [41] M. T. Hossan, M. Z. Chowdhury, M. K. Hasan et al., "A New Vehicle Localization Scheme Based on Combined Optical Camera Communication and Photogrammetry," *Mobile Information Systems*, vol. 2018, Article ID 8501898, 14 pages, 2018.
- [42] S. M. Berman, D. S. Greenhouse, I. L. Bailey, R. D. Clear, and T. W. Raasch, "Human electroretinogram responses to video displays, fluorescent lighting, and other high frequency sources," *Optometry and Vision Science*, vol. 68, no. 8, pp. 645–662, 1991.

- [43] H.-Y. Lee, H.-M. Lin, Y.-L. Wei, H.-I. Wu, H.-M. Tsai, and K. C.-J. Lin, "RollingLight: Enabling line-of-sight light-to-camera communications," in *Proceedings of the 13th Annual International Conference on Mobile Systems, Applications, and Services, MobiSys 2015*, pp. 167–180, Italy, May 2015.
- [44] Z. Zhang, "A flexible new technique for camera calibration," *IEEE Transactions on Pattern Analysis and Machine Intelligence*, vol. 22, no. 11, pp. 1330–1334, 2000.
- [45] H. A. Martins, J. R. Birk, and R. B. Kelley, "Camera models based on data from two calibration planes," *Computer Graphics and Image Processing*, vol. 17, no. 2, pp. 173–180, 1981.
- [46] E. Arthurs and H. Dym, "On the Optimum Detection of Digital Signals in the Presence of White Gaussian Noise—A Geometric Interpretation and a Study of Three Basic Data Transmission Systems," *IRE Transactions on Communications Systems*, vol. 10, no. 4, pp. 336–372, 1962.

Research Article

Threshold Secret Sharing Transmission against Passive Eavesdropping in MIMO Wireless Networks

Jungho Myung,¹ Keunyoung Kim,¹ and Taehong Kim ²

¹Electronics and Telecommunications Research Institute (ETRI), Republic of Korea

²School of Information and Communication Engineering, Chungbuk National University, Republic of Korea

Correspondence should be addressed to Taehong Kim; taehongkim@cbnu.ac.kr

Received 31 July 2018; Revised 19 September 2018; Accepted 2 October 2018; Published 22 October 2018

Guest Editor: Phuc V. Trinh

Copyright © 2018 Jungho Myung et al. This is an open access article distributed under the Creative Commons Attribution License, which permits unrestricted use, distribution, and reproduction in any medium, provided the original work is properly cited.

We propose a threshold secret sharing scheme for secure communications in multiple input and multiple output wireless networks. In the proposed scheme, the base station divides the secret data into N_{min} parts using a polynomial of degree $T - 1$ ($T \leq N_{min}$) and transmits the divided data to the legitimate user by beamforming with multiple spatial dimensions. Then, at the user, the secret data can be reconstructed with a sufficient number ($\geq T$) of divided parts by using the Lagrange interpolating polynomial. However, it is difficult for the eavesdropper to correctly estimate the T parts due to the difference between the main channel with beamforming and the eavesdropping channel in the physical layer, which results in the failure of secret data reconstruction. The numerical results show that the eavesdropping probability of the proposed scheme is lower than those of conventional schemes. Moreover, we analyze the symbol-error-rate and show that the theoretical result is well aligned with simulation results.

1. Introduction

Recently, multiple input and multiple output (MIMO) wireless networks have attracted significant attention due to the potential performance improvements; they have been shown to lead to spatial multiplexing or diversity gain [1–5]. The spatial dimensions derived from multiple antennas have initiated many new transmission techniques utilizing space as a new resource other than frequency and time [3–5]. Among the conventional methods, maximum ratio transmission [3] is proposed, in which a single stream is sent for achieving full diversity gain from multiple spatial dimensions. In addition, for throughput enhancement, spatial multiplexing transmission has been proposed to transmit multiple streams simultaneously [4, 5]. However, most of existing works only focus on spatial dimensions by multiple antennas in order to maximize the spatial multiplexing gain or diversity gain without considering security.

Wireless transmission is inherently vulnerable to eavesdropping due to the broadcast nature of the wireless medium [6–12]. Although a large number of security measures—from wired equivalent privacy in the wireless link layer to transport

layer security in the application layer—have already been developed and widely deployed throughout network layers, the fact remains that it is these very measures that must now confront substantial challenges by attackers or eavesdroppers with immense computing resources acquirable from a cloud or bounded error quantum polynomial time algorithms leveraging quantum computers, to list just a few. As one of new attempts to overcome this problem, physical layer security (PLS) has been introduced to achieve fundamental secrecy in the sense that it does not rely on any intractability assumptions unlike cryptographic algorithms implemented in higher network layers. With a single antenna configuration, Wyner first introduced a wiretap channel and the associated secrecy, the results of which show the feasibility of ultimately secure communication [6]. However, there is a problem in that secrecy cannot be guaranteed if the gain of the eavesdropping channels is higher than the gain of the main channel, that is, the channel of the target user. To overcome this problem, PLS with multiple antennas has been proposed [8–12]. In MIMO wireless networks, by beamforming and jamming techniques, the secrecy can be provided even though the quality of the main channel is

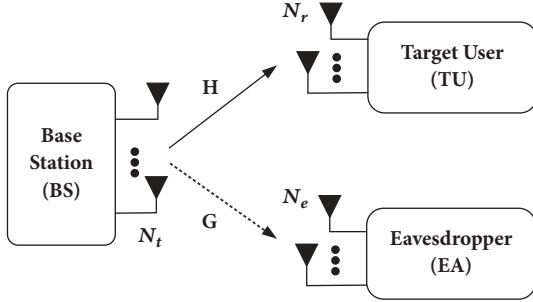


FIGURE 1: MIMO wireless networks with an eavesdropper.

worse than the quality of the eavesdropping channel. Most of existing works have only focused on increasing the secrecy rate by beamforming and jamming design, assuming that the transmitter knows the channel state information (CSI) of the eavesdropper. However, it is impossible to obtain the CSI of the eavesdropper due to the passive posture. Therefore, to ensure secrecy against passive eavesdropper, a new transmission technique with multiple spatial dimensions is needed on the condition that the transmitter cannot know the eavesdropping channels.

In this paper, we propose a threshold secret sharing transmission for secure communications in the absence of an eavesdropping channel information. In the proposed scheme, the secret data is divided into N_{min} parts using a polynomial of degree $T-1$ and then transmitted to the target user through multiple spatial dimensions by a transmit beamforming. At the user, based on the Lagrange interpolating polynomial, the secret data can be recovered when a sufficient number ($\geq T$) of the divided parts are combined together. We also propose the majority rule for secret reconstruction to overcome fading and noise impairments in wireless channels. At the point of the eavesdropper, it is difficult to correctly estimate the T parts due to the difference between main channel and eavesdropping channel in the physical layer. Therefore, attempt to reconstruct the secret data is unsuccessful. The numerical results show that the eavesdropping probability of the proposed approach is better than those of the conventional approaches. Also, we provide an analysis of SER for the proposed secret sharing scheme and verify that the proposed theoretically derived results well agree with the Monte-Carlo simulation results.

Notations. \mathbf{X}^T , \mathbf{X}^* , \mathbf{X}^\dagger , $\|\mathbf{X}\|$, and $\mathbf{E}[\cdot]$ denote the transpose, the conjugate transpose, the pseudo inverse, the Euclidean norm of matrix \mathbf{X} , and the expectation function, respectively.

2. System Model

As shown in Figure 1, we consider MIMO wireless networks with a base station (BS) with N_t transmit antennas, a target user (TU) with N_r receiving antennas, and an eavesdropper (EA) with N_e receive antennas. When BS transmits a secret data over the channel matrix \mathbf{H} to the TU, the radio signal is exposed to the EA over the cross channel \mathbf{G} . The channel coefficients are assumed to be mutually independent Rayleigh

flat fading with additive white Gaussian noise (AWGN) having zero mean and unit variance.

The received signal at the target user can be written as

$$\mathbf{y} = \mathbf{H}\mathbf{x} + \mathbf{n}, \quad (1)$$

where \mathbf{y} , \mathbf{x} , and \mathbf{n} denote the received signal vector, the transmitted signal vector, and the AWGN vector, respectively. Also, the eavesdropping signal can be written as

$$\mathbf{z} = \mathbf{G}\mathbf{x} + \mathbf{w}, \quad (2)$$

where \mathbf{z} and \mathbf{w} denote the received signal vector and the AWGN vector at the EA, respectively.

3. Threshold Secret Sharing Transmission in MIMO Wireless Networks

3.1. Threshold Secret Sharing Generator. Threshold secret sharing is a well-known scheme in cryptography introduced by Adi Shamir [13]. In the scheme, a secret data is divided into N parts by a polynomial of degree $T-1$. To reconstruct the secret data, a minimum number of parts (T) is required for solving the polynomial problem correctly. In the threshold scheme, this number is less than the total number of parts ($T \leq N$). Therefore, this is called the (T, N) -threshold secret sharing scheme [14–16].

For spectral efficiency and throughput enhancement in MIMO networks, a BS transmits independent and separately encoded signals, so-called streams, from each of the multiple transmit antennas. Considering our system model, the number of streams (that is, the spatial multiplexing order) can be obtained as

$$N_{min} = \min(N_t, N_r). \quad (3)$$

It means that there are N_{min} independent wireless paths between the BS and the TU by beamforming.

With multiple paths and the threshold scheme, the BS divides the secret data into N_{min} parts using a polynomial of degree $T-1$ ($T \leq N_{min}$). Then, the i th part with a polynomial can be calculated as

$$S_i = f(i) = (a_0 + a_1i + \dots + a_{T-1}i^{T-1}) \bmod p, \quad (4)$$

where coefficient a_0 is the original secret data while the other coefficients a_1, a_2, \dots, a_{T-1} are all randomly chosen at the BS. In addition, p , T , and \bmod denote a large prime number greater than any of the coefficients, a parameter controlling the balance between the symbol-error-rate (SER) and eavesdropping probability (EP), and the p -modulo operation, respectively. We assume that the value p and T are preshared with BS and TU.

For example, let us examine how the proposed scheme works in MIMO wireless networks with $N_t = N_r = 5$. In the given antenna configuration, the value of N_{min} is determined to be 5 by (3). Also, with preshared parameter (ex. $p = 17$ and $T = 3$), BS randomly chooses the remaining coefficients as a number smaller than p (ex. $a_1 = 4, a_2 = 2$). Then, S_i for secret data can be obtained as

$$S_i = f(i) = \underbrace{4}_{\text{secret data}} + 4i + 2i^2 \bmod 17, \quad (5)$$

and $S_1 = 10, S_2 = 3, S_3 = 0, S_4 = 1, S_5 = 6$.

The divided parts in (4) are modulated (ex. QPSK, QAM) and then the modulated signals are transmitted to the target user through spatial dimensions with the transmit beamforming matrix \mathbf{V} as

$$\mathbf{y} = \mathbf{H}\mathbf{V}\mathbf{x} + \mathbf{n}, \quad (6)$$

where $\mathbf{x} = [\widehat{S}_1, \widehat{S}_2, \dots, \widehat{S}_{N_{min}}]^T$ and \widehat{S}_i denotes the i -th modulated signal. Also, the eavesdropping signal with transmit beamforming is rewritten as

$$\mathbf{z} = \mathbf{G}\mathbf{V}\mathbf{x} + \mathbf{w}. \quad (7)$$

3.2. Spatial Dimension with Beamforming. For the design of an efficient transmit beamforming and receive combining efficiently, we assume that the perfect CSI of \mathbf{H} is available at the BS by channel reciprocity or feedback. If the BS also has the perfect CSI of the eavesdropping channel \mathbf{G} , a secure signal transmission can be possible using transmit beamforming (e.g., Zero-Forcing Beamforming) to nullify the eavesdropping channel. However, due to the passive characteristic of the EA, it is hard to obtain the eavesdropping CSI at the BS. Therefore, without any information about the eavesdropping channel, transmit beamforming is generally designed for maximizing the spectral efficiency or improving the reliability of the target user.

With the perfect CSI of \mathbf{H} , the spatial dimensions in the MIMO networks are obtained by singular value decomposition (SVD). The channel \mathbf{H} can be decomposed to $\mathbf{U}\mathbf{D}\mathbf{V}^*$ by using SVD, where $\mathbf{U} \in \mathbb{C}^{N_r \times N_r}$, $\mathbf{V} \in \mathbb{C}^{N_t \times N_t}$ are unitary matrices, and $\mathbf{D} \in \mathbb{C}^{N_r \times N_t}$ is a diagonal matrix whose nonzero entries $\sqrt{\lambda_i}$ are the square roots of the eigenvalues of $\mathbf{H}^*\mathbf{H}$. With the transmit beamforming matrix \mathbf{V} and the receive combining matrix \mathbf{U}^* , the combined signal at the target user can be rewritten as

$$\mathbf{U}^* \cdot \mathbf{y} = \underbrace{\mathbf{U}^* \cdot \mathbf{U}}_{\mathbf{I}} \cdot \underbrace{\mathbf{D}\mathbf{V}^* \cdot \mathbf{V}}_{\mathbf{I}} \cdot \mathbf{x} + \mathbf{U}^* \cdot \mathbf{n}, \quad (8)$$

$$\tilde{\mathbf{y}} = \mathbf{D}\mathbf{x} + \tilde{\mathbf{n}}.$$

Since \mathbf{U} is a unitary matrix, the noise vectors $\tilde{\mathbf{n}}$ and \mathbf{n} have the same distribution. Then, the i -th signal of $\tilde{\mathbf{y}}$ can be obtained as

$$\tilde{y}_i = \sqrt{\lambda_i}x_i + \tilde{n}_i, \quad i = 1, \dots, N_{min}. \quad (9)$$

3.3. Reconstruction of the Secret. With the receive combining matrix \mathbf{U}^* and the channel compensation of the received signals, the demodulated data $[\widehat{S}_1, \widehat{S}_2, \dots, \widehat{S}_{N_{min}}]$ can be obtained at the target user. Then, the target user with N_{min} demodulated data randomly chooses a subset composed of T data (ex. $[\widehat{S}_1, \widehat{S}_2, \dots, \widehat{S}_T]$) and estimates the Lagrange interpolating polynomial as

$$\widehat{f}(i) = \sum_{j=1}^T \widehat{S}_j \cdot \left[\prod_{k=1, k \neq j}^T \frac{i - i_k}{i_j - i_k} \right] \bmod p, \quad (10)$$

where i_j, i_k means the index parameter of a subset. Then, the secret data can be obtained by $\widehat{f}(0) = \widehat{K}$. For example, with

$N_{min} = 5, T = 3, p = 17$, and the demodulated data $\widehat{S}_1 = 10, \widehat{S}_2 = 3, \widehat{S}_4 = 1$, and the secret data and a polynomial of degree $T - 1$ can be reconstructed by (10) as

$$\begin{aligned} \widehat{f}(i) &= \sum_{j=1}^3 \widehat{S}_j \cdot \left[\prod_{k=1, k \neq j}^3 \frac{i - i_k}{i_j - i_k} \right] \bmod 17, \\ &= \left(10 \cdot \frac{i-2}{1-2} \cdot \frac{i-4}{1-4} + 3 \cdot \frac{i-1}{2-1} \cdot \frac{i-4}{2-4} + 1 \cdot \frac{i-1}{4-1} \right. \\ &\quad \left. \cdot \frac{i-2}{4-2} \right) \bmod 17, \\ &= (21 - 13i + 2i^2) \bmod 17 = \underbrace{4}_{\text{secret data}} + 4i + 2i^2. \end{aligned} \quad (11)$$

However, since modulated signals are transmitted with fading channel and noise in MIMO wireless networks, the reconstruction of the secret must consider the demodulation error. In other words, the derived result in (10) can change depending on which subset a user chooses. Considering the proposed secret sharing scheme, the number of the subset (N_s) is

$$N_s = \mathbf{C} \left(\begin{matrix} N_{min} \\ T \end{matrix} \right), \quad (12)$$

where $\mathbf{C} \left(\begin{matrix} a \\ b \end{matrix} \right)$ denotes the number of possible combinations of b objects from a set of a objects. Then, a set (\mathcal{U}) of the estimated secret data \widehat{K} from (10) and (12) is obtained as

$$\mathcal{U} = \{ \widehat{K}_1, \widehat{K}_2, \dots, \widehat{K}_{N_s} \}, \quad (13)$$

and the secret data is finally determined by majority rule of \mathcal{U} to reduce the effect of the demodulation error. Figure 2 shows a simplified block diagram of the proposed threshold secret sharing system in MIMO wireless networks.

3.4. Performance Analysis. In this subsection, we provide an analysis of SER to show how SER is affected by T, N_{min} , and signal-to-noise ratio (SNR). In our MIMO networks, the i -th modulated signal \widehat{S}_i is transmitted to the user through the i -th spatial dimension in (9) by beamforming technique in Section 3.2. To find the distribution of the i -th eigenvalue, the joint probability density function (E_{JPDF}) of the N_{min} -eigenvalues of Wishart matrices, $\lambda_1 \geq \lambda_2 \geq \dots \geq \lambda_{N_{min}} \geq 0$, is defined [17] as

$$\begin{aligned} E_{JPDF} &= \frac{1}{K_{m,n}} e^{-(1/2) \sum_{i=1}^{N_{min}} \lambda_i} \prod_{i=1}^{N_{min}} \lambda_i^{(1/2)(N_{max} - N_{min} - 1)} \\ &\quad \cdot \prod_{i < j} (\lambda_i - \lambda_j) d\lambda_1 \cdots d\lambda_{N_{min}}, \end{aligned} \quad (14)$$

where

$$\begin{aligned} K_{m,n} &= \left(\frac{2^{N_{max}}}{\pi} \right)^{N_{min}/2} \\ &\quad \cdot \prod_{i=1}^{N_{min}} \Gamma \left(\frac{N_{max} - i + 1}{2} \right) \Gamma \left(\frac{N_{min} - i + 1}{2} \right), \end{aligned} \quad (15)$$

$$N_{max} = \max(N_t, N_r).$$

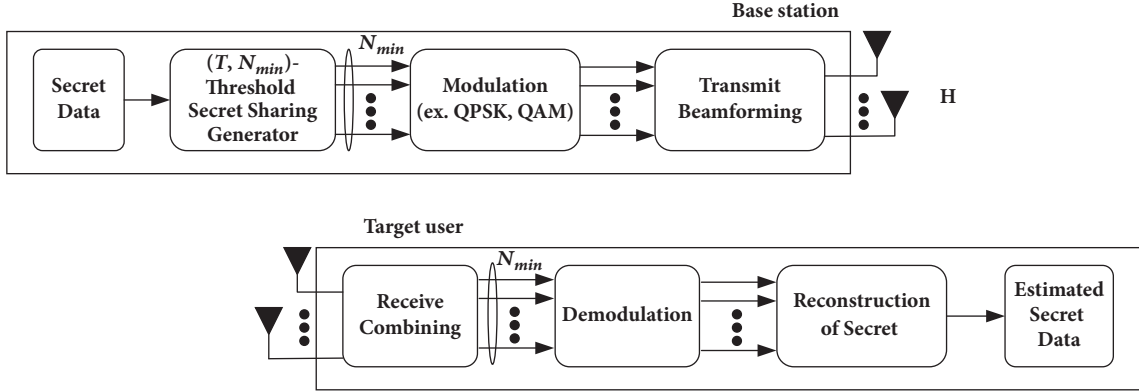


FIGURE 2: A simplified block diagram of the proposed threshold secret sharing system in MIMO wireless networks.

Then, the density of the i -th eigenvalue can be obtained by integrating (14) as

$$E_{PDF}^i = \int_{R_+^{N_{min}-1}} E_{JPDF} d\Omega, \quad (16)$$

where $d\Omega = d\lambda_1 \cdots d\lambda_{i+1} d\lambda_{i-1} \cdots d\lambda_{N_{min}}$ and the integration takes place over the positive orthant, $R_+^{N_{min}-1} = \{(\lambda_1, \dots, \lambda_{i+1}, \lambda_{i-1}, \dots, \lambda_{N_{min}}) : \lambda \geq 0\}$.

Also, if $\log_2 M$ is even integer, SER of M -QAM in AWGN channel can be defined [18] as $P_{SER} = 1 - (1 - p)^2$ with

$$p = \left(1 - \frac{1}{\sqrt{M}}\right) \operatorname{erfc} \left(\sqrt{\frac{3}{2(M-1)} \frac{E_s}{N_o}} \right), \quad (17)$$

where

$$\operatorname{erfc}(x) = \frac{2}{\sqrt{\pi}} \int_x^\infty e^{-t^2} dt, \quad (18)$$

and E_s/N_o means the signal-to-noise ratio. Then, SER of M -QAM in fading channel can be obtained as

$$P_s = 2E[p] - E[p^2]. \quad (19)$$

Also, with N_{min} spatial dimensions in our MIMO network, SER of the i -th dimension is rewritten as

$$P_s^i = 2E_i[p] - E_i[p^2], \quad (20)$$

where

$$\begin{aligned} E_i[p] &= \int_0^\infty \bar{p} \cdot E_{PDF}^i d\lambda_i, \\ E_i[p^2] &= \int_0^\infty \bar{p}^2 \cdot E_{PDF}^i d\lambda_i, \end{aligned} \quad (21)$$

$$\bar{p} = \left(1 - \frac{1}{\sqrt{M}}\right) \operatorname{erfc} \left(\sqrt{\frac{3\lambda_i}{2(M-1)} \frac{E_s}{N_o}} \right).$$

Since we cannot find any closed-form expression in our best knowledge, P_s^i needs to be calculated by numerically integrating (21). Then, based on the majority rule in

Section 3.3, SER of the proposed threshold sharing scheme can be obtained by (10) and (20) as

$$P_s = 1 - \sum_{\text{sum}(\mathbf{k}) \leq N_{min} - T - 1} \prod_{i=1}^{N_{min}} (P_s^i)^{k_i} \cdot (1 - P_s^i)^{1 - k_i}, \quad (22)$$

where

$$\mathbf{k} = \{k_1, \dots, k_i, \dots, k_{N_{min}}\},$$

$$\text{sum}(\mathbf{k}) = \sum_{i=1}^{N_{min}} k_i, \quad k_i \in \{0, 1\}. \quad (23)$$

4. Eavesdropper Behavior

In this section, we explain the eavesdropper's behavior against the threshold secret sharing system.

4.1. With only \mathbf{G} . If EA is a legitimate user and an internal eavesdropper in wireless network, EA can easily obtain the channel state information of \mathbf{G} by channel estimation using pilot and preamble signals of BS [19]. With only information \mathbf{G} , the eavesdropping signal in (7) is combined by the receive combining matrix \mathbf{U}_e^G to eliminate interference caused by channel \mathbf{G} as

$$\begin{aligned} \mathbf{U}_e^G \cdot \mathbf{z} &= \mathbf{U}_e^G \cdot \mathbf{G}\mathbf{V}\mathbf{x} + \mathbf{U}_e^G \cdot \mathbf{w} \\ &= \tilde{\mathbf{V}}\mathbf{x} + \tilde{\mathbf{w}}^G, \end{aligned} \quad (24)$$

where

$$\mathbf{U}_e^G = \frac{\mathbf{G}^\dagger}{\|\mathbf{G}\|}. \quad (25)$$

In this case, since there is no information of the transmit beamforming matrix \mathbf{V} and the eavesdropper fails to decode the received signal correctly, except for the transmit beamforming matrix $\mathbf{V} = \mathbf{I}$.

4.2. With \mathbf{G} and \mathbf{H} . For efficient eavesdropping, channel information about \mathbf{H} and \mathbf{G} is needed at the EA. First,

based on the channel estimation technique, EA knows \mathbf{G} . We also assumed that smart EA can be obtained \mathbf{H} and p by eavesdropping the TU's channel feedback and the exchanged information for secure data transmission.

Then, with the channel information of \mathbf{H} , EA predicts \mathbf{V} for the target user by SVD of \mathbf{H} . Therefore, for efficient eavesdropping, the eavesdropping signal can be combined by the receive matrix \mathbf{U}_e^{GH} considering channel compensation as

$$\begin{aligned} \mathbf{U}_e^{\text{GH}} \cdot \mathbf{z} &= \mathbf{U}_e^{\text{GH}} \cdot \mathbf{G}\mathbf{V}\mathbf{x} + \mathbf{U}_e^{\text{GH}} \cdot \mathbf{w} \\ &= \tilde{\mathbf{D}}_e \mathbf{x} + \tilde{\mathbf{w}}, \end{aligned} \quad (26)$$

where

$$\mathbf{U}_e^{\text{GH}} = \frac{(\mathbf{G} \cdot \mathbf{V})^\dagger}{\|\mathbf{G} \cdot \mathbf{V}\|}, \quad (27)$$

and $\tilde{\mathbf{D}}_e$ denotes the diagonal matrix through the inverse matrix operation. Then, the transmitted data are estimated by the compensation of $\tilde{\mathbf{D}}_e$. Finally, the secret data can be obtained through the same procedure as that of the secret reconstruction described in Section 3.3.

5. Numerical Results

In this section, we provide the simulation results of the symbol-error-rate (SER) and the eavesdropping probability of the proposed scheme. For simulation, MIMO wireless channels are considered as shown in Figure 1, where the channel coefficients are assumed to be flat Rayleigh fading with mutually independent and additive white Gaussian noise terms having zero mean and equivalent variance $\mathcal{CN}(0, \sigma^2)$. We compare the (T, N_{\min}) -threshold secret sharing scheme (TS- (T, N_{\min})) with spatial multiplexing transmission (SM) and diversity transmission (Div). In SM, for full multiplexing gain, we assumed that the BS transmits N_{\min} independent data to the TU by beamforming. Therefore, an instantaneous EP at the EA is defined by N_{sm} over N_{\min} , where N_{sm} is the number of successfully decoded data. Also, since a single data transmission is assumed for full diversity gain in Div, an instantaneous EP is defined by eavesdropping success (1) or failure (0). The specific parameters are indicated at each figure.

In Figure 3, SER versus SNR at the TU is evaluated for different approaches. With full diversity gain, Div shows the best SER performance. On the other hand, SM shows the worst SER performance, because N_{\min} stream is simultaneously transmitted through spatial dimensions with an equal transmit power constraint. In general, we can see that TS achieves better performance than SM. In the high SNR region in particular, it achieves the diversity gain as Div because the TS can recover the secret data by majority rule, even though there are some miss-decoded parts due to the low eigenvalues in (9). On the contrary, in a low SNR region, due to the error propagation of majority rule, the TS shows the worst SER performance. In addition, through the slope of the graph, we can see that SER performance is determined by a gap between T and N_{\min} . With the fixed N_{\min} , the performance of the TS

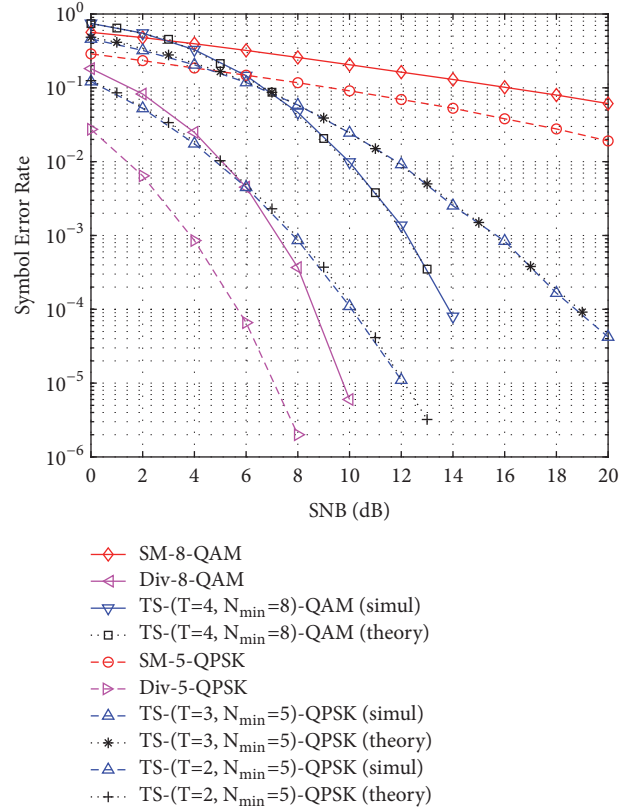


FIGURE 3: Symbol error rate vs. SNR (dB) at the target user, where $N_t = N_r = \{8, 5\}$ and $T = \{4, 3, 2\}$.

approaches that of the SM as T approaches to N_{\min} , because the secret data can be reconstructed only when all parts are successfully decoded to solve the polynomial. In addition, if T approaches 1, the performance of the TS approaches that of Div, because the secret data can be easily obtained by solving the polynomial with a small number of parts. It is noticeable that the theoretically derived result in Section 3.4 is well matched with simulation results.

In Figure 4, we evaluate the performance of EP at the eavesdropper under different SNR. With full diversity gain, Div shows the most vulnerable performance to eavesdropping. On the other hand, the proposed TS shows good performance against eavesdropping compared to SM and Div, especially in the low SNR region. If only \mathbf{G} is available, the eavesdropping fails due to the intersymbol interference caused by beamforming matrix \mathbf{V} . Even though the smart EA has the perfect CSIs of both \mathbf{G} and \mathbf{H} , it is hard to estimate the sufficient number ($\geq T$) of parts correctly, and it fails to reconstruct the secret data because the gain of the effective eavesdropping channel $\mathbf{G}\mathbf{V}$ is degraded compared to the gain of the effective main channel $\mathbf{H}\mathbf{V}$ in physical layer. We can also see that EP is determined by the threshold value. When the threshold value is set to be N_{\min} , the most secure communication against eavesdropping is possible. Therefore, an appropriate threshold value should be set according to the user's purpose because there is a performance trade-off between SER and DP depending on the threshold value.

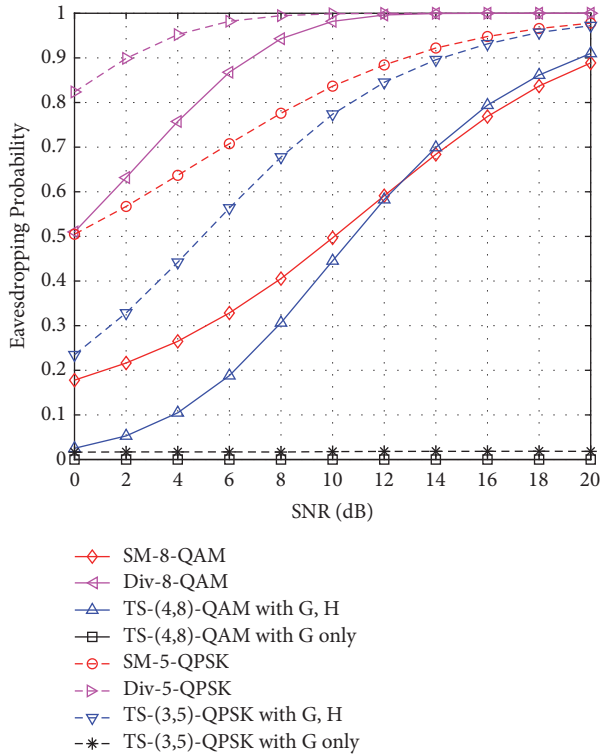


FIGURE 4: Eavesdropping probability vs. SNR(dB) at the eavesdropper, where $N_t = N_r = N_e = \{8, 5\}$ and $T = \{4, 3\}$.

6. Conclusion

In this paper, we considered a threshold secret sharing to enhance physical layer security against an eavesdropper. In the proposed scheme, with N_{min} spatial dimensions by beamforming, the secret data is divided into N_{min} parts using a unique polynomial of degree $T - 1$ and then transmitted to the user. Then, the user can reconstruct the secret data with a sufficient number ($\geq T$) of parts by using the Lagrange interpolating polynomial. However, at the eavesdropper, the reconstruction of secret data fails due to the difference between the main channel and the eavesdropping channel in the physical layer. The simulation shows that the eavesdropping probability of the proposed scheme is better than those of the conventional approaches. Moreover, we found that the threshold value plays an important role in our scheme. Therefore, in the future, we would like to extend our current scheme with a fixed threshold value to a dynamic scheme where the base station can determine their own threshold value to simultaneously maximize the user's symbol error rate and to minimize the eavesdropping probability with imperfect CSI.

Data Availability

The data used to support the findings of this study are included within the article.

Disclosure

A preliminary version of this paper was presented at International Conference on Ubiquitous and Future Networks (ICUFN), Czech Republic, July 2018 [20].

Conflicts of Interest

The authors declare that they have no conflicts of interest.

Authors' Contributions

T. Kim is the corresponding author of this paper.

Acknowledgments

This research was partially supported by Basic Science Research Program through the National Research Foundation of Korea (NRF) funded by the Ministry of Education (2016R1D1A1B03933007) and Electronics and Telecommunications Research Institute (ETRI) grant funded by the Korean government (18ZF1100, Wireless Transmission Technology in Multi-point to Multipoint Communications).

References

- [1] M. H. M. Costa, "Writing on dirty paper," *IEEE Transactions on Information Theory*, vol. 29, no. 3, pp. 439–441, 1983.
- [2] G. J. Foschini and M. J. Gans, "On limits of wireless communications in a fading environment when using multiple antennas," *Wireless Personal Communications*, vol. 6, no. 3, pp. 311–335, 1998.
- [3] T. K. Y. Lo, "Maximum ratio transmission," *IEEE Transactions on Communications*, vol. 47, no. 10, pp. 1458–1461, 1999.
- [4] P. W. Wolniansky, G. J. Foschini, G. D. Golden, and R. A. Valenzuela, "V-BLAST: an architecture for realizing very high data rates over the rich-scattering wireless channel," in *Proceedings of the URSI International Symposium on Signals, Systems, and Electronics (ISSSE '98)*, pp. 295–300, IEEE, Pisa, Italy, September–October 1998.
- [5] Q. H. Spencer, A. L. Swindlehurst, and M. Haardt, "Zero-forcing methods for downlink spatial multiplexing in multiuser MIMO channels," *IEEE Transactions on Signal Processing*, vol. 52, no. 2, pp. 461–471, 2004.
- [6] A. D. Wyner, "The wire-tap channel," *Bell Labs Technical Journal*, vol. 54, no. 8, pp. 1355–1387, 1975.
- [7] A. Khisti, A. Tchamkerten, and G. W. Wornell, "Secure broadcasting over fading channels," *Institute of Electrical and Electronics Engineers Transactions on Information Theory*, vol. 54, no. 6, pp. 2453–2469, 2008.
- [8] E. G. Larsson and E. A. Jorswieck, "Competition versus cooperation on the MISO interference channel," *IEEE Journal on Selected Areas in Communications*, vol. 26, no. 7, pp. 1059–1069, 2008.
- [9] R. Liu and H. V. Poor, "Secrecy capacity region of a multiple-antenna Gaussian broadcast channel with confidential messages," *Institute of Electrical and Electronics Engineers Transactions on Information Theory*, vol. 55, no. 3, pp. 1235–1249, 2009.
- [10] T. Liu and S. Shamai, "A note on the secrecy capacity of the multiple-antenna wiretap channel," *IEEE Transactions on Information Theory*, vol. 55, no. 6, pp. 2547–2553, 2009.

- [11] F. Oggier and B. Hassibi, "The secrecy capacity of the MIMO wiretap channel," *IEEE Transactions on Information Theory*, vol. 57, no. 8, pp. 4961–4972, 2011.
- [12] J. Myung, H. Heo, and J. Park, "Joint beamforming and jamming for physical layer security," *ETRI Journal*, vol. 37, no. 5, pp. 898–905, 2015.
- [13] A. Shamir, "How to share a secret," *Communications of the ACM*, vol. 22, no. 11, pp. 612–613, 1979.
- [14] C.-C. Yang, T.-Y. Chang, and M.-S. Hwang, "A (t, n) multi-secret sharing scheme," *Applied Mathematics and Computation*, vol. 151, no. 2, pp. 483–490, 2004.
- [15] C.-W. Chan and C.-C. Chang, "A scheme for threshold multi-secret sharing," *Applied Mathematics and Computation*, vol. 166, no. 1, pp. 1–14, 2005.
- [16] L.-J. Pang and Y.-M. Wang, "A new (t, n) multi-secret sharing scheme based on Shamir's secret sharing," *Applied Mathematics and Computation*, vol. 167, no. 2, pp. 840–848, 2005.
- [17] R. J. Muirhead, *Aspects of Multivariate Statistical Theory*, John Wiley & Sons, New York, NY, USA, 1982.
- [18] M. K. Simon and M. Alouini, *Digital Communication Over Fading Channels*, John Wiley & Sons, Inc., New York, USA, 2000.
- [19] B. He and X. Zhou, "Secure On-Off transmission design with channel estimation errors," *IEEE Transactions on Information Forensics and Security*, vol. 8, no. 12, pp. 1923–1936, 2013.
- [20] J. Myung and T. Kim, "Threshold Secret Sharing Transmission Against Passive Eavesdropping in MIMO Wireless Network," in *Proceedings of the 2018 Tenth International Conference on Ubiquitous and Future Networks (ICUFN)*, pp. 634–636, Prague, Czech Republic, July 2018.

Research Article

Network-Assisted Optimal Datalink Selection Scheme for Heterogeneous Aeronautical Network

Dongli Wang ¹, Guoce Huang,² Shufu Dong,² Yequn Wang,² Jian Liu,² and Weiting Gao²

¹Graduate College, Air Force Engineering University, Xi'an 710051, China

²Information and Navigation College, Air Force Engineering University, Xi'an 710077, China

Correspondence should be addressed to Dongli Wang; wdl4178@163.com

Received 23 July 2018; Revised 9 September 2018; Accepted 13 September 2018; Published 16 October 2018

Guest Editor: Phuc V. Trinh

Copyright © 2018 Dongli Wang et al. This is an open access article distributed under the Creative Commons Attribution License, which permits unrestricted use, distribution, and reproduction in any medium, provided the original work is properly cited.

Currently, the existing datalink selection algorithms in heterogeneous aeronautical network unilaterally focus on the user side or network side and lack the two sides' cooperation, which seriously affects the utilization of available datalinks. Firstly, to reflect the user-side requirements and network-side load, we propose a user-centric datalink selection scheme combing the user-side multiattribute utility and the network-side access rate for single-user selection. It can be established as a multiobjective optimization problem and solved by the selected optimal datalink. Secondly, for multiuser datalink selection, in order to guarantee the access requests of multiple users, the central control mode of Software Define Networking (SDN) is used to assist the user to perform datalink selection on the network side. By constructing multiuser multiobjective optimization problem, a priority distinction selection (PDS) algorithm is proposed to maximize the number of users accessing their optimal datalinks and minimize the modification of the users' access request. Finally, the proposed user-side datalink selection scheme and network-side assisted selection algorithm are simulated to verify the feasibility and effectiveness.

1. Introduction

In the field of aeronautical communications, with the anticipated increase in the number of aircraft [1], the communication demands have shown exponential growth in numerous applications, such as air traffic control (ATC) for manned aircraft [2], communication and surveillance for unmanned aerial vehicles (UAVs) [3–5], and the cooperative systems of manned-unmanned aerial vehicles [6]. In all of these applications, a great mass of heterogeneous information with different criticality levels needs to be transmitted over the datalinks. However, it is impractical to use a single datalink to meet all requirements in air-to-air and air-to-ground communications [7]. Different datalinks have obvious differences in their technical indicators, usage costs, and potential risks and are applicable to diverse scenarios. Due to the diversity of aircraft and the specificity of the terrestrial networks corresponding to different links, the aeronautical network composed of aircraft, transmission links, and terrestrial access networks exhibits apparent heterogeneity, which is

more complexity than the homogeneous network. However, the convergence of multiple heterogeneous transmission links can extend system capacity and utilize heterogeneous resources efficiently, which is unrealizable for a single link. Therefore, by integrating multiple Radio Access Technologies (RATs), Next Generation Air Transportation System (NextGen) [8] and Signal European Sky for ATM Research (SESAR) [9] conduct researches on heterogeneous aeronautical communication systems including NEWSKY (NEtWORKing the SKY) [10] and SANDRA (Seamless Aeronautical Networking through integration of Data links, Radios, and Antennas) [11], which have achieved significant progress. The heterogeneous aeronautical communication system constructs the network architecture by the airborne segment, the link segment and the ground segment. It introduces the Multilink Operational Concept (MLOC) on the link segment and isolates the applications from different RATs on the airborne segment. Combined with the construction of the heterogeneous aeronautical network on the ground segment, it is possible to integrate the future datalinks such as L-band

Digital Aeronautical Communications System (LDACS) [12] and Aeronautical Mobile Airport Communications System (AeroMACS) [13] and to be compatible with the original technologies, such as very high frequency (VHF) digital link mode 2 (VDL 2) [14].

The aircraft generally has multilink configuration and multihoming capabilities to ensure flight safety and reliability of information transmission. In the scenario where multiple links are available, suitable datalink selection is needed to maintain seamless communications [15]. As we know, there are four main reasons for triggering the aircraft to select datalink [16]: (1) changes in the flight phase of the aircraft lead to changes in available links, (2) arrival of new or handover services, (3) dynamic changes of user-side attributes or network-side properties, and (4) changes in user or operator preferences. The usual datalink selection algorithm is based on a preset priority. For example, the VHF link has the highest priority, followed by the satellite link and High Frequency (HF) link. This method does not consider the attributes of the services and easily causes the network congestion, long access time, and unguaranteed communication effect. In addition, the baseline link selection algorithm used in SANDRA is also one of the commonly used methods [17]. It selects available links according to a single attribute. This algorithm is too simple to consider user preference and multiple attributes, so the selected datalink is not optimal. Compared with single-attribute link selection, the multiattribute link selection method considers multiple factors and has a better user experience. The optimal datalink selection algorithm proposed by ALAM et al. utilizes the multiple attribute decision making (MADM) method to consider user preference, and has remarkable flexibility [17].

The existing datalink selection algorithms in heterogeneous aeronautical network unilaterally focus on the user side or network side, and usually use user-side attributes and preferences as the basis for datalink selection instead of network-side dynamic attributes. Considering the wide coverage of aeronautical links, such as the Iridium beam footprint with a diameter of approximately 550 kilometres [18] and the maximum transmission range of 200 nautical miles of LDACS, it is more than one aircraft in the overlay airspace as shown in Figure 1. Simultaneously, multiple aircraft are likely to perform datalink selection due to their high-speed mobility. If plenty of aircraft select the same datalink, the access network will be congested with excessive load. So it is necessary to estimate the network-side load to guide the link selection on the user side. Moreover, according to the limited resources of the heterogeneous network and the different available datalinks of each user, we should consider that how to maximize the protection of the user-side access requests with multiuser access and network-side assistance.

In this paper, we propose a network-assisted optimal datalink selection scheme for the heterogeneous aeronautical network. Firstly, for single-user selection a multiattribute utility function is constructed according to the user-side requirements, and the access rate is measured to present the network-side load. The multiobjective optimization problem is implemented to reflect the user-side demand and the

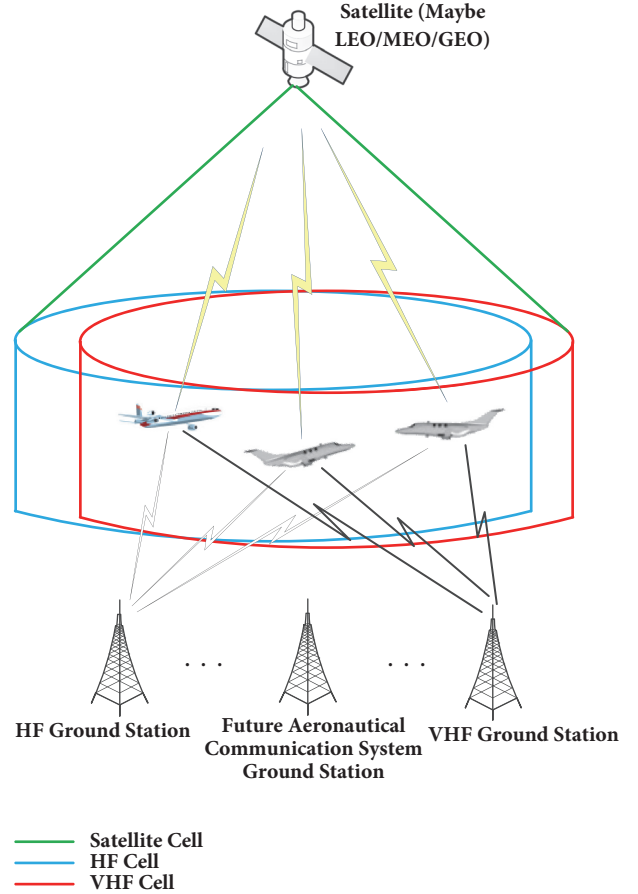


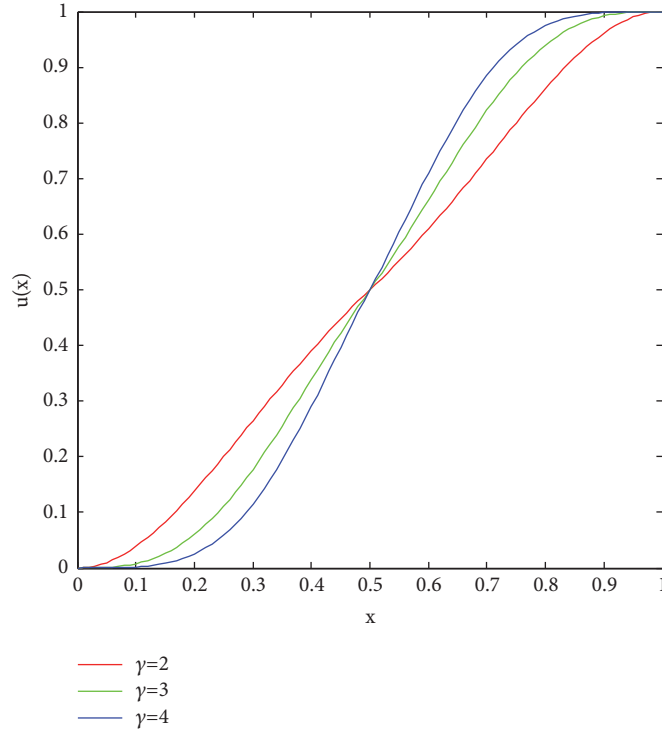
FIGURE 1: Multilink overlapping airspace scenario.

network-side dynamic, and then converted to a single-objective optimization problem solved by the selected optimal link. Secondly, for multiuser link selection, in order to guarantee the access requests of multiple users, the central control mode of Software Define Networking (SDN) [19] is used to assist the user to perform link selection on the network side. By constructing multiuser multiobjective optimization problem, a priority distinction selection algorithm is proposed to maximize the number of users accessing their optimal datalinks and minimize the modification of the user's access request. Finally, the proposed user-side datalink selection scheme and network-side assisted selection algorithm are simulated to verify the feasibility and effectiveness.

This paper is organized as follows. Section 2 establishes the system model and proposes the evaluation models on user side and network side, respectively. The novel datalink selection scheme assisted by the centric network architecture is presented in Section 3. Simulation results are presented in Section 4 and Section 5 concludes the paper.

2. System Description and Problem Formulation

In this section, we formulate the datalink selection problem in the heterogeneous aeronautical network. Specifically, we

FIGURE 2: The utility function under different γ .

consider a heterogeneous aeronautical environment which consists of M different datalinks and N aircraft in the overlapping airspace, as shown in Figure 1. For each datalink, it corresponds to one different ground access network. We assume that every aircraft is independent with each other, and the scene of cooperation between different aircraft is not considered in this paper. Note that network selection and link selection have the same meaning because the end point of the link is the access network, and the terms users and aircraft are interchangeable in this paper.

2.1. The Utility Function on User Side. To effectively evaluate the different attributes of datalinks, we design a universal utility function on user side to map different attributes to corresponding utility metrics. For the sake of generality, we use the Sigmoid function to build this utility that satisfies the following additional conditions:

$$\begin{aligned} u(x) &= 0 \quad \forall x \leq x_{\min} \\ u(x) &= 1 \quad \forall x \geq x_{\max} \\ u(x) &= 0.5, \quad x = x_{\text{mid}} \end{aligned} \quad (1)$$

where x_{\max} and x_{\min} are the maximum and minimum values of the attribute x , respectively, and $x_{\text{mid}} = (x_{\max} + x_{\min})/2$ is the median value.

We construct the utility function that meets (1) as follows [20]:

$$u(x) = \begin{cases} 0 & x \leq x_{\min} \\ \frac{(x/x_{\text{mid}})^\gamma}{1 + (x/x_{\text{mid}})^\gamma} & x_{\min} < x \leq x_{\text{mid}} \\ 1 - \frac{((x_{\max} - x)/(x_{\max} - x_{\text{mid}}))^\gamma}{1 + ((x_{\max} - x)/(x_{\max} - x_{\text{mid}}))^\gamma} & x_{\text{mid}} < x \leq x_{\max} \\ 1 & x > x_{\max} \end{cases} \quad (2)$$

where $\gamma \geq 2$. Figure 2 shows the utility function of different γ . It is straightforward that this utility function is twice differentiable, monotonic, and concavity-convex and satisfies the utility theory [20].

Generally, the attributes of each different link are classified into upward attributes and downward attributes according to their anticipated values. For upward attributes, such as received signal strength (RSS) and transmission rate, we directly use $u(x)$ as their utility function. On the contrary, $1 - u(x)$ is adopted as the utility function for downward attributes, e.g., cost, bit error rate, and delay.

In order to evaluate the datalink more comprehensively, it is not enough to only consider a single attribute, so an overall utility combined by multiple attributes is inevitable. The combined multiattribute utility function should follow the following criteria:

$$\begin{aligned} \frac{\partial U(\mathbf{x})}{\partial u_i} &\geq 0 \\ \text{sign}\left(\frac{\partial U(\mathbf{x})}{\partial x_i}\right) &= \text{sign}\left(\frac{du_i}{dx_i}\right) \end{aligned}$$

$$\begin{aligned} \lim_{u_i \rightarrow 0} U(\mathbf{x}) &= 0, \quad \forall i = 1, \dots, n \\ \lim_{u_1, \dots, u_n \rightarrow 1} U(\mathbf{x}) &= 1 \end{aligned} \quad (3)$$

In the multiattribute utility function, the exponential-multiplication form is commonly used with satisfying constraints (3) [20]. Thus the overall utility of the user j corresponding to the link e_i can be constructed as

$$U_{ij}(\mathbf{x}) = \prod_{k=1}^K u_{ik}(x_{ik})^{\omega_k}, \quad i = 1, 2, \dots, M \quad (4)$$

where \mathbf{x} is the vector consisting of x_{ik} ; $\omega_k \in [0, 1]$ is the weight of the k th attribute x_{ik} of the link e_i and the utility function $u_{ik}(x_{ik})$. It is apparent that $\sum_{k=1}^K \omega_k = 1$, where K is the number of attributes. Although different services of aircraft have different requirements on the importance of each attribute, the weight of each attribute for the same service is fixed for different links and the i-TRUST method can be adopted to determine its value [17].

2.2. The Access Rate on Network Side. Given that there is more than one aircraft that triggers link selection in the overlapping airspace, the load of the access network connected by different link has to be considered to avoid access failure caused by multiuser access simultaneously. However, the increasing flight security problem reminds aircraft do not share their private information with others in a noncooperative scenario. The current selecting user has no idea of the number of other users selecting the same link, and does not know the resources they requested, so it is a challenging problem for current selecting user to select the optimal link that satisfies its required resources and maximize the access rate of target network. Thus, we consider the access rate, which means the probability of current selecting user successfully accessing the target link, as the evaluation metric on the network side.

On account of the imperfect network information about other selecting users, the current selecting user has to estimate this information by the existing knowledge and then regard it as the evaluation criterion on the network side when performing the datalink selection. Therefore, in order to assist a selecting user to infer the link selection behaviours of other selecting users, we investigate the relationship between any two selecting users based on their available link sets, because each one has several available links in the overlapping airspace. According to [21], we use the intersection of available link sets of the two users as the criterion. When the intersection is empty, the two are completely uncorrelated, which means the correlation coefficient is 0 and their link selection behaviours are totally unaffected. Conversely, when the available link sets of the two are identical, the two are absolutely related and their correlation coefficient is 1, which causes that the link selection behaviours have the greatest impacts on accessing the target network. If the intersection is a part of the available link set, then the two will be partially related and the correlation coefficient is between 0 and 1. So in order to estimate the access rate of the target network, the

probability of other users selection target network and their requirements on link resources are two prerequisites.

According to the above analysis, considering the worst case, it is assumed that all selecting users are completely related to the current selecting user, which has the greatest influence on the user link selection. In the heterogeneous aeronautical network, we assume that the current number of users and the remaining available resources of each access network are embedded in the air intelligence, and are periodically transmitted by broadcast to each user in the current airspace. It can be seen that the number of users in the current airspace is $N = \sum_{i=1}^M N_i$, where N_i is the number of users accessing the network e_i . Since the resources used by different multiple access methods are generally different, such as the channel of Frequency Division Multiple Access (FDMA), time slot of Time Division Multiple Access (TDMA), code word of Code Division Multiple Access (CDMA) and time-frequency resource block of Orthogonal Frequency Division Multiple Access (OFDMA), a unified measurement criterion using bit rate is reasonable for different access networks. Therefore, the remaining available bit rate of the current network can be adopted to measure its available resources uniformly, which can be expressed as

$$R_s^i = (N_{\max}^i - N_i) R_{\max}^i \quad (5)$$

where N_{\max}^i is the maximum number of users supported by the link e_i in the current airspace and R_{\max}^i is the maximum bit rate supported by the link e_i .

To ensure the current selecting user to successfully access to the network connected by target link, two factors need to be met. Firstly, the current user needs to select the expected link as the target link. Then, the number of users selecting the target link should be smaller than the maximum number of users supported by the target link in the current airspace, which means that the target link is not fully loaded. Since the target link is selected on the user side according to the overall utility of each link, we can calculate the selected probability of the target link among M datalinks, and its probability can be given by

$$\alpha_{ij} = \frac{U_{ij}(\mathbf{x})}{\sum_{i=1}^M U_{ij}(\mathbf{x})} \quad (6)$$

Secondly, the underload probability of the corresponding target network is calculated. The current selecting user lacks of the information of other selecting users in the same airspace, so we assume that other selecting users can select the best link based on available resources according to the Always Best Connection (ABC) [22] criterion. The probability of each user selecting a link based on available resources can be expressed as

$$q_i = \frac{R_s^i}{\sum_{i=1}^M R_s^i} \quad (7)$$

For the target link, the total number of users at the next moment consists of two parts: one is the number of users switching from other links to the current link N_{o2i} ; the other

is the number of users who maintain the access to current link N_{i2i} . The probability of the former N_{o2i} can be calculated by the current selecting user according to the estimated information of other selecting users as follows:

$$\begin{aligned} P\{N_{o2i} | N - N_i - 1\} \\ = \binom{N - N_i - 1}{N_{o2i}} (q_i)^{N_{o2i}} (1 - q_i)^{N - N_i - 1 - N_{o2i}} \end{aligned} \quad (8)$$

Following the same reason, the distribution probability of the latter N_{i2i} can be given by

$$P\{N_{i2i} | N_i\} = \binom{N_i}{N_{i2i}} (\gamma_i)^{N_{i2i}} (1 - \gamma_i)^{N_i - N_{i2i}} \quad (9)$$

where γ_i is the probability of user staying on the current link and can be estimated by the same probability of current selecting user.

Only when $N_{i2i} + N_{o2i} \leq N_{\max}^i - 1$ does the current selecting user accessing the target link have no collisions with other users, therefore, the underload probability of target link is expressed as

$$P_{\text{Underload}}^i = P\{N_{i2i} + N_{o2i} \leq N_{\max}^i - 1\} \quad (10)$$

where $N_{i2i} + N_{o2i}$ is a simple two-dimensional random variable.

Consequently, the access rate of the target network can be obtained as follows:

$$P_{\text{Access}}^{ij} = \alpha_{ij} P_{\text{Underload}}^i \quad (11)$$

3. The Proposed Datalink Selection Scheme

In this section, we propose the datalink selection on the user side and the network-assisted selection scheme on the network side.

3.1. User-Side Selection Scheme. Since the users generally have a multilink configuration for safety, we only consider the scenario of selecting the optimal link when multiple links are available and use β_{ij} to indicate the result of link selection, where

$$\beta_{ij} = \begin{cases} 1, & \text{if current user select datalink } e_i \\ 0, & \text{otherwise.} \end{cases} \quad (12)$$

When only the link selection on the user side is considered, the user desires to select the link with the largest overall utility. At this time, the user-side evaluation model can be established as the following optimization problem:

$$\begin{aligned} \max \quad \mathcal{O}_j^1 &= \sum_{i=1}^M \beta_{ij} U_{ij}(\mathbf{x}) \\ \text{s.t.} \quad \sum_{i=1}^M \beta_{ij} &\leq 1 \end{aligned} \quad (13)$$

where $\sum_{i=1}^M \beta_{ij} \leq 1$ means that at most one link can be selected among all the available links, and the constraint can be easily extended to the selection of multiple links.

Similarly, when only considering the link selection on the network side, the user expects to select the link with the highest access rate. The optimization problem established by using the network-side evaluation model is given by

$$\begin{aligned} \max \quad \mathcal{O}_j^2 &= \sum_{i=1}^M \beta_{ij} P_{\text{Access}}^{ij} \\ \text{s.t.} \quad \sum_{i=1}^M \beta_{ij} &\leq 1 \end{aligned} \quad (14)$$

However, in the actual link selection, the user should not only consider the user-side evaluation model, but also consider the evaluation model on the network side; that means the current selecting user expects to both obtain the maximum utility and the highest access rate. Consequently, combining \mathcal{O}_j^1 and \mathcal{O}_j^2 under the same constraints, the multiobjective optimization problem $\{\mathcal{O}_j^1, \mathcal{O}_j^2\}$ can be established. For the multiobjective optimization, according to the importance of each target, the simple weighting method is usually adopted to transform multiple objectives into a single-objective optimization problem to obtain an acceptable solution under certain compromise [23]. According to [24], the feasible solution of transformed single-objective optimization is one of Pareto optimal solutions when each weight of single target is greater than zero.

Therefore, the multiobjective optimization problem $\{\mathcal{O}_j^1, \mathcal{O}_j^2\}$ under the same constraints of \mathcal{O}_j^1 or \mathcal{O}_j^2 can be transformed into the following single-objective optimization problem:

$$\begin{aligned} \max \quad \mathcal{O}_j &= \lambda_j \cdot \mathcal{O}_j^1 + (1 - \lambda_j) \cdot \mathcal{O}_j^2 \\ \text{s.t.} \quad \sum_{i=1}^M \beta_{ij} &\leq 1 \end{aligned} \quad (15)$$

where $\lambda_j \in [0, 1]$ and $1 - \lambda_j$ are the weights of the \mathcal{O}_j^1 and \mathcal{O}_j^2 , respectively, which represent the significance of the user-side and the network-side objectives on the decision making. When $\lambda_j = 1$, the optimization problem (15) is converted to the user-side optimization, and to the network-side optimization when $\lambda_j = 0$. Therefore, λ_j should be determined by user's requirement and generally set to 0.5 considering the fairness between the user and the network. Considering that the objective function and constraints in (15) are linear and the number of available links for each user is limited, the multiobjective optimization can be solved by the integer programming method [25].

The link selection scheme we proposed on the user side is as shown in Figure 3. In general, the steps involved in this user-side scheme are summarized as follows.

Step 1. The prelink screening [17] is firstly performed to find candidate links that meet the requirements.

Step 2. If there is only one candidate link after the prelink screening, it will be chosen as the target link to establish connection.

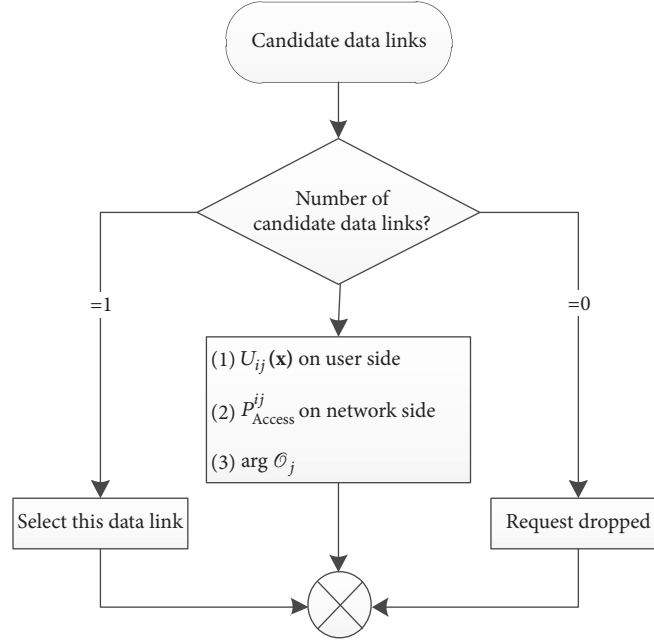


FIGURE 3: Link selection scheme on user side.

Step 3. If there is no available link, no connection will be established and the request will be dropped.

Step 4. If there are more than one candidate links, the link utility on the user side is first calculated, and then the access rate on the network side is calculated. Subsequently, the optimization problem \mathcal{O}_j is constructed and solved, and the candidate link corresponding to the maximization of \mathcal{O}_j is determined as the optimal link.

Due to the simple search method can be used to solve the optimization problem \mathcal{O}_j because of the limited candidate links, we sort the links according to their \mathcal{O}_j decreasingly to form a priority list, then the selected optimal link is the first element in this list.

3.2. Network-Assisted Selection Scheme. Due to the limited resources of heterogeneous aeronautical network, the target access network will have serious collisions if all selecting users in the same airspace utilize the above-mentioned user-side scheme to select the optimal link. In this multiuser access scenario, the heterogeneous aeronautical network needs to assist user to perform the link selection and ensure each user's access request with minimal modification.

In the overlapping airspace, both the selecting users and the nonselecting users are included among the N users. For the selecting user, it needs to select the optimal link according to the service requirement, whereas for the nonselecting user staying in certain link, it can be considered as a special selecting user who only has one candidate link that is actually the original link. We establish an optimization model for this scenario from the user's perspective to optimize all N users' requests as follows:

$$\max \quad \{\mathcal{O}_1, \mathcal{O}_2, \dots, \mathcal{O}_N\}$$

$$\text{s.t.} \quad \sum_{i=1}^M \beta_{ij} \leq 1$$

$$\sum_{j=1}^N \beta_{ij} \leq N_{\max}^i$$

(16)

where $\sum_{j=1}^N \beta_{ij} \leq N_{\max}^i$ represents the number of users accessing the network e_i cannot exceed the maximum number of users supported by this network.

The multiobjective optimization problem in (16) can be transformed into a maximum-minimum problem by the weighted Tchebycheff method [26] as follows:

$$\min \quad \max_j \{\phi_j (\mathcal{O}_j^o - \mathcal{O}_j)\}$$

$$\text{s.t.} \quad \phi_j > 0$$

$$\sum_{i=1}^M \beta_{ij} \leq 1$$

$$\sum_{j=1}^N \beta_{ij} \leq N_{\max}^i$$

(17)

where $\mathcal{O}_j^o = \max \mathcal{O}_j$ is the maximum of \mathcal{O}_j and ϕ_j is the positive weight assigned to the user j by the heterogeneous network.

The objective function in the optimization problem (17) can be further transformed into the following objective function:

$$\min \quad \sum_{j=1}^N \{\phi_j (\mathcal{O}_j^o - \mathcal{O}_j)\} \quad (18)$$

Generally, considering the fairness between different users, we assume the same ϕ_j is reasonable for each user. Under this assumption, the solution of optimization problem (18) is a Pareto optimal solution for the multiobjective optimization problem [26]. As a combinatorial optimization, the complexity of optimization problem (18) increases exponentially with the number of users and their candidate links and will lead to a NP-hard problem which causes the traditional optimal search method searching one by one to be unimplementable.

In order to reduce the complexity of solving combinatorial optimization, suboptimal intelligent optimization algorithms, such as Genetic Algorithm (GA) [27] and Particle Swarm Optimization (PSO) [28], are generally used to approximate the optimal solution. However, the complexity of the intelligent optimization algorithm is still very high and the approximate optimum solution is not optimal for the users because the optimization problem (18) is established from the heterogeneous network's perspective.

Therefore, from the user's perspective, a priority distinction selection (PDS) algorithm on the network side is proposed by setting user's priority to maximize the number of users accessing their optimal links. We use the number of available links to distinguish the user priority, which means the smaller the number of available links, the higher the priority of the user. Particularly, the flexibility of the user decreases with the increasing number of available links. By setting the priority, the high priority users with low flexibility are allowed to access at first and followed by the low priority users subsequently. For the group of users with the same priority, the underload links can be accessed by the users who evaluate them as optimal links, and then the access of other users in this group will be allowed if the resources are plenty enough. Thereby, we can guarantee the maximal number of users to access their optimal links and the whole heterogeneous network in the meanwhile. The steps of the proposed PDS algorithm for optimization problem (18) are as shown in Algorithm 1.

Step 1. Firstly, the user A_j^i with i candidate links can be classified in the set \mathbf{G}_i ; that means $A_j^i \in \mathbf{G}_i$, $1 \leq i \leq M$. Correspondingly, the accessible network resources of A_j^i are $\mathbf{Re} = \{\text{Re}_t^1, \dots, \text{Re}_t^i\}$, $1 \leq t, t \leq M$, where Re_t^i represents the remaining number of access user supported by i th available link, which is sorted by user-side utility (note that the \mathbf{Re} of each user is different).

Step 2. For a user with only a single available link $A_j^1 \in \mathbf{G}_1$, the available resource of the link is $\mathbf{Re} = \{\text{Re}_t^1\}$, and the link e_t is the optimal access link. If $\text{Re}_t^1 \geq 1$, we can get $\beta_{tj} = 1$ which means the user A_j^1 can access link e_t , and then \mathbf{Re} should be updated after access; otherwise, the user A_j^1 cannot access any link because of $\beta_{tj} = 0$.

Step 3. For users with multiple available links $A_j^i \in \mathbf{G}_i$, $i > 1$, the available resources are $\mathbf{Re} = \{\text{Re}_t^1, \dots, \text{Re}_t^i\}$, where $l \neq t \& 1 \leq l, t \leq M$. Firstly, the user who can access the

```

Step 1: Sort  $A_j^i \in \mathbf{G}_i$ ,  $\mathbf{Re} = \{\text{Re}_t^1, \dots, \text{Re}_t^i\}$ 
Step 2:
For all  $A_j^1 \in \mathbf{G}_1$ ,  $\mathbf{Re} = \{\text{Re}_t^1\}$ ;
    If  $\text{Re}_t^1 \geq 1$ ,  $\beta_{tj} = 1$ ,  $A_j^1$  can access  $e_t$ , update  $\mathbf{Re}$ ;
    else  $\beta_{tj} = 0$ , no network can be accessed by  $A_j^1$ .
Step 3:
For all  $A_j^i \in \mathbf{G}_i$ ,  $i > 1$ ,  $\mathbf{Re} = \{\text{Re}_t^1, \dots, \text{Re}_t^i\}$ ;
    If  $\text{Re}_t^1 \geq 1$ ,  $\beta_{tj} = 1$ ,  $A_j^i$  can access  $e_t$ , and update
Re;
    else put  $A_j^i$  to candidate set  $\mathbf{D}_i$ .
For  $k = 1, \dots, i - 1$ 
    If  $\mathbf{D}_i = \emptyset$ , break;
    else For all  $A_j^i \in \mathbf{D}_i$ ;
        If  $\text{Re}_t^{k+1} \geq 1$ ,  $A_j^i$  can access to  $e_t$  and be
        deleted from  $\mathbf{D}_i$ , and then update  $\mathbf{Re}$ ;
        else  $A_j^i$  still stay in  $\mathbf{D}_i$ .
    If  $k = i - 1$ ,  $\mathbf{D}_i \neq \emptyset$ ,  $A_j^i \in \mathbf{D}_i$  can't access any
    network, and need to wait the next selection.

```

ALGORITHM 1: The proposed priority distinction selection algorithm.

optimal link is judged according to the link resources, which is the same as the user with single available link. For all users $A_j^i \in \mathbf{G}_i$, $i > 1$, if $\text{Re}_t^1 \geq 1$, the user A_j^i can access the optimal link e_t because of $\beta_{tj} = 1$, then \mathbf{Re} is updated; however, for other users in \mathbf{G}_i , we sort them in a candidate set \mathbf{D}_i . For the users in the candidate set $A_j^i \in \mathbf{D}_i$, we repeat the above operation, and currently the user needs to search backwards for the suboptimal accessible link because of $\text{Re}_t^1 = 0$. If the resources are available, the access is performed and the current user is deleted from \mathbf{D}_i ; otherwise, the user continues to be retained in \mathbf{D}_i . Ultimately if there are still users in \mathbf{D}_i after $i - 1$ iterations, they cannot access to any link and need to wait for the next link selection.

Therefore, the proposed network-assisted selection scheme is based on the user's priority. First of all, the link selection mechanism on the user side is performed for each user, and then an access request with the sorted candidate link list is sent by the selected optimal link to heterogeneous aeronautical network. We assume that the heterogeneous network adopts a central control mode of SDN [19], the network receives the access requests of all users and then optimizes these requests according to (18) by PDS algorithm. Eventually, the network sends an acknowledgement to each user on the optimized access link, suppose that the user's reception detection is performed on each candidate link.

4. Performance Evaluation

Due to the poor availability and reliability of HF communications, HF links are not considered here. Assume that Iridium, VDL2, Inmarsat broadband global area network (BGAN) [29], and Mobile User Objective System (MUOS) [30] are the available links for aircraft in the overlapping airspace and

TABLE 1: The specific attributes of different aeronautical links [17].

Attributes	Links			
	Iridium	VDL2	BGAN	MUOS
BR(kbps)	Up to 2.4	Up to 31.5	Class 4: up to 200 Class 6: up to 432	Up to 64
PD(ms)	Up to 748	Up to 2000	Up to 1100	Up to 1000
RSS(dBm)	-	-	-	-
CST(\$/MB)	7	1	3	5

TABLE 2: Utility values for different services.

Links	Attributes				Services			
	BR (kbps)	PD (ms)	RSS (dBm)	CST (\$/MB)	20 kbps		2 kbps	
					safety	non-safety	safety	non-safety
Iridium	2.1	100	-84	7	-	-	-	0.5260
VDL2	31.5	50	-80	1	-	0.6163	-	0.6163
BGAN1	32	260	-100	3	-	0.1933	-	0.1933
BGAN2	32	260	-82	3	-	0.1871	-	0.1871
MUOS	40	260	-100	5	-	0.3369	-	0.3369

their specific parameters are listed in Table 1 [17]. Since Class 4 and Class 6 of BGAN only differ in transmission rate, they can be expressed as BGAN1 and BGAN2, respectively. In this paper for so many attributes of each different link, only the corresponding bit rate (BR), packet delay (PD), received signal strength (RSS), and cost (CST) are considered.

4.1. The User-Side Selection Scheme. To begin with, we calculate the overall utility on the user side. Assume that the RSS vector of the five datalinks is [-84, -80, -100, -82, -100] in dBm shown in Table 2, the BR can be calculated by the current RSS accordingly. Since all three satellite links of BGAN1, BGAN2, and MUOS use synchronous orbit satellites, it can be assumed that the minimum propagation delay of one-hop is 260 ms. And considering the cost of data transmission, we can see that the costs of Iridium and VDL2 are the highest and lowest compared with other links, respectively.

Take the 20kbps security service as an example to calculate the user-side utility. The prescreening of the available links is performed firstly. Since the VDL2 does not support the safety service, the available link sets are BGAN1, BGAN2, and MUOS as shown in Table 2. Under the principle of quality priority, the weights of attributes required by the service can be obtained by the i-TRUST method, where $\omega = [0.30 \ 0.15 \ 0.50 \ 0.05]$. The overall utilities of 20kbps in different links calculated are $U_{BGAN1} = 0.1933$, $U_{BGAN2} = 0.1871$, and $U_{MUOS} = 0.3369$. For the 2 kbps security service, the other four links except VDL2 are candidate links. Under the same weights as the 20 kbps service, the user-side utility of Iridium is 0.5260. If only the link selection on the user side is considered, the best link for the 20 kbps safety service is MUOS, and the best link for the 2 kbps safety service is the Iridium link. For nonsafety services of 2kbps or 20kbps, VDL2 is a candidate solution, but the Iridium link is not included in candidate set of the 20kbps nonsafety service.

According to Table 2, users with 20kbps or 2 kbps nonsafety service tend to choose the most efficient VDL2 link.

Secondly, we calculate the access rate by the underload probability on the network side. We assume that there are a total of 200 aircraft in the overlapping airspace which remains stable at the current time, and the vector of the maximum number of users supported by the five datalinks is [40, 70, 50, 50, 80]. For different γ_i , the $P_{\text{Underload}}^i$ changing with the number of users in the target network is shown in Figure 4. When the number of users in the Iridium network is less than $N_{\text{max}}^i = 40$, the $P_{\text{Underload}}^i$ of the Iridium network is all 100% that is because the resources of Iridium network occupy a tiny proportion of the total resources and the probability of other users choosing the Iridium is diminutive in the heterogeneous network. The underload probabilities of other networks increase with the ascending number of users due to the substantive scenarios of $N_{i2i} + N_{o2i}$. Considering more opportunities of current users switching to other links when the number of users held in the target network grows, the possible chances of users in other networks to handover to the target network increase, which augments the $P_{\text{Underload}}^i$ of the target network. Generally, $P_{\text{Underload}}^i$ increases with the descending γ_i in Figure 4(b) compared with Figure 4(a), due to the decreasing γ_i leading to the incremental availability of other users.

As for the access rate of different links shown in Figure 5, the change trend of P_{Access}^{ij} is consistent with $P_{\text{Underload}}^i$ when α_{ij} remains unchanged, but the P_{Access}^{ij} is lower than $P_{\text{Underload}}^i$. With the declining number of users in the target network, P_{Access}^{ij} gradually decreases because so many resources can be utilized by other users with high selecting probabilities. On the contrary, a considerable P_{Access}^{ij} can be achieved with the growing number of users benefiting from the more dynamic in the target network.

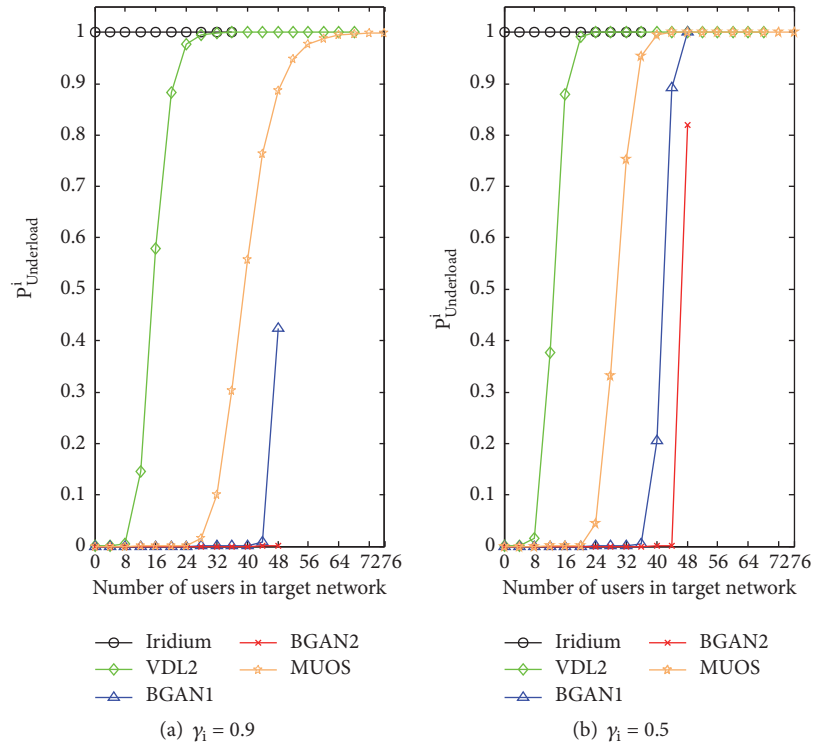


FIGURE 4: The $P^i_{Underload}$ of the current network under different user numbers in different links.

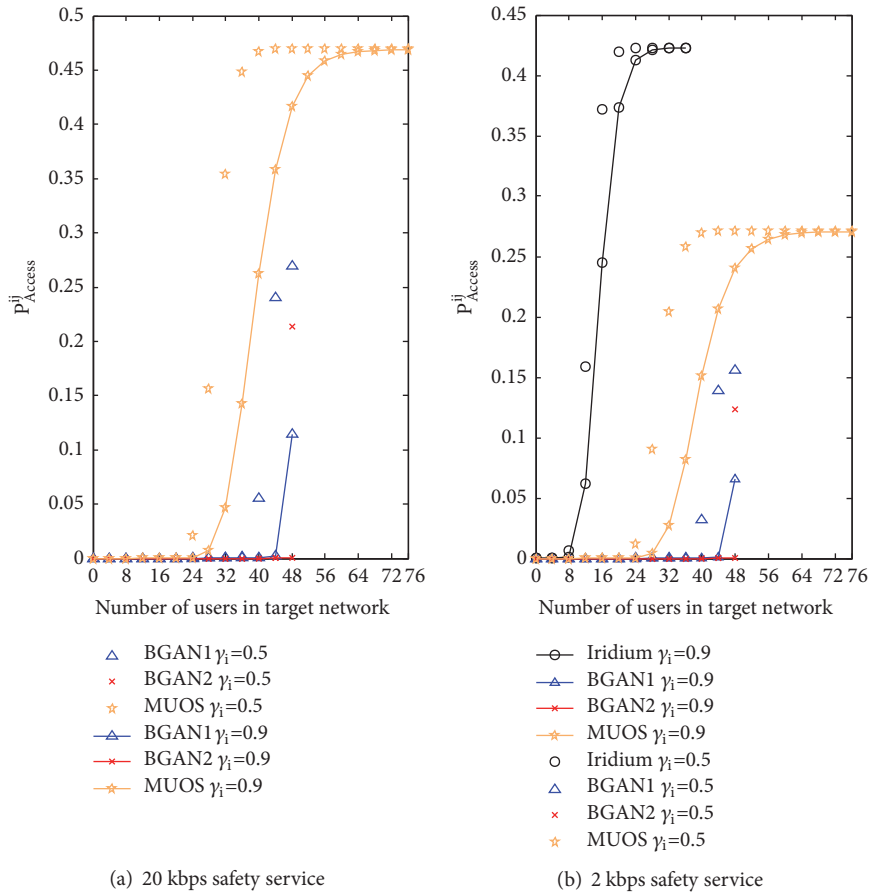


FIGURE 5: The P^ij_{Access} of 20kbps and 2kbps safety services.

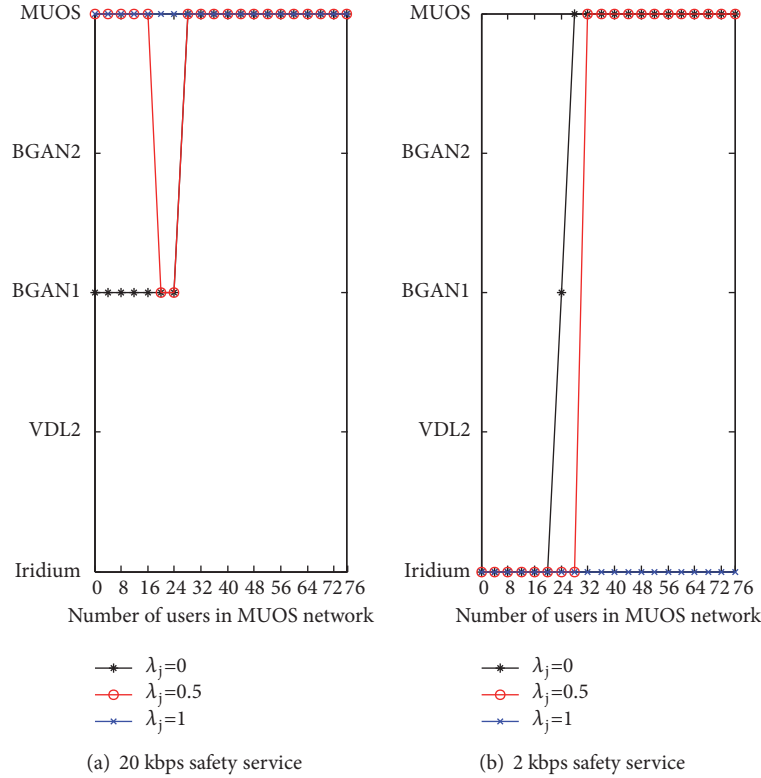


FIGURE 6: The datalink selection results of different services in MUOS network.

TABLE 3: The available datalinks and their utilities of different users.

User	Network ID					User	Network ID				
	1	2	3	4	5		1	2	3	4	5
1	1	0	0	0	0	11	0	0.4	0.3	0.6	0
2	0	1	0	0	0	12	0	0	0.5	0.3	0.4
3	0	0	1	0	0	13	0.2	0	0.4	0	0.6
4	0	0	0	0.5	0.7	14	0	0	0	0.4	0.3
5	0.5	0.7	0	0	0	15	0.2	0	0.5	0	0.4
6	0	0.4	0	0.6	0	16	0.2	0.4	0.5	0.3	0
7	0	0	0.5	0	0.4	17	0	0.7	0.5	0.3	0.4
8	0	0	0	0.4	0.6	18	0.2	0.7	0.5	0	0.4
9	0.7	0	0	0.4	0	19	0.2	0.4	0.6	0.3	0.7
10	0.2	0.6	0.5	0	0	20	0.7	0.8	0.6	0.3	0.4

Finally, the results of user-side selection in MUOS network are shown in Figure 6 as an example. With the incremental number of users, the user selects the optimal link with the maximum P_{Access}^{ij} when $\lambda_j = 0$. Conversely, the user would like to select the link with maximum $U_{ij}(\mathbf{x})$ when $\lambda_j = 1$, which results in conflicts among other users on the network side such as the Iridium link selected by 2kbps safety service in Figure 6(b). For $\lambda_j = 0.5$, the user considers the over utility and access rate more fairly for the optimal link selection.

4.2. The Network-Assisted Selection Scheme. In order to simplify the presentation complexity, the scenario with the

number of users $N = 20$ and the number of above-mentioned links $M = 5$ is considered, and the accessible networks corresponding to each user and their overall utilities are shown in Table 3. On the network side, we use $Rate = (\sum_{j=1}^N \max \mathcal{O}_j - \sum_{j=1}^N \mathcal{O}_j) / \sum_{j=1}^N \max \mathcal{O}_j$ to measure the performance of the proposed algorithm, where \mathcal{O}_j is the value of each user accessing the corresponding network after using the proposed PDS algorithm. On the user side, we use the number of users accessing the heterogeneous network N_a and the number of users accessing optimal link N_o to measure the performance. The proposed PDS algorithm is compared with the GA and PSO intelligent algorithms, whose number

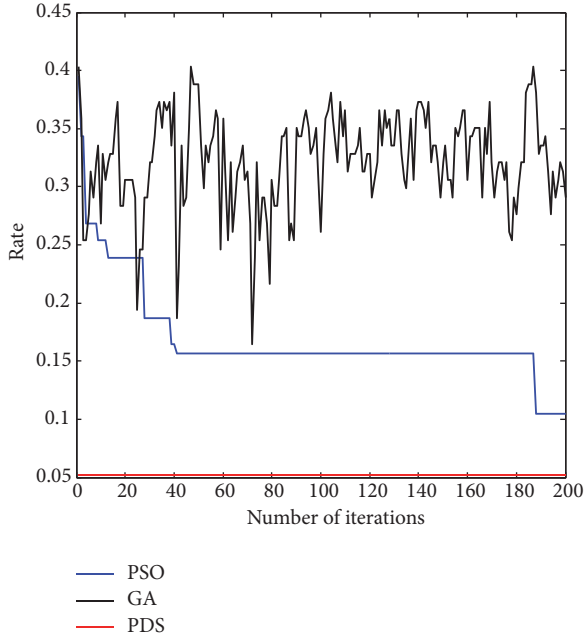


FIGURE 7: The *Rate* of different algorithms under $\text{Renet} = [3\ 5\ 4\ 3\ 5]$.

of iterations is set to 200 and population size is 100 for saving the processing time.

Firstly, 20 network resources are taken as an example to verify the performance of proposed algorithm. We assume that the number of available resources corresponding to each network is $\text{Renet} = [3\ 5\ 4\ 3\ 5]$. Without considering resource constraints, the maximum cumulative utility achieved by the access link is 13.4 according to Table 3. As shown in Figure 7, the maximum cumulative utility obtained by the GA algorithm is 11.2, and correspondingly the minimum of *Rate* is 16.42% in the 200 iterations. Simultaneously when *Rate* reaches its minimum, Figure 8 presents that N_a is equal to 19 and N_o equals 9, which means 10 users access the nonoptimal links and one user cannot access the heterogeneous network. Through multiple selection, crossover and mutation operations, the *Rate* of GA algorithm does not converge to a stable value, because the above operations cause individuals to become random and do not evolve in an optimal direction during evolution. Moreover, for all access schemes corresponding to individuals in GA algorithm, not all of them meet resource constraints. On the contrary, the PSO algorithm gradually converges to the local optimal solution through multiple iterations. The maximum utility value obtained at this time is 12, and the *Rate* gradually stabilizes at 10.45%. Meanwhile, $N_a = 20$ and $N_o = 12$, which means there are 8 users switching from the expected optimal link to the nonoptimal link, so the PSO performance is better than the GA algorithm. From Figure 7 we can see that the PDS algorithm has the best performance, because the PDS algorithm is a deterministic search algorithm which does not need multiple iterations and has low complexity. The cumulative utility obtained by PDS algorithm is 12.7, and the *Rate* is only 5.22%. Currently, the N_a is equal to 20 and N_o

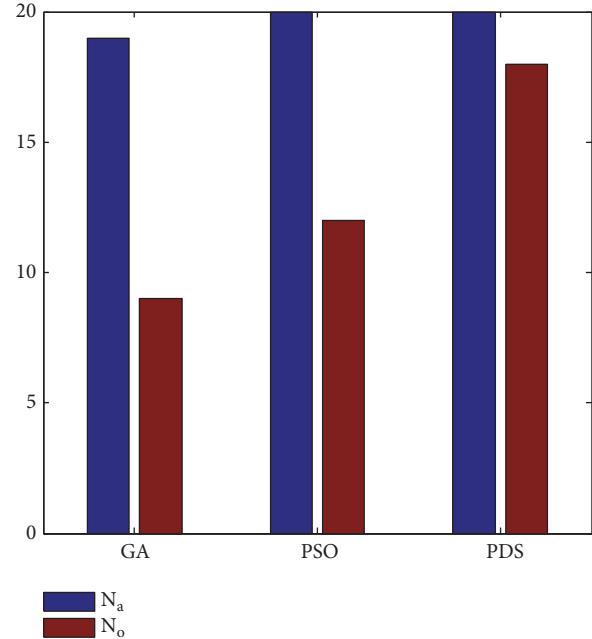


FIGURE 8: N_a and N_o of different algorithms under $\text{Renet} = [3\ 5\ 4\ 3\ 5]$.

equals 18 according to Figure 8, which means only the 19th and the 20th users cannot access the optimal link. Therefore, the required modification for users' link selection in this PDS algorithm is the smallest compared with GA and PSO.

When the resources of heterogeneous network are less than the number of users, for example, in the case where the number of access network resources is $\text{Renet} = [2\ 4\ 3\ 2\ 4]$, the three algorithms are evaluated. As can be seen from Figure 9, the GA algorithm still does not converge with the reduction of network resources, and the minimum of *Rate* is 33.58% in 200 iterations. Meanwhile $N_a = 14$ and $N_o = 10$ can be reached by GA algorithm according to Figure 10, which means one user cannot access and four users have to access to nonoptimal links. With the reduction of resources, the PSO algorithm gradually improves its search performance and is superior to the PDS algorithm in the *Rate*, which is stable at 4.67% as the iteration increases, because the search range of PSO is drastically reduced and it can reach the optimal solution from the perspective of the network. Only $N_o = 12$ out of $N_a = 15$ users can access to their optimal links when using PSO algorithm; however, for the PDS algorithm the N_o can reach 13 with $N_a = 15$ although the *Rate* is 27.61% at this time. From the user's perspective when the network resources are gradually reduced, the PDS algorithm is still better than PSO algorithm and can reduce the complexity without the multiple iterations. Therefore, the DSP algorithm can maximize the number of users accessing the optimal links and minimize the user' modification greatly compared with GA and PSO algorithms.

5. Conclusions

This paper proposes a novel network-assisted datalink selection mechanism for heterogeneous aeronautical network in

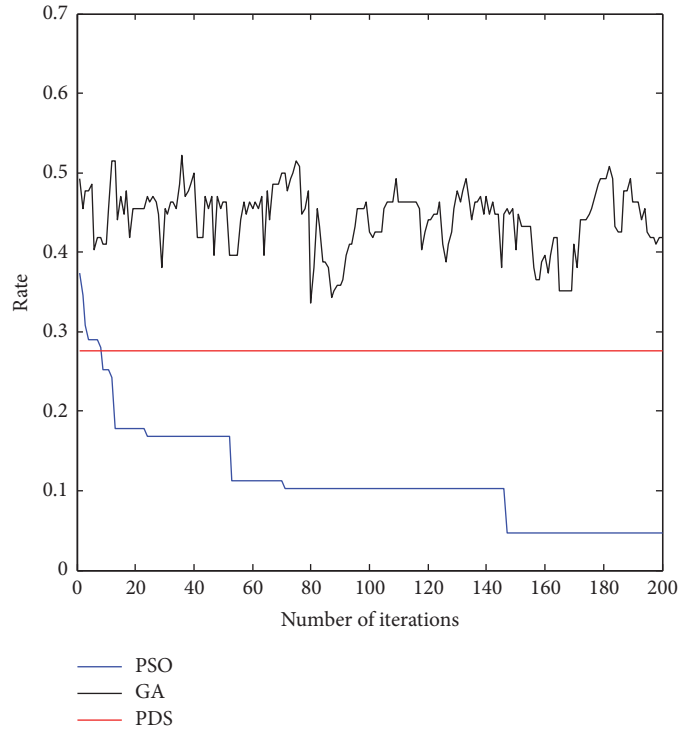


FIGURE 9: The Rate of different algorithms under Renet = [2 4 3 2 4].

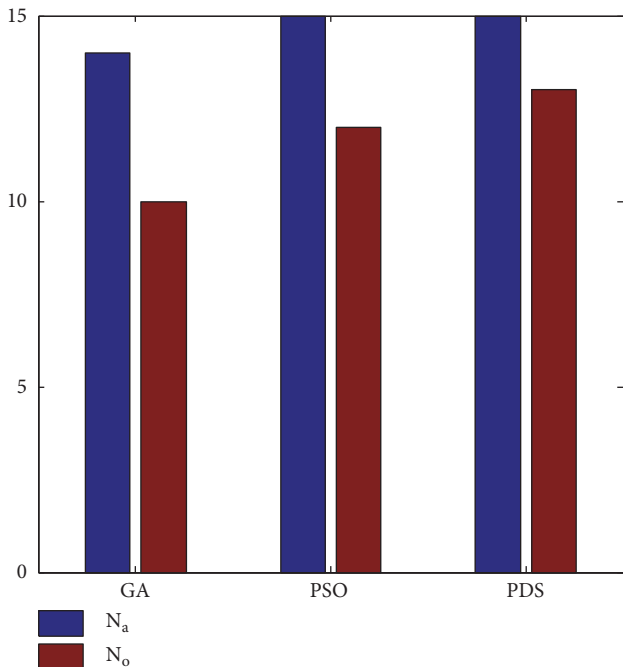


FIGURE 10: N_a and N_o of different algorithms under Renet = [2 4 3 2 4].

multilink overlapping airspace. For a single-user selection, the user combines the user-side utility with the network-side access rate to optimize and select the optimal link. For multiuser selection, combined with the network-side central

control mode, a priority distinction selection algorithm with low complexity is proposed to assist users to perform link selection, maximize the number of users accessing their optimal links, and minimize the user-side modification. The effectiveness of the proposed selection scheme with proposed algorithm is validated by simulations. In the future, we will study the multilink selection, especially dual-connectivity scheme, to support the high mobility of aircraft. By utilizing the multilink connectivity, the aircraft can reduce the unnecessary handover for realizing a seamless communication and make use of the diversity to improve the robustness and reliability. Furthermore, under the constraint of limited resources we will optimize the global performance of the aeronautical heterogeneous network considering dual-connectivity users in the overlapping airspace.

Data Availability

The data used to support the findings of this study is included within the article.

Conflicts of Interest

The authors declare that there are no conflicts of interest regarding the publication of this paper.

Acknowledgments

This work was supported by the National Natural Science Foundation of China (Grant 61701521), the China Post-doctoral Science Foundation (Grant 2016M603044), and

the Shaanxi Provincial Natural Science Foundation (Grant 2018JQ6074).

References

- [1] AIRBUS GLOBAL MARKET FORECAST 2017-2036. http://www.aircraft.airbus.com/market/global-market-forecast20172036/?eID=maglisting_push&tx_maglisting_pil%5BdocID%5D=233685.
- [2] D. G. Depoorter and W. Kellerer, "Designing the Air-Ground Data Links for Future Air Traffic Control Communications," *IEEE Transactions on Aerospace and Electronic Systems*, 2018.
- [3] I. Jawhar, N. Mohamed, J. Al-Jaroodi, D. P. Agrawal, and S. Zhang, "Communication and networking of UAV-based systems: Classification and associated architectures," *Journal of Network and Computer Applications*, vol. 84, pp. 93–108, 2017.
- [4] X. Wang, Z. Ouyang, H. Song, and Q. Lin, "Collaborative unmanned aerial systems for effective and efficient airborne surveillance," in *Proc. SPIE 10652, Disruptive Technologies in Information Sciences*, vol. 106520F, 2018.
- [5] X. Yue, Y. Liu, J. Wang, H. Song, and H. Cao, "Software Defined Radio and Wireless Acoustic Networking for Amateur Drone Surveillance," *IEEE Communications Magazine*, vol. 56, no. 4, pp. 90–97, 2018.
- [6] J. Fan, D. Li, R. Li, T. Yang, and Q. Wang, "Analysis for cooperative combat system of manned-unmanned aerial vehicles and combat simulation," in *Proceedings of the IEEE International Conference on Unmanned Systems (ICUS)*, IEEE, pp. 204–209, 2017.
- [7] B. Kubera and M. Ehammer, "A survey of multilink concepts for aeronautical data link communications," in *Proceedings of the 2013 13th Annual Integrated Communications, Navigation and Surveillance Conference, ICNS 2013*, USA, April 2013.
- [8] Next generation air transportation system - Integrated plan, U.S. Dept. Transp., Washington, DC, 2004.
- [9] State of progress with the project to implement the new generation European Air Traffic Management System (SESAR), European Union, Brussels, Belgium, 2007.
- [10] M. Schnell and S. Scalise, "NEWSKY—concept for NEtworking the SKY for civil aeronautical communications," *IEEE Aerospace and Electronic Systems Magazine*, vol. 22, no. 5, pp. 25–29, 2007.
- [11] S. Plass, "Seamless networking for aeronautical communications: One major aspect of the SANDRA concept," *IEEE Aerospace and Electronic Systems Magazine*, vol. 27, no. 9, pp. 21–27, 2012.
- [12] M. Schnell, U. Epple, D. Shutin, and N. Schneckenburger, "LDACS: Future aeronautical communications for air-traffic management," *IEEE Communications Magazine*, vol. 52, no. 5, pp. 104–110, 2014.
- [13] G. Bartoli, R. Fantacci, and D. Marabissi, "AeroMACS: A new perspective for mobile airport communications and services," *IEEE Wireless Communications Magazine*, vol. 20, no. 6, pp. 44–50, 2013.
- [14] VHF air-ground digital link (VDL) mode 2, Technical characteristics and methods of measurement for ground-based equipment, Part 1: Physical layer and MAC sub-layer, ETSI, Sophia Antipolis, France, 2010, pp. 1–53.
- [15] C. Kissling, "Data link selection in mobile aeronautical telecommunication networks," in *Proceedings of the 27th IET and AIAA International Communications Satellite Systems Conference (ICSSC 2009)*, pp. 1–8, Edinburgh, UK.
- [16] L. Wang and D. Binet, "TRUST: A trigger-based automatic subjective weighting method for network selection," in *Proceedings of the 2009 5th Advanced International Conference on Telecommunications, AICT 2009*, pp. 362–368, Italy, May 2009.
- [17] A. S. Alam, Y.-F. Hu, P. Pillai, K. Xu, and J. Baddoo, "Optimal Datalink Selection for Future Aeronautical Telecommunication Networks," *IEEE Transactions on Aerospace and Electronic Systems*, vol. 53, no. 5, pp. 2502–2515, 2017.
- [18] P. W. Lemme, S. M. Glenister, and A. W. Miller, "Iridium aeronautical satellite communications," *IEEE Aerospace and Electronic Systems Magazine*, vol. 14, no. 11, pp. 11–16, 1999.
- [19] L. Qiang, J. Li, Y. Ji, and C. Huang, "A novel software-defined networking approach for vertical handoff in heterogeneous wireless networks," *Wireless Communications and Mobile Computing*, vol. 16, no. 15, pp. 2374–2389, 2016.
- [20] D. Jiang, L. Huo, Z. Lv, H. Song, and W. Qin, "A Joint Multi-Criteria Utility-Based Network Selection Approach for Vehicle-to-Infrastructure Networking," *IEEE Transactions on Intelligent Transportation Systems*, vol. 19, no. 10, pp. 3305–3319, 2018.
- [21] L. Qiang, J. Li, and E. Altman, "A novel distributed network selection scheme for heterogeneous wireless network environments," *IEEE Transactions on Control of Network Systems*, vol. 4, no. 3, pp. 575–586, 2017.
- [22] J. Kellokoski, J. Koskinen, and T. Hämäläinen, "Always best connected heterogeneous network concept," *Wireless Personal Communications*, vol. 75, no. 1, pp. 63–80, 2014.
- [23] M. Bin, D. Hong, and X. Xianzhong, "Two-sided Matching Model Based Vertical Handover Algorithm in Heterogeneous Wireless Networks," *Journal of Electronics Information Technology*, vol. 40, no. 2, pp. 421–429, 2018.
- [24] L. A. Zadeh, "Optimality and non-scalar-valued performance criteria," *IEEE Transactions on Automatic Control*, vol. 8, no. 1, pp. 59–60, 1963.
- [25] J. S. Borrero, C. Gillen, and O. A. Prokopyev, "A simple technique to improve linearized reformulations of fractional (hyperbolic) 0-1 programming problems," *Operations Research Letters*, vol. 44, no. 4, pp. 479–486, 2016.
- [26] G. Yu, Y. Jiang, L. Xu, and G. Y. Li, "Multi-objective energy-efficient resource allocation for multi-RAT heterogeneous networks," *IEEE Journal on Selected Areas in Communications*, vol. 33, no. 10, pp. 2118–2127, 2015.
- [27] D. Whitley, "A genetic algorithm tutorial," *Statistics and Computing*, vol. 4, no. 2, pp. 65–85, 1994.
- [28] I. C. Trelea, "The particle swarm optimization algorithm: convergence analysis and parameter selection," *Information Processing Letters*, vol. 85, no. 6, pp. 317–325, 2003.
- [29] A. Franchi, A. Howell, and J. Sengupta, "Broadband mobile via satellite Inmarsat BGAN," in *Proceedings of the IEE Seminar on Broadband Satellite: The Critical Success Factors Technology, Services and Markets*, pp. 23–23, London, UK, 2002.
- [30] J. D. Oetting and T. Jen, "The mobile user objective system," *Johns Hopkins APL Technical Digest*, vol. 30, no. 2, pp. 103–112, 2011.